MEASUREMENTS OF THE TRANSVERSE SPIN-DEPENDENT TOTAL CROSS SECTION DIFFERENCE $\Delta\sigma_T$ FOR THE SCATTERING OF POLARIZED NEUTRONS FROM POLARIZED PROTONS

by

Wesley Scott Wilburn

Department of Physics
Duke University

Date:_____

Approved:

_____
N. Russell Roberson, Supervisor

_____
Lawrence E. Evans

_____
Daniel J. Gauthier

_____
Christopher R. Gould

_____
Werner Tornow

Dissertation submitted in partial fulfillment of
the requirements for the degree of Doctor
of Philosophy in the Department of
Physics in the Graduate School
of Duke University

1993

ABSTRACT

(Physics-Nuclear)

MEASUREMENTS OF THE TRANSVERSE SPIN-DEPENDENT
TOTAL CROSS SECTION DIFFERENCE $\Delta\sigma_T$ FOR THE
SCATTERING OF POLARIZED NEUTRONS
FROM POLARIZED PROTONS

by

Wesley Scott Wilburn

Department of Physics
Duke University

Date:_____

Approved:

_____
N. Russell Roberson, Supervisor

_____
Lawrence E. Evans

_____
Daniel J. Gauthier

_____
Christopher R. Gould

_____
Werner Tornow

An abstract of a dissertation submitted in partial
fulfillment of the requirements for the degree
of Doctor of Philosophy in the Department
of Physics in the Graduate School
of Duke University

1993

MEASUREMENTS OF THE TRANSVERSE SPIN-DEPENDENT TOTAL CROSS SECTION DIFFERENCE $\Delta\sigma_T$ FOR THE SCATTERING OF POLARIZED NEUTRONS FROM POLARIZED PROTONS

by

Wesley Scott Wilburn

Although the existence of a tensor component in the nucleon-nucleon interaction has been known since the discovery of the electric quadrupole moment of the deuteron, its strength has remained poorly determined, especially at low energies. The tensor force is also important as it is responsible for much of the binding energy of the triton, and it contributes significantly to the binding of other few-nucleon systems. At low energies, the strength of the tensor interaction in neutron-proton scattering is characterized by the ϵ_1 phase-shift parameter which gives the mixing between the $^3S_1$ and $^3D_1$ states. Most observables which are sensitive to ϵ_1, such as the spin-correlation coefficients $A_{yy}(\theta)$ and $A_{zz}(\theta)$, are also sensitive to other phase-shift parameters, particularly the phase shifts associated with the $^1P_1$ and $^3P_1$ states. The longitudinal and transverse spin-dependent differences in total cross section, $\Delta\sigma_L$ and $\Delta\sigma_T$, however, are very sensitive to ϵ_1 and insensitive to most other phase-shift parameters. In addition, $\Delta\sigma_L$ and $\Delta\sigma_T$ are predicted to cross through zero, allowing very accurate measurements to be made at these energies as they are unaffected by most systematic errors.

Measurements of $\Delta\sigma_T$ have been made at six energies in the region of the zero-crossing using a polarized proton target and a polarized neutron beam. The polarized proton target is of the brute-force type and consists of TiH_2 cooled to below 17 mK by a ^{3}He-^{4}He dilution refrigerator in a 7 T magnetic field. The polarized neutron beam is produced via the ^{3}H($\vec{p}$,$\vec{n}$)^{3}He reaction using a polarized proton beam obtained from the Triangle Universities Nuclear Laboratory atomic beam polarized ion source and accelerated by a tandem Van de Graaff accelerator. The beam polarization is monitored by a carbon-foil polarimeter. The temperature of the dilution refrigerator is measured by ^{3}He melting curve thermometers. In addition, polarization transfer

coefficients, $K_y^{y'}$, have been measured for the ^{3}H($\vec{\mathrm{p}}$,$\vec{\mathrm{n}}$)^{3}He reaction at three energies using a ^{4}He neutron polarimeter.

A zero-crossing energy of $E_{zc} = 5.08 \pm 0.10$ MeV has been observed for $\Delta\sigma_T$. A simple phase-shift analysis using this value results in $\epsilon_1 = 0.30 \pm 0.17°$. This result is somewhat lower than predicted by the full Bonn potential, which has the smallest tensor force of all realistic nucleon-nucleon potential models.

ACKNOWLEDGMENTS

The success of this project is due to the hard work of many people. I would like to first thank my thesis advisor, Dr. Russell Roberson for teaching me the art of experiment and for his advice, encouragement, and patience. I am grateful to Dr. Chris Gould who has been a teacher and advisor, beginning when I was an undergraduate and continuing to this day. I have greatly enjoyed working with Dr. David Haase who has taught me cryogenic techniques and more. To Dr. Werner Tornow, who first suggested this measurement, I am greatly indebted for his tireless efforts and considerable expertise.

I would like to thank Chris Keith and Paul Huffman for helping to set up and run the experiments and for doing whatever was necessary to get the job done. Tim Murphy and Brian Raichle deserve thanks for the many midnight shifts they worked. Dr. Jim Koster's help in the early days of the experiment was invaluable.

An experiment of this complexity would not be possible without a superb technical staff such as the one at TUNL. The machinists in the instrument shop, Al Lovette, Gene Harris, and Bob Hogan, could make anything I could draw, and almost always had a better way of doing it. Sidney Edwards and Pat Mulkey in the electronics shop deserve thanks for either building, fixing, or modifying much of the electronics in this experiment, often on short notice. Paul Carter, John Dunham, and Ken Sweeton have my gratitude for fixing what was broken and for keeping the lab running, despite vacuum failures, chiller woes, and water main breaks.

I have benefited from many discussions on the theoretical aspects of this work with Dr. Alec Schramm. I appreciate the timely help of Dr. H. O. Klages at KFA in Karslruhe, Germany who provided the titanium hydride for the target. Without this material, the experiment would have been delayed for several months. Chris Westerfeldt has been a source of help and advice both before and during this project. Thanks are due also to Dr. Tom Clegg and Dr. Eric Crosson for their work with the TUNL Polarized Ion Source.

I would like to thank my parents, Ed and Mary Wilburn, for encouraging my interest in science and for making my education possible. Finally, I would like to thank my son Grey for his smiles and laughs. I only hope he will be as happy in his pursuits as I have been in mine. This dissertation is dedicated to my wife Dianne whose constant love and encouragement has meant so much to me during this journey.

Contents

List of Figures

List of Tables

Chapter 1

Introduction

Although the existence of a tensor component in the nucleon-nucleon interaction has been known since the discovery of the electric quadrupole moment of the deuteron, its strength is still poorly determined, especially at low energies. The tensor force is also important as it is responsible for much of the binding energy of the triton, and it contributes significantly to the binding of other few-nucleon systems. At low energies, the strength of the tensor interaction in neutron-proton scattering is characterized by the ϵ_1 phase-shift parameter which gives the mixing between the $^3S_1$ and $^3D_1$ states. The notation used to describe the scattering states is $^{2S+1}L_J$, where S is the total spin, L refers to the orbital angular momentum, ℓ, ($S \Leftrightarrow \ell = 0$, $P \Leftrightarrow \ell = 1$, $D \Leftrightarrow \ell = 2$, etc.), and $\boldsymbol{J} = \boldsymbol{S} + \boldsymbol{\ell}$ is the total angular momentum. Most observables which are sensitive to ϵ_1, such as the spin-correlation coefficients $A_{yy}(\theta)$ and $A_{zz}(\theta)$, are also sensitive to other phase-shift parameters, particularly the phase shifts associated with the $^1P_1$ and $^3P_1$ states. The longitudinal and transverse spin-dependent differences in total cross section, $\Delta\sigma_L$ and $\Delta\sigma_T$, however, are very sensitive to ϵ_1 and insensitive to most other phase-shift parameters. In addition, $\Delta\sigma_L$ and $\Delta\sigma_T$ are predicted to cross through zero, allowing very accurate measurements to be made at energies where they are unaffected by most systematic errors.

Measurements of $\Delta\sigma_T$ have been made at six energies in the region of the zero-crossing using a polarized proton target and a polarized neutron beam. The polarized proton target is of the brute-force type and consists of TiH_2 cooled to below 17 mK in a 7 T magnetic field. The target is cooled by a ^{3}He-^{4}He dilution refrigerator and the magnetic field is produced by a superconducting split-coil solenoid. The polar-

ized neutron beam is produced via the ^{3}H($\vec{\mathrm{p}}$,$\vec{\mathrm{n}}$)^{3}He reaction using a polarized proton beam. The proton beam polarization is monitored by a carbon-foil polarimeter. The temperature of the dilution refrigerator is measured by ^{3}He melting curve thermometers. Transmitted neutrons are detected at 0° using two organic liquid scintillator cells mounted to photomultiplier tubes.

Because of their importance in the analysis of the $\Delta\sigma_T$ data, polarization-transfer coefficients, $K_y^{y'}$, have been measured for the ^{3}H($\vec{\mathrm{p}}$,$\vec{\mathrm{n}}$)^{3}He reaction at three energies using a neutron polarimeter. A high-pressure ^{4}He gas cell is used as an analyzer and the scattered neutrons are detected in four side detectors. The gas cell is an active target, scintillating from the recoiling alpha particles. Coincidences between the scattered neutrons and the recoiling alphas greatly reduce the background counts.

A zero-crossing energy, E_{zc}, has been extracted from the $\Delta\sigma_T$ data and used in a simple phase-shift analysis to determine the value of ϵ_1 at that energy. The data and the resulting values of E_{zc} and ϵ_1 are compared to potential-model predictions.

Chapter 2

Theoretical Overview

2.1 Nuclear Tensor Interaction

At present, the only satisfactory theories of the nuclear force are meson-exchange models. These models treat nucleons as fundamental particles which interact through the exchange of mesons with Yukawa-type potentials. Although nucleons are known to actually be composite, no realistic quark model of the nuclear interaction has as yet been constructed due to the computational difficulties of such an approach. At the other extreme, phenomenological models exist, but they are unable to provide insight into the underlying mechanisms. Thus it is reasonable to look for the origins of a nuclear tensor interaction in meson exchange.

The Yukawa potential arises from considering the wave equation for massive particles [Yuk35].

$$\left(\nabla^2 - \frac{m^2c^2}{\hbar^2}\right)\phi = \frac{1}{c^2}\frac{\partial^2\phi}{\partial t^2} \tag{2.1}$$

Here, m is the mass of the exchanged particle. The solutions to this equation fall off exponentially with distance, with a decay constant proportional to the mass. The strength of the interaction is given by a coupling constant g.

$$\phi = \frac{g}{4\pi}\frac{e^{-mcr/\hbar}}{r} \tag{2.2}$$

Since pions have the smallest mass of the mesons involved in the nuclear force, they will have the largest contribution at long range. Because pions have negative intrinsic

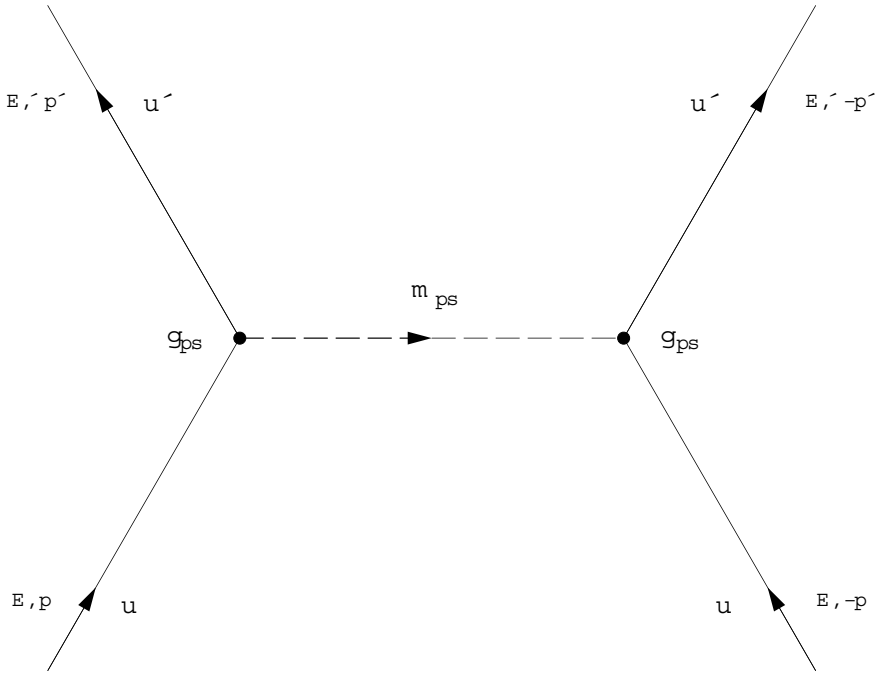

Figure 2.1: Feynman Diagram for One-Pion Exchange

parity, a pseudoscalar coupling is chosen to conserve parity. The Lagrangian for one-pion exchange (represented by the Feynman diagram in Figure 2.1) is then of the form

$$\mathcal{L}_{ps} = g_{ps}\bar{\Psi} i\gamma_5 \Psi \phi_{ps}. \tag{2.3}$$

The matrix element for this interaction can be written

$$\mathcal{M}_{fi} = \frac{g_{ps}^2(\bar{u}_1' i\gamma_5 u_1)(\bar{u}_2' i\gamma_5 u_2)}{(\boldsymbol{p}-\boldsymbol{p}')^2 + m_{ps}^2}. \tag{2.4}$$

$\boldsymbol{p}$ and $\boldsymbol{p}'$ are the initial and final momenta, and u and u' are the initial and final wave functions. In the non-relativistic limit, the wave functions have the form

$$u_1 = \sqrt{\frac{E+M}{2M}} \begin{pmatrix} 1 \\ \frac{\boldsymbol{\sigma}_1 \boldsymbol{p}}{E+M} \end{pmatrix} \chi_1, \tag{2.5}$$

where M is the nucleon mass, $\boldsymbol{\sigma}$ and $\boldsymbol{p}$ are the spin and momentum operators, and χ is the spin wavefunction. Evaluating the matrix element gives the result

$$\mathcal{M}_{fi} = \frac{-g_{ps}^2}{4M^2} \frac{(\boldsymbol{\sigma}_1 \cdot \boldsymbol{q})(\boldsymbol{\sigma}_2 \cdot \boldsymbol{q})}{q^2 + m_{ps}^2}, \tag{2.6}$$

with $\boldsymbol{q} = \boldsymbol{p}' - \boldsymbol{p}$. This interaction can be expressed as a momentum-space potential

$$V_{ps}(\boldsymbol{k}) = \frac{-g_{ps}^2}{4M^2} \frac{(\boldsymbol{\sigma}_1 \cdot \boldsymbol{k})(\boldsymbol{\sigma}_2 \cdot \boldsymbol{k})}{k^2 + m_{ps}^2}. \tag{2.7}$$

By performing a three-dimensional Fourier transform, the coordinate-space potential may be obtained [Mac86].

$$V_{ps}(\boldsymbol{x}) = \frac{g_{ps}^2}{4\pi} \frac{m_{ps}^2}{12M^2} \left\{ \boldsymbol{\sigma}_1 \cdot \boldsymbol{\sigma}_2 + S_{12}(\hat{\boldsymbol{x}}) \left[1 + \frac{3}{m_{ps} r} + \frac{3}{(m_{ps} r)^2} \right] \right\} \frac{e^{-m_{ps} r}}{r} \tag{2.8}$$

S_{12} is the tensor operator

$$S_{12}(\hat{\boldsymbol{x}}) = 3(\boldsymbol{\sigma}_1 \cdot \hat{\boldsymbol{x}})(\boldsymbol{\sigma}_2 \cdot \hat{\boldsymbol{x}}) - \boldsymbol{\sigma}_1 \cdot \boldsymbol{\sigma}_2. \tag{2.9}$$

The first term of the potential is a spin-dependent central interaction while the second is a tensor interaction which mixes states with different orbital angular momentum. This type of interaction also arises from considering the tensor coupling of vector mesons such as the rho.

$$\mathcal{L}_t = \frac{g_v}{2M} \bar{\Psi} \sigma_{\mu\nu} \Psi \partial^\mu \phi_{ps}^\nu \tag{2.10}$$

This coupling results in a coordinate-space potential

$$V_t(\boldsymbol{x}) = \frac{g_v^2}{4\pi} \frac{m_v^2}{12M^2} \left\{ 2\boldsymbol{\sigma}_1 \cdot \boldsymbol{\sigma}_2 - S_{12}(\hat{\boldsymbol{x}}) \left[1 + \frac{3}{m_v r} + \frac{3}{(m_v r)^2} \right] \right\} \frac{e^{-m_v r}}{r} \tag{2.11}$$

containing a tensor term of the same form but opposite in sign compared to the pseudoscalar coupling. The tensor force is thus reduced at shorter distances where the heavier rho contributes to the nuclear interaction.

2.2 Phase-Shift Parameters

The elastic scattering of one spinless particle from another can be described asymptotically as the superposition of an incident plane wave with a scattered spherical wave [Sch68, DeB67]. If only central forces are involved, the orbital angular momentum, ℓ, is conserved and the incident plane wave can be written as a partial-wave expansion.

$$\begin{aligned} \Psi_i &= A e^{ikz} \\ &= A \sum_{\ell=0}^{\infty} i^\ell (2\ell + 1) j_\ell(kr) P_\ell(\cos\theta) \end{aligned} \tag{2.12}$$

For large values of r,

$$\begin{aligned} j_\ell &\approx \frac{\sin(kr - \frac{1}{2}\ell\pi)}{kr} \\ &\approx i\frac{e^{-i(kr-\ell\frac{\pi}{2})} - e^{+i(kr-\ell\frac{\pi}{2})}}{2kr}. \end{aligned} \tag{2.13}$$

The incident plane wave can then be described (in the asymptotic limit) as the sum of incoming and outgoing spherical waves and is given by

$$\Psi_i = \frac{A}{2kr}\sum_{\ell=0}^{\infty} i^{\ell+1}(2\ell+1)\left[e^{-i(kr-\ell\frac{\pi}{2})} - e^{+i(kr-\ell\frac{\pi}{2})}\right]P_\ell(\cos\theta). \tag{2.14}$$

Since the scattered wave consists only of outgoing spherical waves, it can be included by modifying the second term of Equation 2.14 by a factor η_ℓ. The total wave function is then

$$\Psi = \frac{A}{2kr}\sum_{\ell=0}^{\infty} i^{\ell+1}(2\ell+1)\left[e^{-i(kr-\ell\frac{\pi}{2})} - \eta_\ell e^{+i(kr-\ell\frac{\pi}{2})}\right]P_\ell(\cos\theta). \tag{2.15}$$

The scattered wave is then obtained by subtracting the incident wave from the total.

$$\begin{aligned} \Psi_s &= \Psi - \Psi_i \\ &= \frac{A}{2kr}\sum_{\ell=0}^{\infty} i^{\ell+1}(2\ell+1)(1-\eta_\ell)e^{i(kr-\ell\frac{\pi}{2})}P_\ell(\cos\theta) \\ &= A\frac{i}{2k}\frac{e^{ikr}}{r}\sum_{\ell=0}^{\infty}(2\ell+1)(1-e^{i\delta_\ell})P_\ell(\cos\theta) \end{aligned} \tag{2.16}$$

$$\tag{2.17}$$

Here $e^{i\delta_\ell} = \eta_\ell$ and δ_ℓ are the phase shifts. The total wave function can be written asymptotically in terms of the scattering amplitude, $f(\theta)$, as

$$\Psi = A\left[e^{ikz} + f(\theta)\frac{e^{ikz}}{r}\right]. \tag{2.18}$$

Comparing this result to Equation 2.15 gives

$$f(\theta) = \frac{i}{2k}\sum_{\ell=0}^{\infty}(2\ell+1)(1-e^{i\delta_\ell})P_\ell(\cos\theta). \tag{2.19}$$

The differential cross section is then

$$\begin{aligned}\sigma(\theta) &= |f(\theta)|^2 \\ &= \frac{1}{k^2}\left|\sum_{\ell=0}^{\infty}(2\ell+1)e^{i\delta_\ell}\sin\delta_\ell\, P_\ell(\cos\theta)\right|^2 . \end{aligned} \tag{2.20}$$

Integrating over θ gives the total cross section in terms of the phase shifts.

$$\sigma = \frac{4\pi}{k^2}\sum_{\ell=0}^{\infty}(2\ell+1)\sin^2\delta_\ell \tag{2.21}$$

There exists one scattering eigenstate corresponding to each value of ℓ. The contribution of each eigenstate is determined by its corresponding phase shift, δ_ℓ. The phase shifts are related to the scattering matrix, $\mathbf{S}$, through the expression

$$S_{fi} = \begin{cases} e^{2i\delta_\ell}, & \ell_f = \ell_i = \ell \\ 0, & \ell_f \neq \ell_i \end{cases} \tag{2.22}$$

when purely central forces act. The subscripts i and f refer to the initial and final states. Off-diagonal terms will occur in $\mathbf{S}$ if non-central interactions exist.

In a phase-shift description of nucleon-nucleon scattering, the spin 1/2 nature of the nucleons must be considered. The principal quantum number is now the total angular momentum, J. Whereas before there was one state for each value of ℓ, there are now four states for each value of the total angular momentum J, for $J \geq 1$. There is a spin-singlet state with orbital angular momentum $\ell = J$ and three spin-triplet states with $\ell = J-1$, $\ell = J$, and $\ell = J+1$. Total spin S is conserved under the assumption of charge independence, while ℓ is conserved for pure central forces. Since the tensor force is manifestly non-central, mixing can occur for states with the same J, S, and parity, but with different ℓ; the triplet states with $\ell = J-1$ and $\ell = J+1$. For the simplest case in which mixing can occur, $J = 1$,[1] the four scattering states are:

$$^1P_1$$
$$^3S_1$$
$$^3P_1$$
$$^3D_1$$

[1] There is no mixing for $J = 0$ because there are no states with $\ell = J \pm 1$.

and mixing of states can occur between ${}^3S_1$ and ${}^3D_1$. In the case of proton-proton and neutron-neutron scattering, only states with total isospin $T = 1$ exist, whereas in the case of neutron-proton scattering states with both $T = 0$ and $T = 1$ occur [DeB67]. In addition, the Pauli principle requires

$$(-1)^{S+T+\ell} = -1. \tag{2.23}$$

Thus, for identical particles, only singlet states with even ℓ and triplet states with odd ℓ are allowed. Mixing can then occur only for states with even J in the pp and nn cases.

When a tensor interaction exists, the states with $\ell = J - 1$ and $\ell = J + 1$ are no longer energy eigenfunctions. Instead, the new states are α_J and β_J which are a mixture of the two states of definite ℓ. The part of the scattering matrix corresponding to these states has the form [Bla52a, Bla52b]

$$\mathbf{S} = \mathbf{U}^{-1} e^{2i\mathbf{\Delta}} \mathbf{U} \tag{2.24}$$

where

$$\mathbf{U} = \begin{pmatrix} \cos\epsilon_J & \sin\epsilon_J \\ -\sin\epsilon_J & \cos\epsilon_J \end{pmatrix}, \tag{2.25}$$

$$\mathbf{\Delta} = \begin{pmatrix} \delta_{J\alpha} & 0 \\ 0 & \delta_{J\beta} \end{pmatrix}. \tag{2.26}$$

$\delta_{J\alpha}$ and $\delta_{J\beta}$ are the phase shifts and ϵ_J is the mixing parameter, in the notation of Blatt and Biedenharn. By convention, these states are referred to as ${}^3S_1$ and ${}^3D_1$, even though they are not states of pure ℓ, except at $E = 0$. At low energies, ϵ_1 is the phase-shift parameter which most directly characterizes the strength of the tensor interaction. Because of the difference in ℓ of the two states coupled by the tensor interaction, no mixing can occur at $E_n = 0$. At the lowest energies (below approximately 2 MeV), ϵ_1 is constrained by this kinematic consideration and by the properties of the deuteron.

2.3 Spin-Dependent Total Cross Section Differences

Phase-shift parameters are not directly measurable. Instead, experiments designed to measure the strength of the tensor force at low energies must measure observables sensitive to the ϵ_1 mixing parameter. Ideally, these observables will not be sensitive to any other phase-shift parameters. In order to be sensitive to a spin-spin interaction such as the tensor force, two polarizations must be measured by the observable. Such observables include the spin-correlation parameters $A_{yy}(\theta)$ and $A_{zz}(\theta)$. Unfortunately, these measurements are also very dependent upon the $^1P_1$ phase shift except at $\theta = 90°$ which is experimentally very difficult.

Another set of observables are the spin-dependent differences in total cross section, $\Delta\sigma$, [Bug80, Tor88] where

$$\Delta\sigma = \sigma(0°, \boldsymbol{I}, -\boldsymbol{s}) - \sigma(0°, \boldsymbol{I}, \boldsymbol{s}). \tag{2.27}$$

$\boldsymbol{I}$ is the spin of the proton target, and $\boldsymbol{s}$ is the spin of the neutron projectile. In the simplest case, $\boldsymbol{I}$ and $\boldsymbol{s}$ are along the same axis and can either be longitudinal or transverse with respect to the direction of propagation. More general cases are discussed in Appendix B. The longitudinal and transverse cases are defined by

$$\Delta\sigma_L = \sigma(\overrightarrow{\leftarrow}) - \sigma(\overrightarrow{\rightarrow}), \tag{2.28}$$

$$\Delta\sigma_T = \sigma(\uparrow\downarrow) - \sigma(\uparrow\uparrow). \tag{2.29}$$

Where the top or first arrow refers to the target spin and the bottom or second refers to the projectile spin. The total cross section can be decomposed into two parts

$$\sigma = \sigma_0 + \sigma_{ss} \tag{2.30}$$

where σ_0 is even under a reversal of projectile spin and σ_{ss} is odd. The total cross section differences depend only on the second term.

$$\begin{aligned} \Delta\sigma &= (\sigma_0 + \sigma_{ss}) - (\sigma_0 - \sigma_{ss}) \\ &= 2\sigma_{ss} \end{aligned} \tag{2.31}$$

The spin-spin cross section can then be divided into scalar and tensor parts

$$\sigma_{ss} = \sigma_s(\boldsymbol{\sigma}_1 \cdot \boldsymbol{\sigma}_2) + \sigma_t S_{12}, \tag{2.32}$$

where the tensor operator, S_{12}, is defined in Equation 2.9. This gives

$$\Delta\sigma_L = 2(\sigma_s + 2\sigma_t), \tag{2.33}$$

$$\Delta\sigma_T = 2(\sigma_s - \sigma_t). \tag{2.34}$$

$\Delta\sigma_L$ and $\Delta\sigma_T$ are then two different linear combinations of the scalar and tensor parts of the spin-spin cross section. These observables can be written in terms of the phase-shift parameters in the Stapp convention as [Tor91]

$$\Delta\sigma_L = \frac{\pi}{k^2}\left[\begin{array}{l} -2 + \cos 2\delta_{1S0} + \cos 2\delta_{3P0} + 3\cos 2\delta_{1P1} \\ \quad - \cos 2\delta_{3S1} - 3\cos\delta_{3P1} + \cos 2\delta_{3D1} \\ \quad - 4\sqrt{2}\sin(\delta_{3S1} + \delta_{3D1})\sin 2\epsilon_1 + 5\cos 2\delta_{1D2} \\ \quad - \cos 2\delta_{3P2} - 5\cos 2\delta_{3D2} + \cos 2\delta_{3F2} \\ \quad - 4\sqrt{6}\sin(\delta_{3P2} + \delta_{3F2})\sin 2\epsilon_2 + \cdots \end{array}\right], \tag{2.35}$$

$$\Delta\sigma_T = \frac{\pi}{k^2}\left[\begin{array}{l} \cos 2\delta_{1S0} - \cos 2\delta_{3P0} + 3\cos 2\delta_{1P1} \\ \quad - \cos 2\delta_{3S1} - 2\cos 2\delta_{3D1} \\ \quad + 2\sqrt{2}\sin(\delta_{3S1} + \delta_{3D1})\sin 2\epsilon_1 \\ \quad + 5\cos 2\delta_{1D2} - 2\cos 2\delta_{3P2} - 3\cos 2\delta_{3F2} \\ \quad + 2\sqrt{6}\sin(\delta_{3P2} + \delta_{3F2})\sin 2\epsilon_2 + \cdots \end{array}\right]. \tag{2.36}$$

In these equations, δ_{1S0}, for example, refers to the phase shift for the $^1S_0$ state.

2.4 Potential Models

Potential models of the nucleon-nucleon interactions vary considerably in the strength of the tensor force. In terms of the phase shifts, this variation can be seen in the ϵ_1 mixing parameter. Figure 2.2 shows ϵ_1 as a function of energy for several potential models as well as the phase-shift analysis, SM92, of Ardnt [Mac87, Bra88, Mac89, Lac80, Nag78, Arn92]. This variation in tensor strength can also be observed in the predictions of the properties of the deuteron. Table 2.1 lists the deuteron D-state probability, P_D, magnetic dipole moment, μ_d, and electric quadrupole moment, Q_d, for various potential models [Mac87, Bra88, Mac89, Nag78, Lac80, Rei68, Kel39,

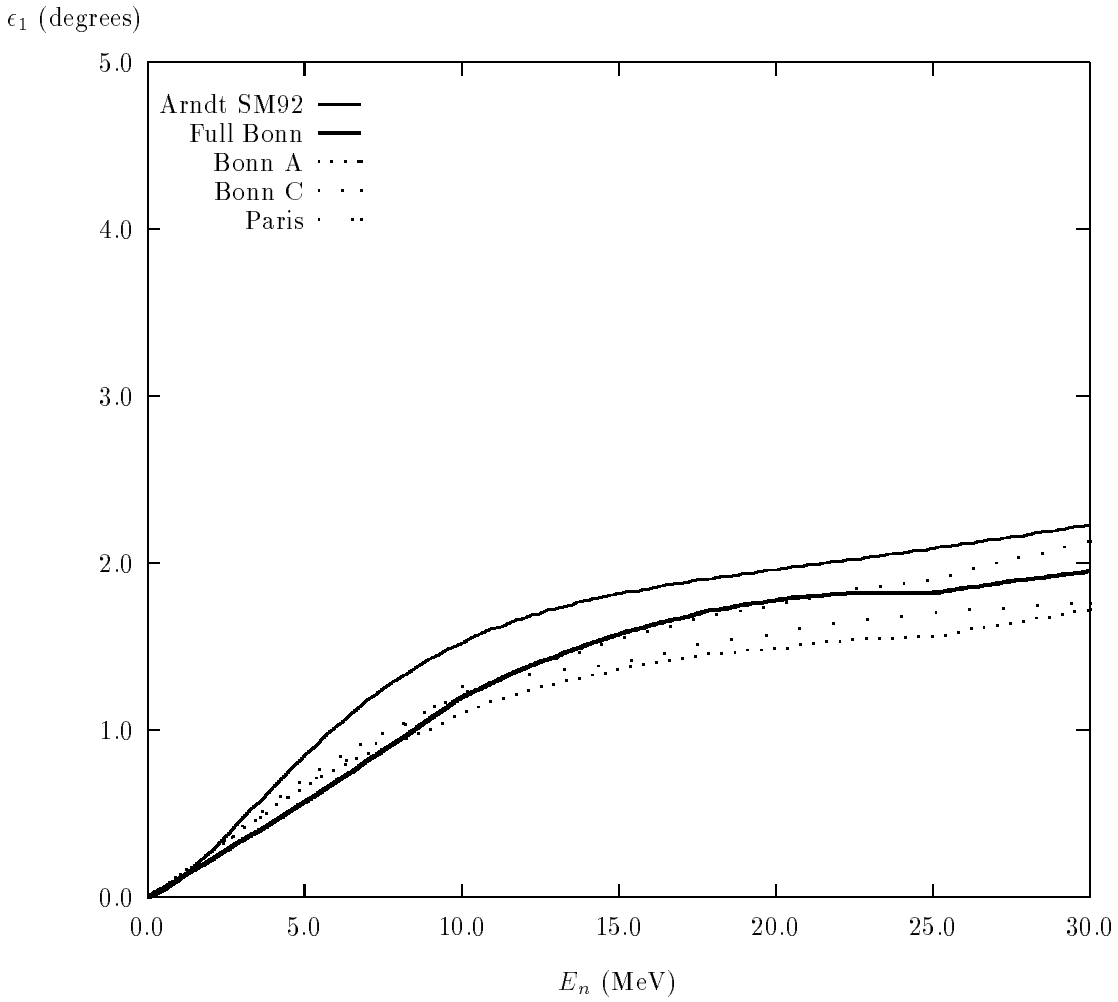

Figure 2.2: Potential-Model Predictions of the ϵ_1 Mixing Parameter

Potential	Q_d (fm^2)	μ_d (μ_N)	P_D (%)
Full Bonn	0.2807	0.8555	4.25
Bonn A	0.274	0.8548	4.4
Bonn B	0.278	0.8514	5.0
Bonn C	0.281	0.8478	5.6
Nijmegen	0.2715		5.4
Paris	0.279	0.853	5.8
Reid Soft Core	0.2796		6.5
Experiment	0.2859	0.857406	
	$\pm$ 0.0003	$\pm$ 0.000001	

Table 2.1: Predicted Deuteron Properties for Various Potential Models

Eri84]. The binding energy of the triton is also greatly affected by the choice of tensor strength. Figure 2.3 shows the strong correlation that exists between the deuteron D-state probability and the triton binding energy [Bra88]. Models with a stronger tensor force, as indicated by a larger P_D, underestimate the triton binding energy more than models with a weaker tensor force.

Predictions of $\Delta\sigma_L$ and $\Delta\sigma_T$ can be calculated from the potential-model phase shifts. Figures 2.4 and 2.5 show these results for several models and for the Arndt phase-shift analysis in the energy range of interest. In addition, sensitivity calculations can be performed by varying the phase-shift parameters of one model. For this purpose, the Arndt phase-shift analysis, SP89, is chosen [Arn89]. The phase shifts are varied by $\pm 1^\circ$ and the resulting shifts in $\Delta\sigma_L$ and $\Delta\sigma_T$ are plotted in Figures 2.6–2.19 for $J \leq 1$. Higher partial waves do not contribute significantly to these observables. These figures show that $\Delta\sigma_L$ and $\Delta\sigma_T$ are more sensitive to ϵ_1 than to the other phase-shift parameters. $\Delta\sigma_L$ and $\Delta\sigma_T$ can be expressed to a good approximation in terms of only $^1S_0$, $^3S_1$, and ϵ_1. The sensitivity to ϵ_1 is a maximum at about 10 MeV: approximately 51 mb/degree for $\Delta\sigma_L$ and 26 mb/degree for $\Delta\sigma_T$. Of particular interest from an experimental viewpoint are the zero-crossing energies of $\Delta\sigma_L$ and $\Delta\sigma_T$, which also display large sensitivities to ϵ_1. Measurements made at the zero-crossing energies are insensitive to most systematic uncertainties. Predictions for the zero-crossings of $\Delta\sigma_L$ and $\Delta\sigma_T$ are shown in Figures 2.20 and 2.21.

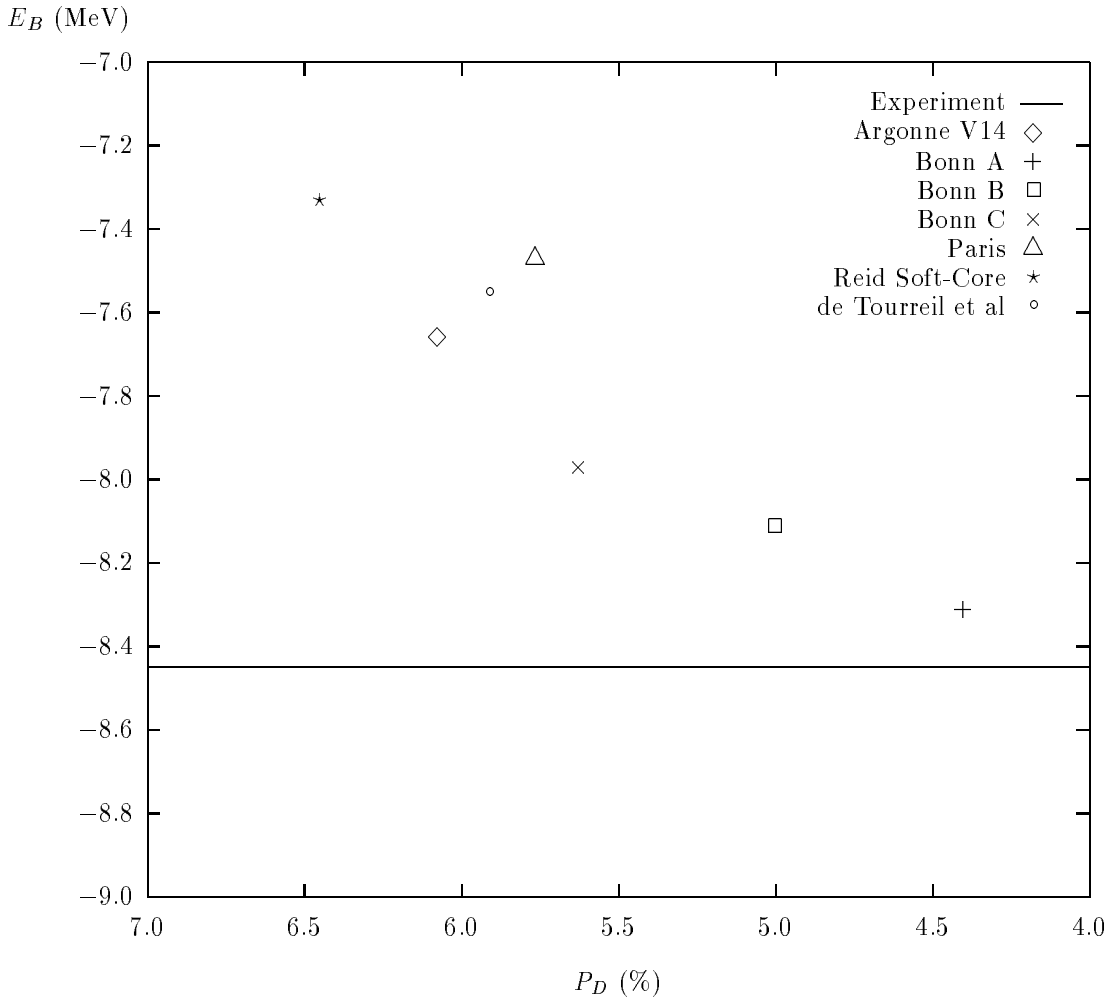

Figure 2.3: Triton Binding Energy versus Deuteron D-State Probability for Various Potential Models

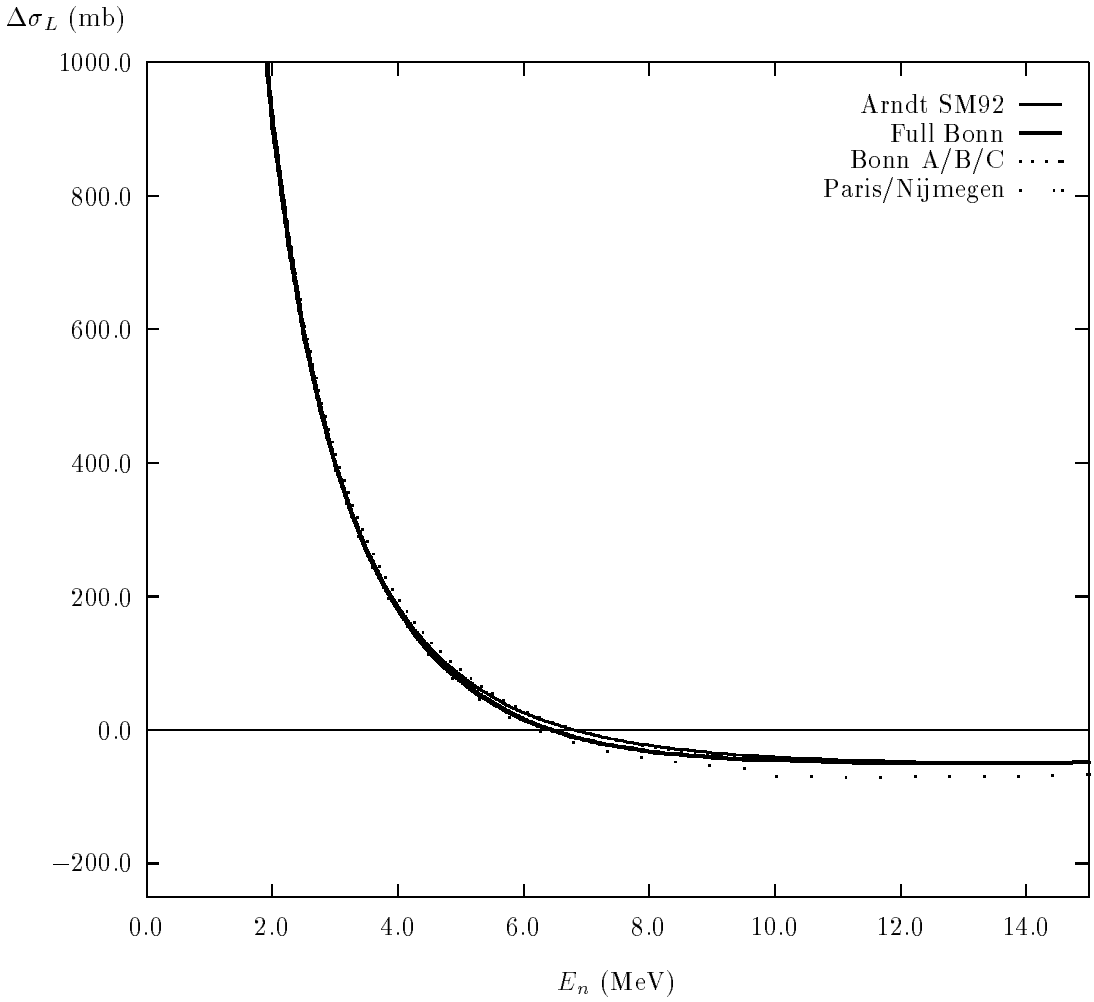

Figure 2.4: Potential-Model Predictions for $\Delta\sigma_L$ at Low Energies

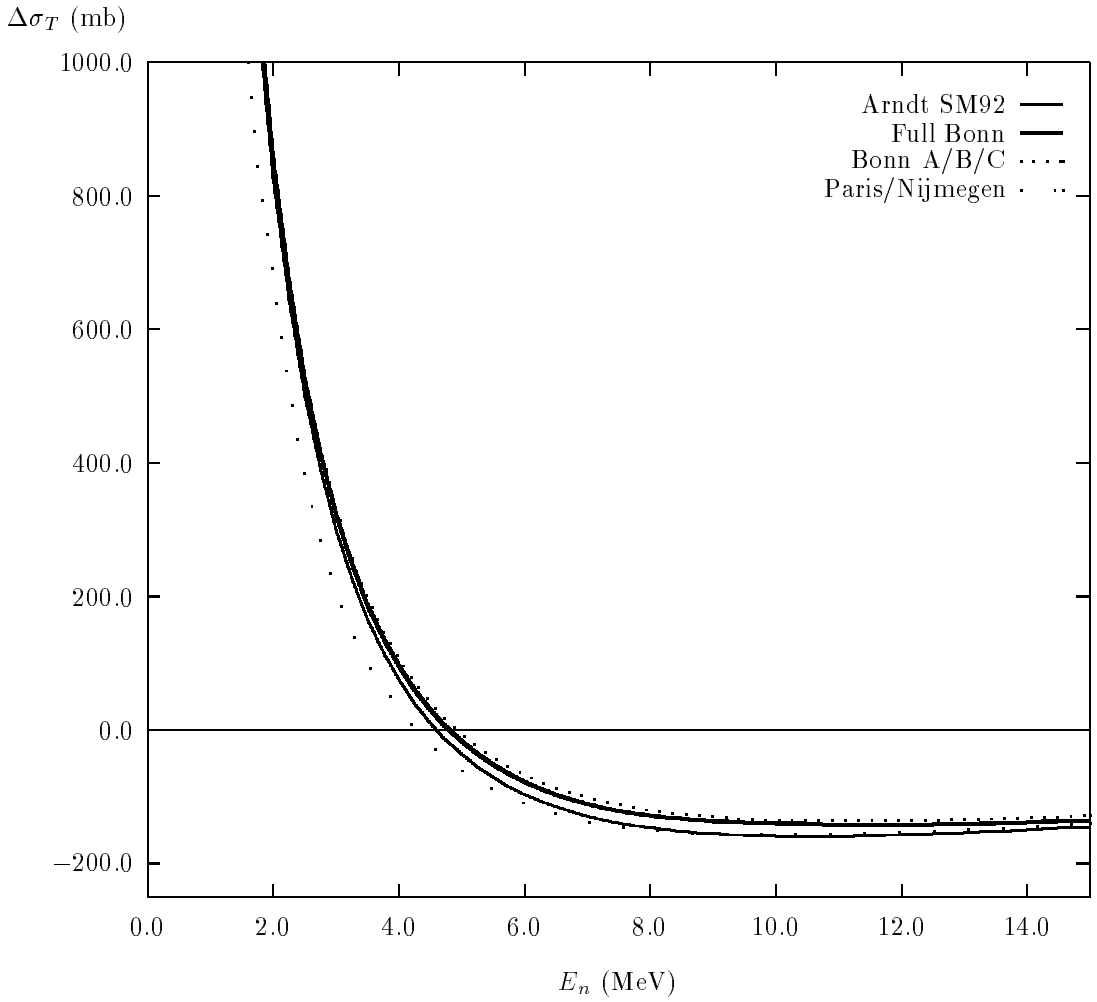

Figure 2.5: Potential-Model Predictions for $\Delta\sigma_T$ at Low Energies

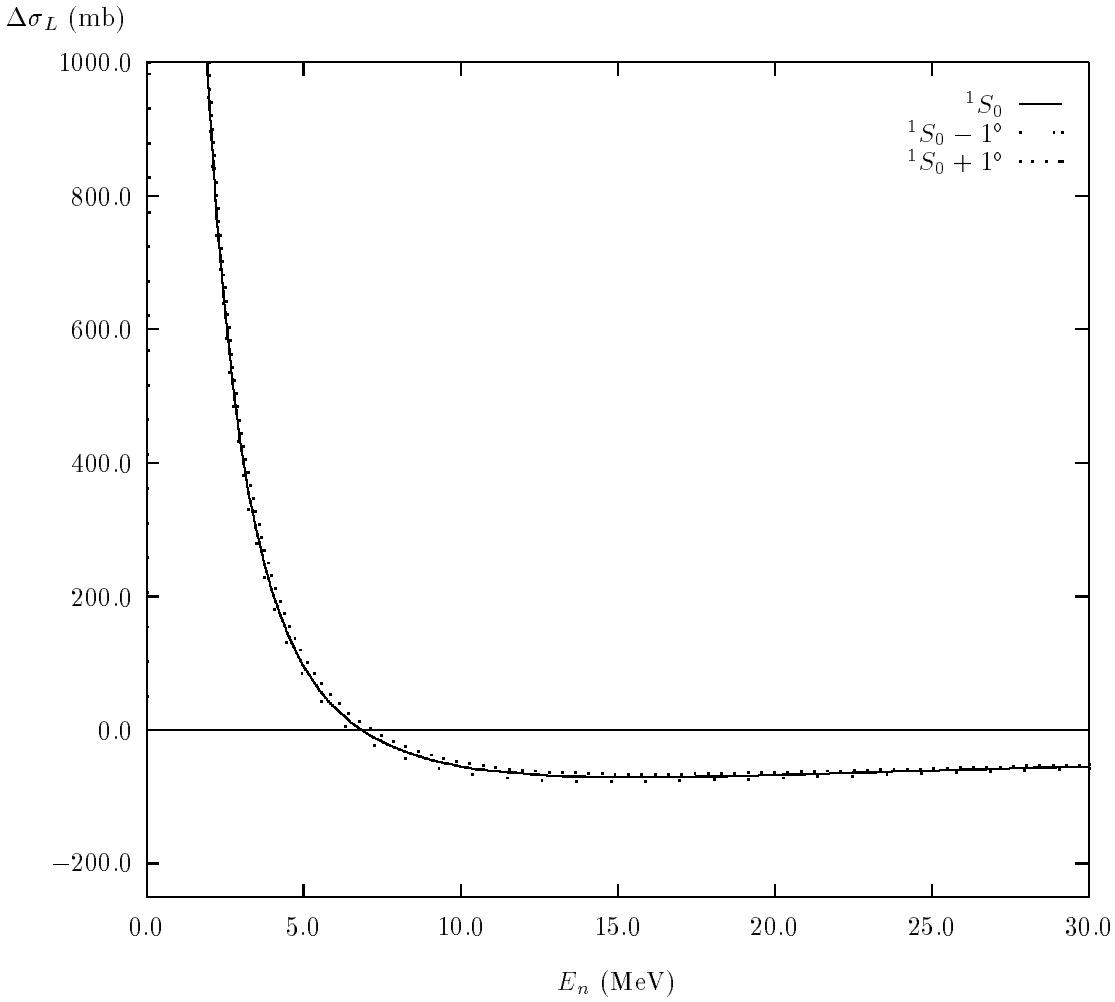

Figure 2.6: Sensitivity of $\Delta\sigma_L$ to a $\pm 1°$ Variation in $^1S_0$ Using Arndt SP89

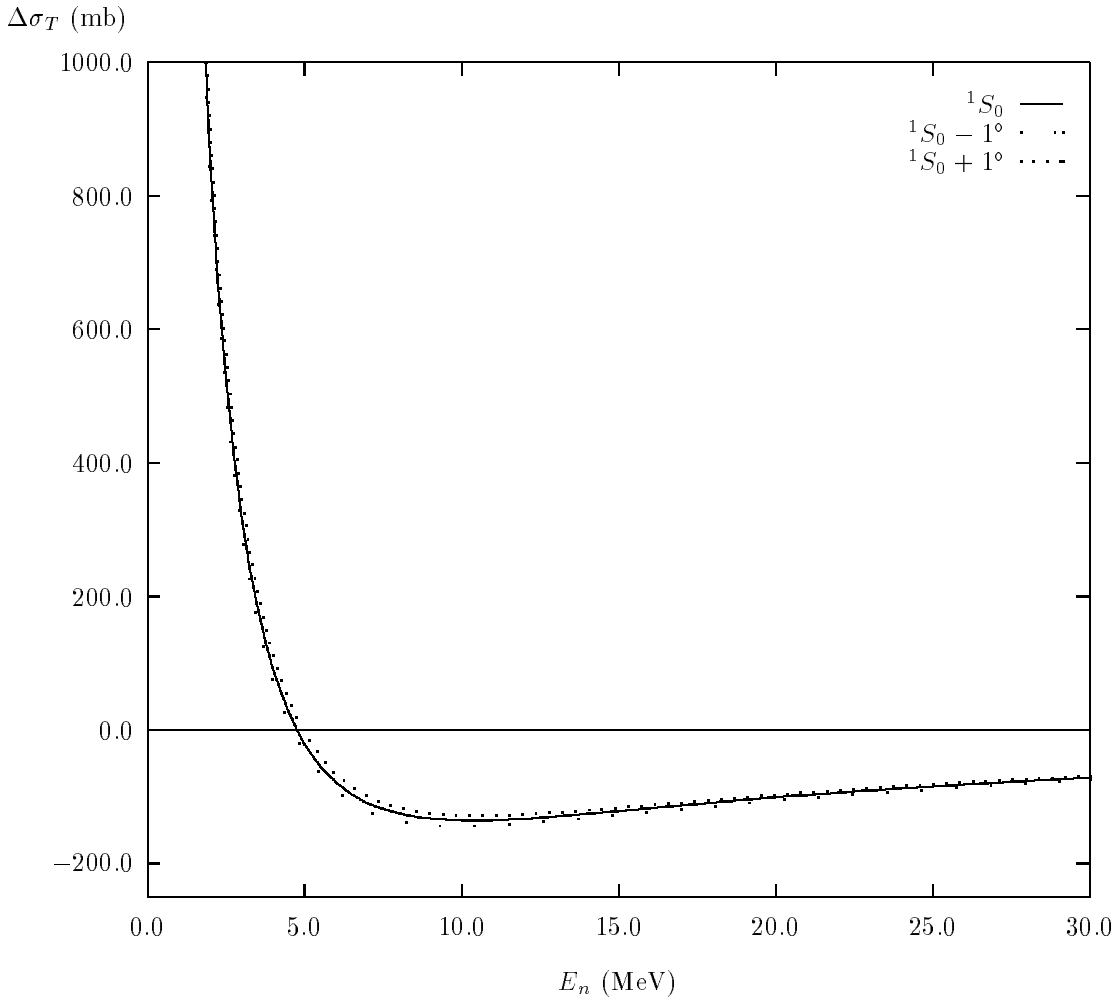

Figure 2.7: Sensitivity of $\Delta\sigma_T$ to a $\pm 1°$ Variation in $^1S_0$ Using Arndt SP89

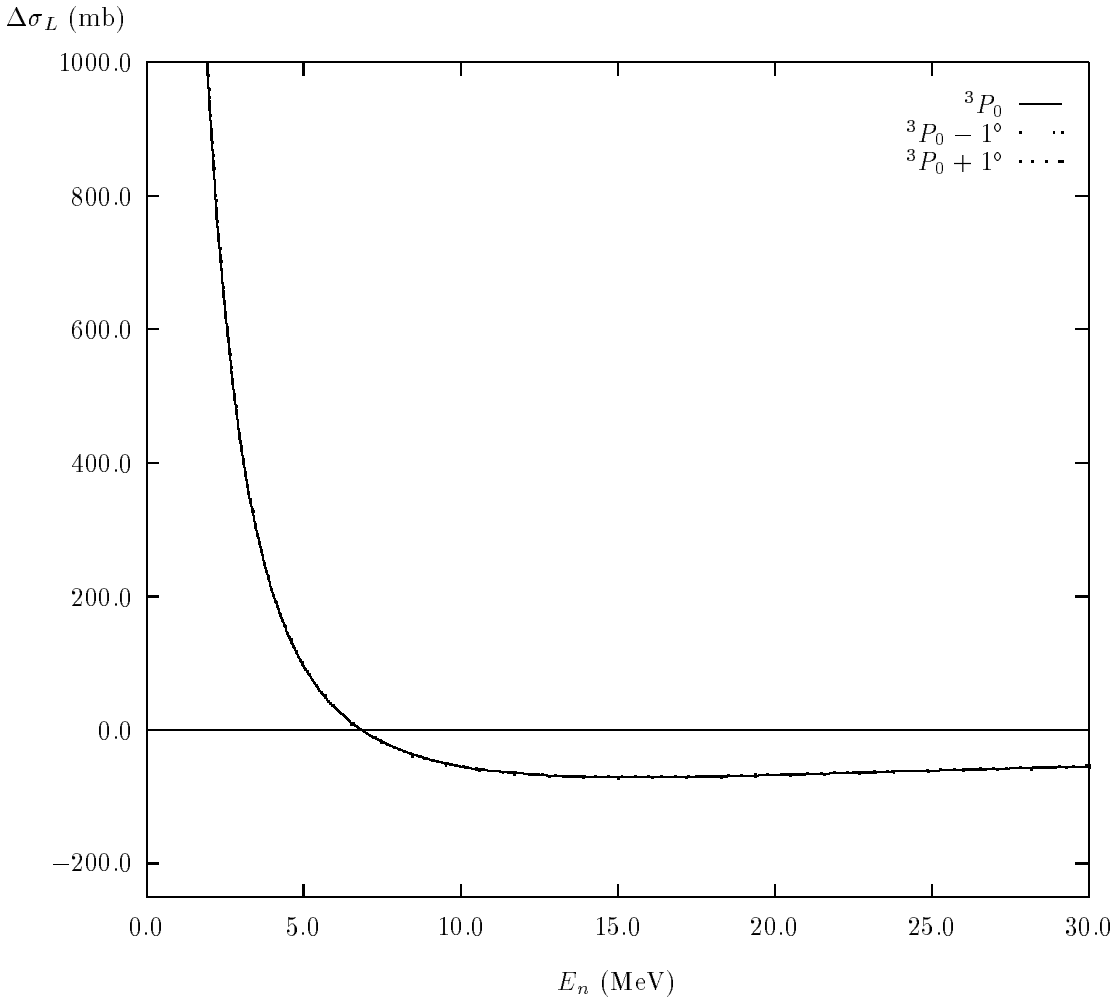

Figure 2.8: Sensitivity of $\Delta\sigma_L$ to a $\pm 1°$ Variation in $^3P_0$ Using Arndt SP89

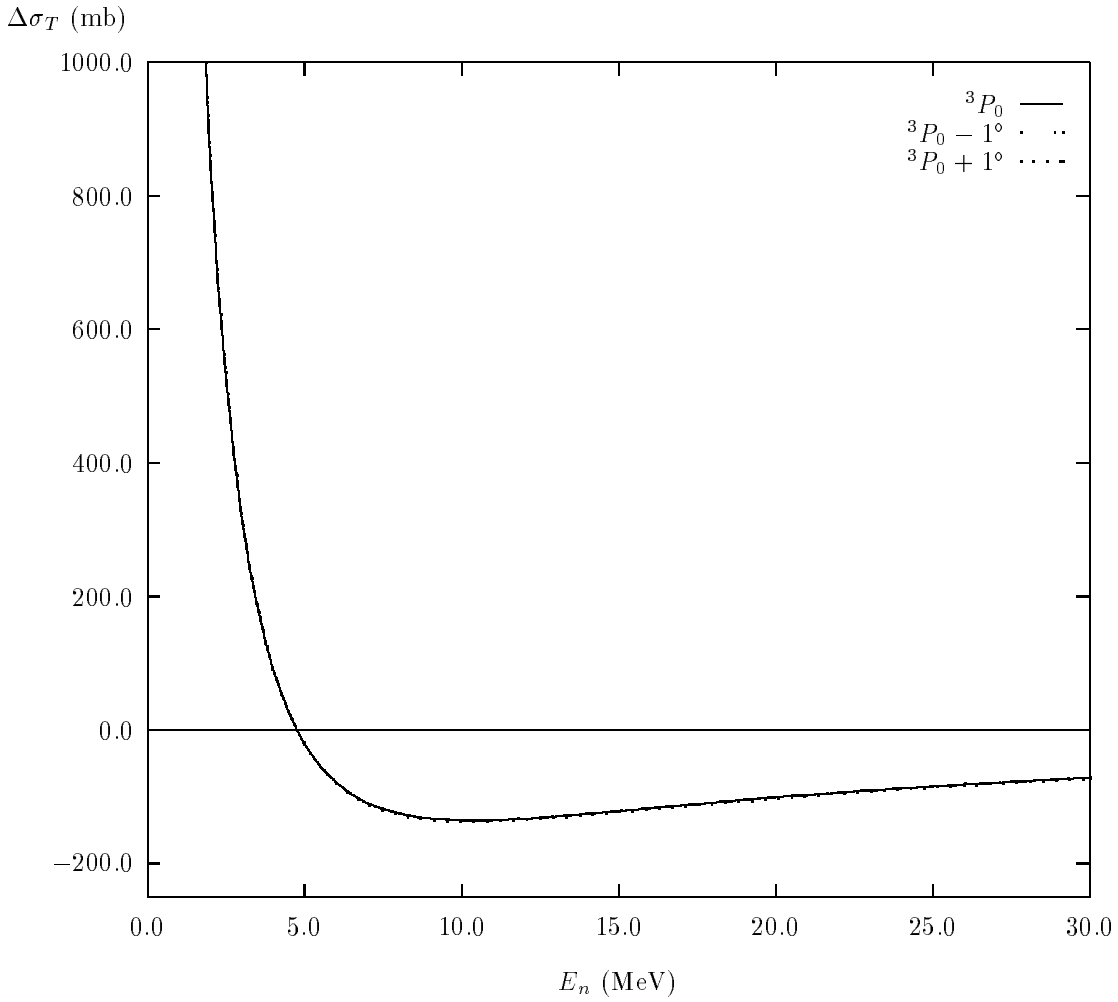

Figure 2.9: Sensitivity of $\Delta\sigma_T$ to a $\pm 1°$ Variation in $^3P_0$ Using Arndt SP89

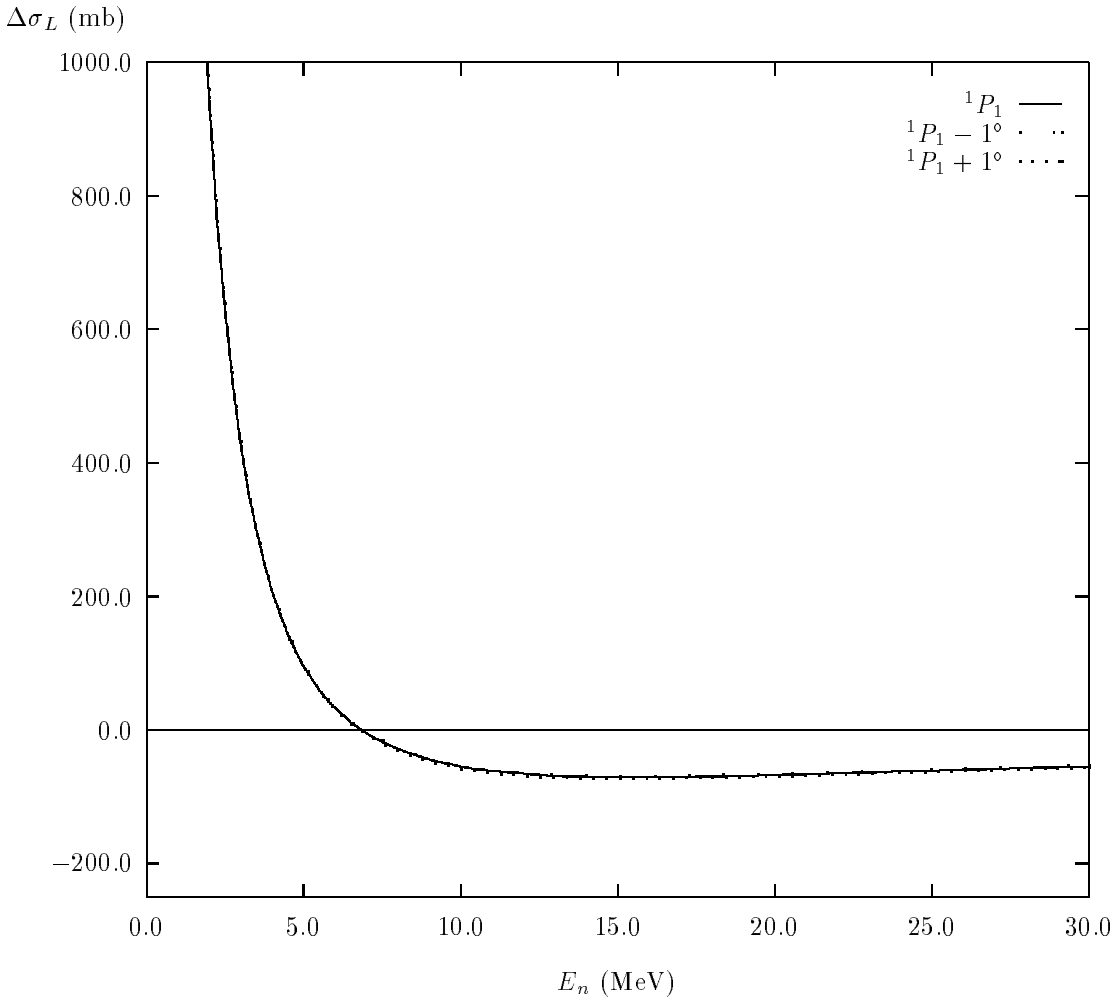

Figure 2.10: Sensitivity of $\Delta\sigma_L$ to a $\pm 1°$ Variation in $^1P_1$ Using Arndt SP89

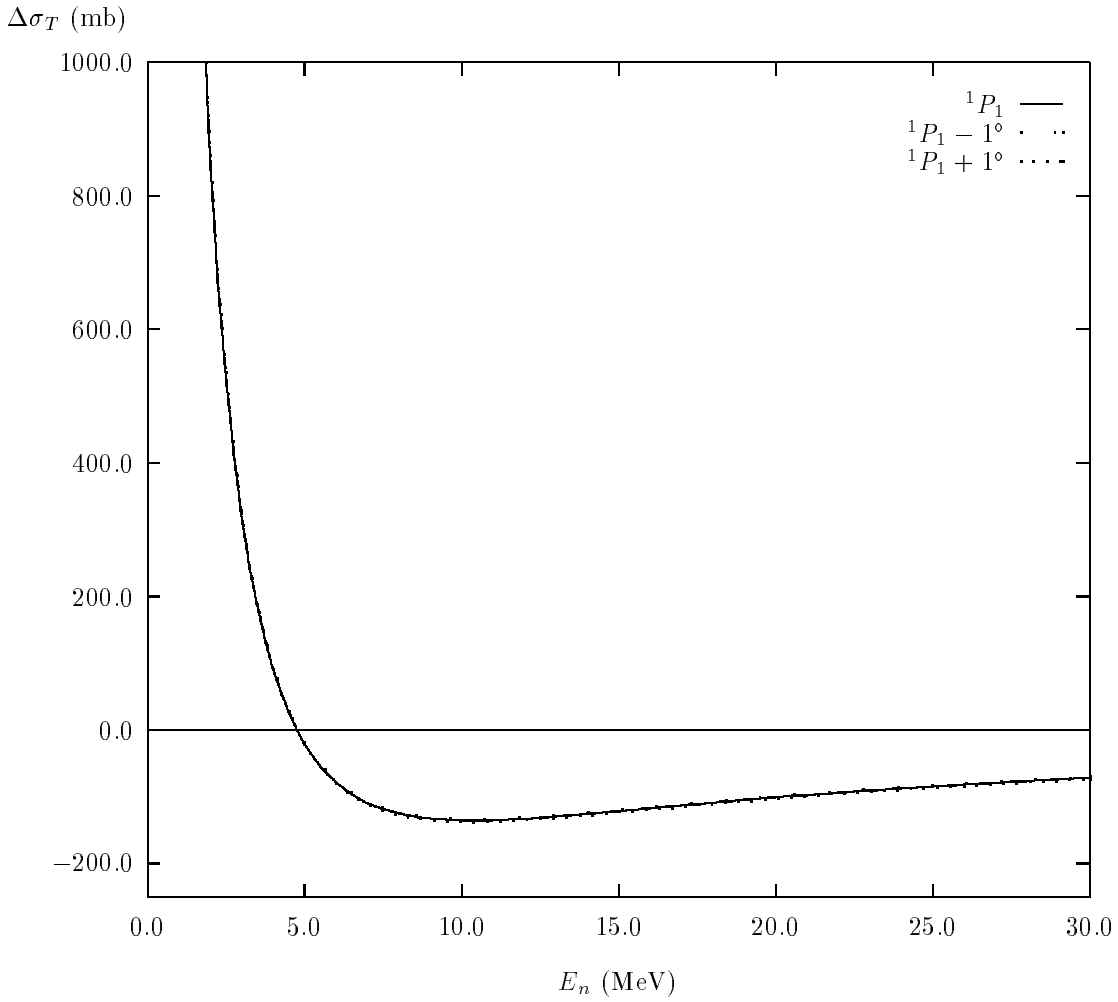

Figure 2.11: Sensitivity of $\Delta\sigma_T$ to a $\pm 1°$ Variation in $^1P_1$ Using Arndt SP89

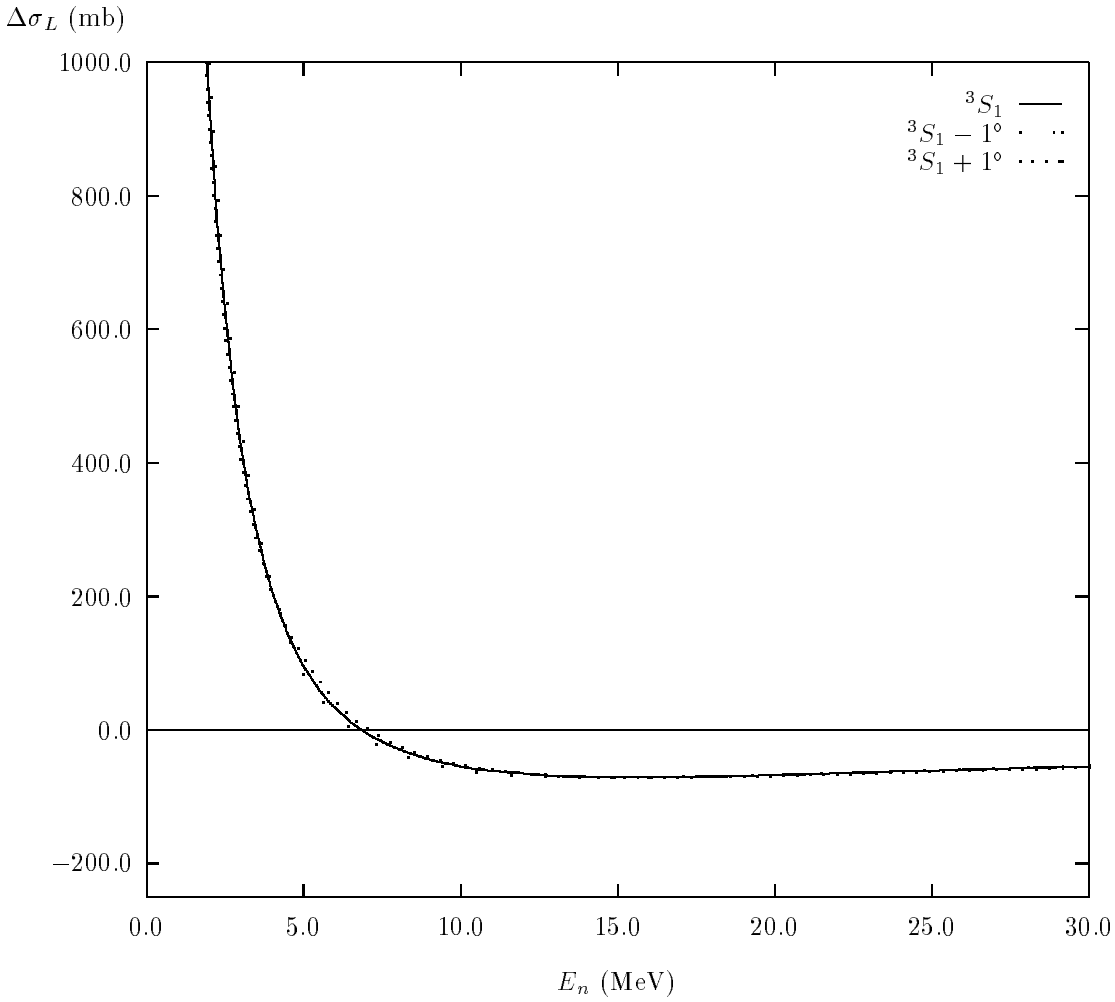

Figure 2.12: Sensitivity of $\Delta\sigma_L$ to a $\pm 1°$ Variation in $^3S_1$ Using Arndt SP89

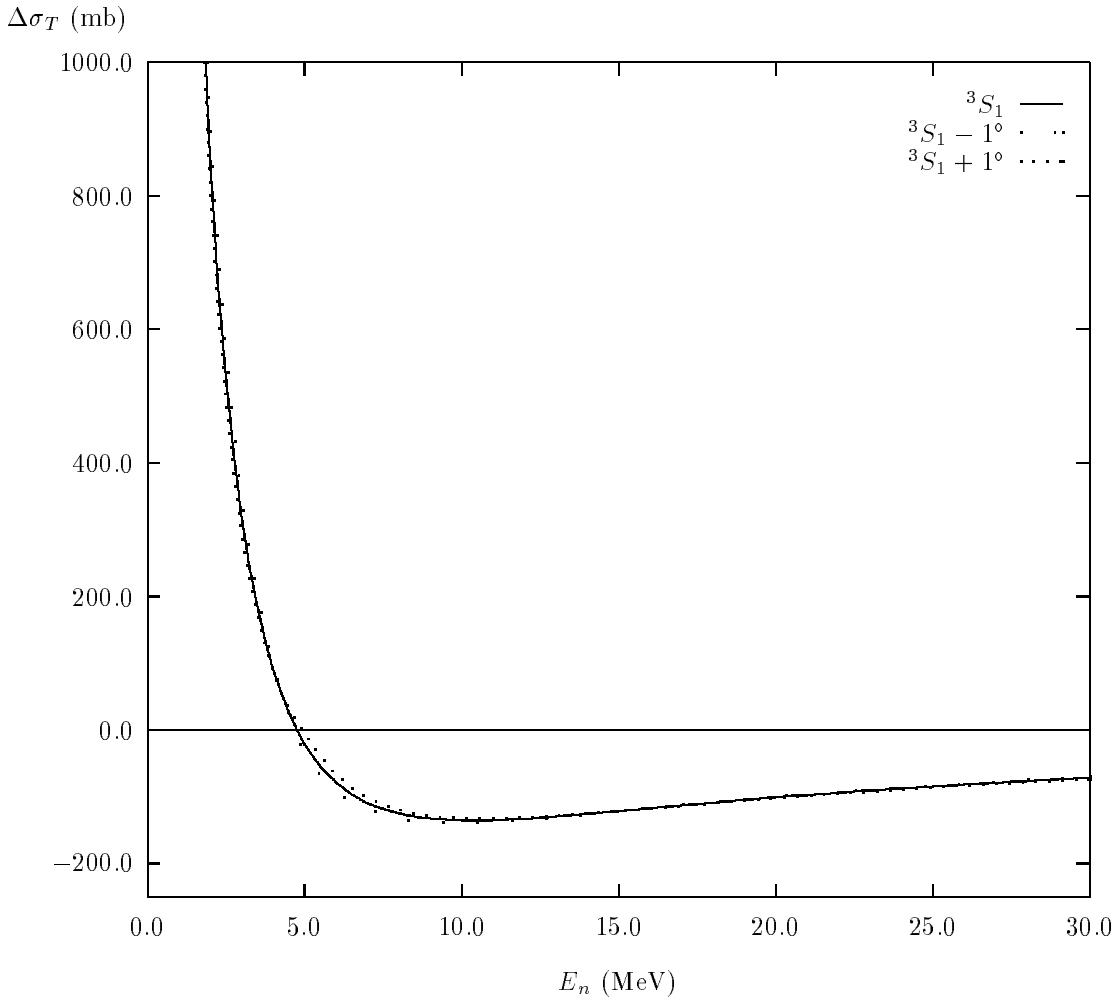

Figure 2.13: Sensitivity of $\Delta\sigma_T$ to a $\pm 1°$ Variation in $^3S_1$ Using Arndt SP89

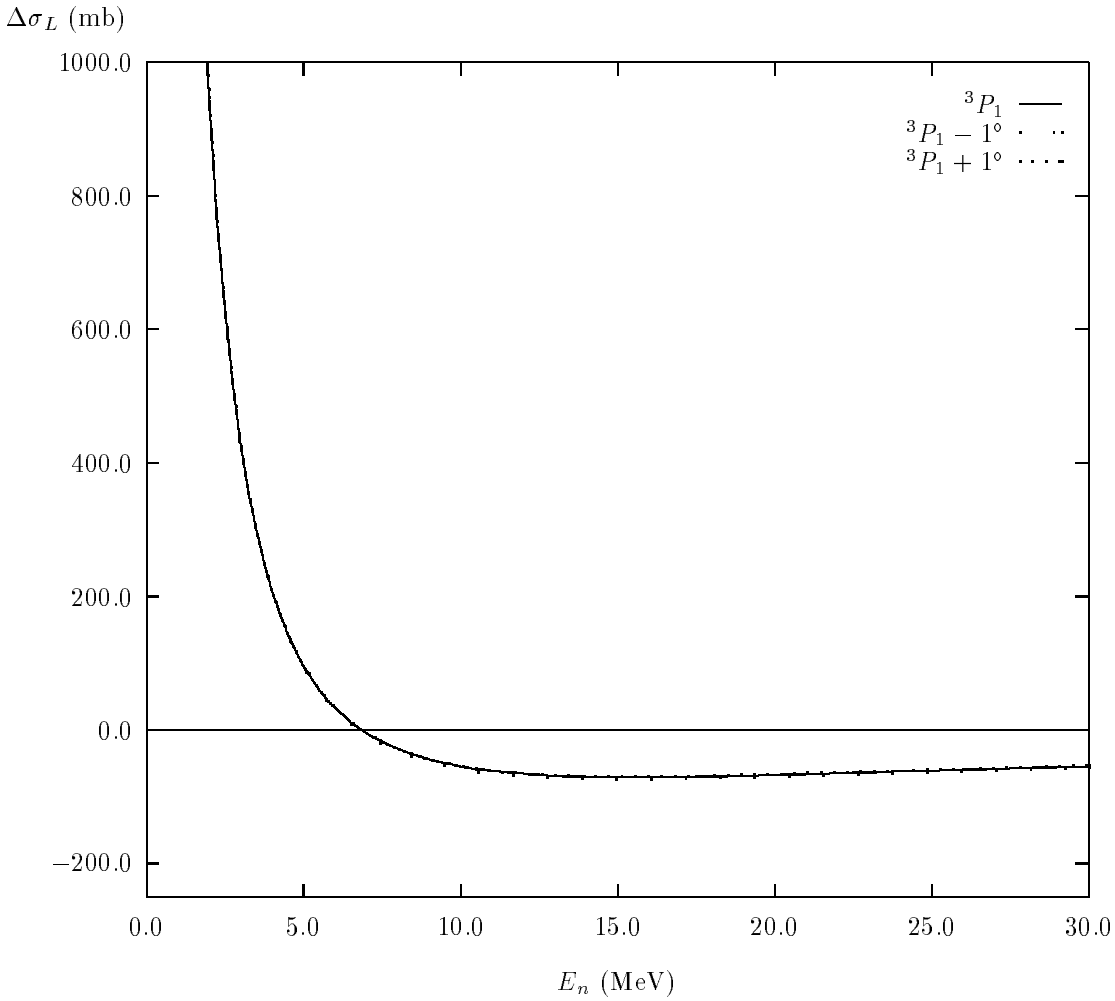

Figure 2.14: Sensitivity of $\Delta\sigma_L$ to a $\pm 1°$ Variation in $^3P_1$ Using Arndt SP89

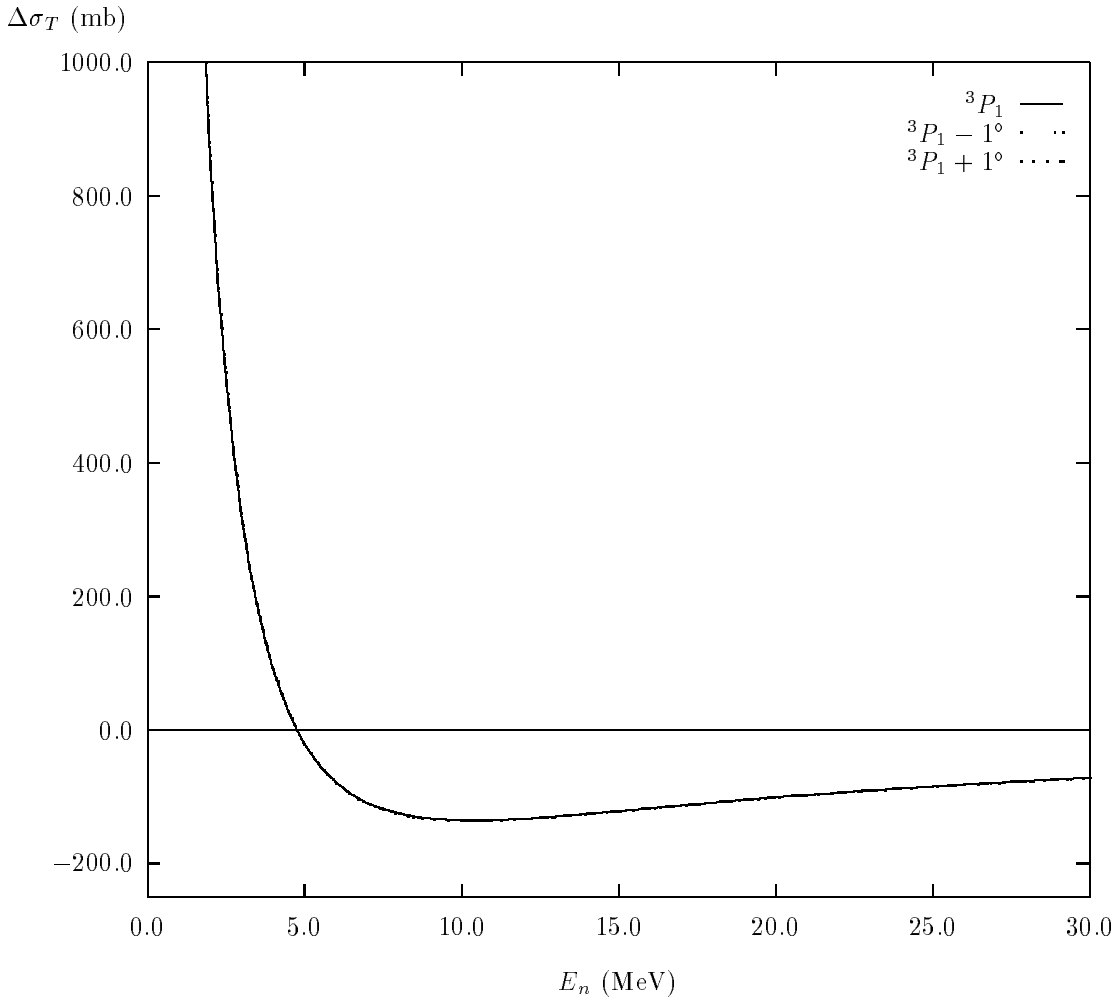

Figure 2.15: Sensitivity of $\Delta\sigma_T$ to a $\pm 1°$ Variation in $^3P_1$ Using Arndt SP89

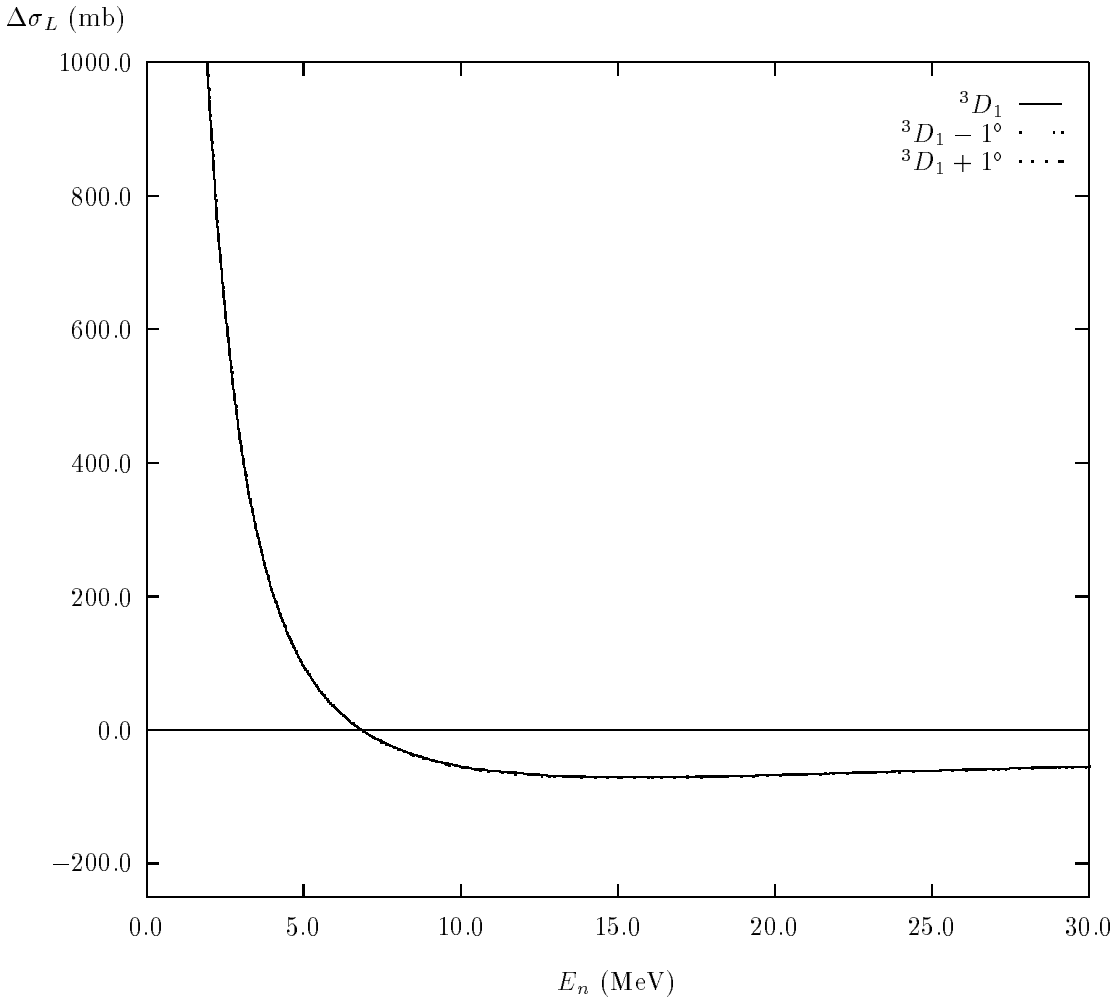

Figure 2.16: Sensitivity of $\Delta\sigma_L$ to a $\pm 1°$ Variation in $^3D_1$ Using Arndt SP89

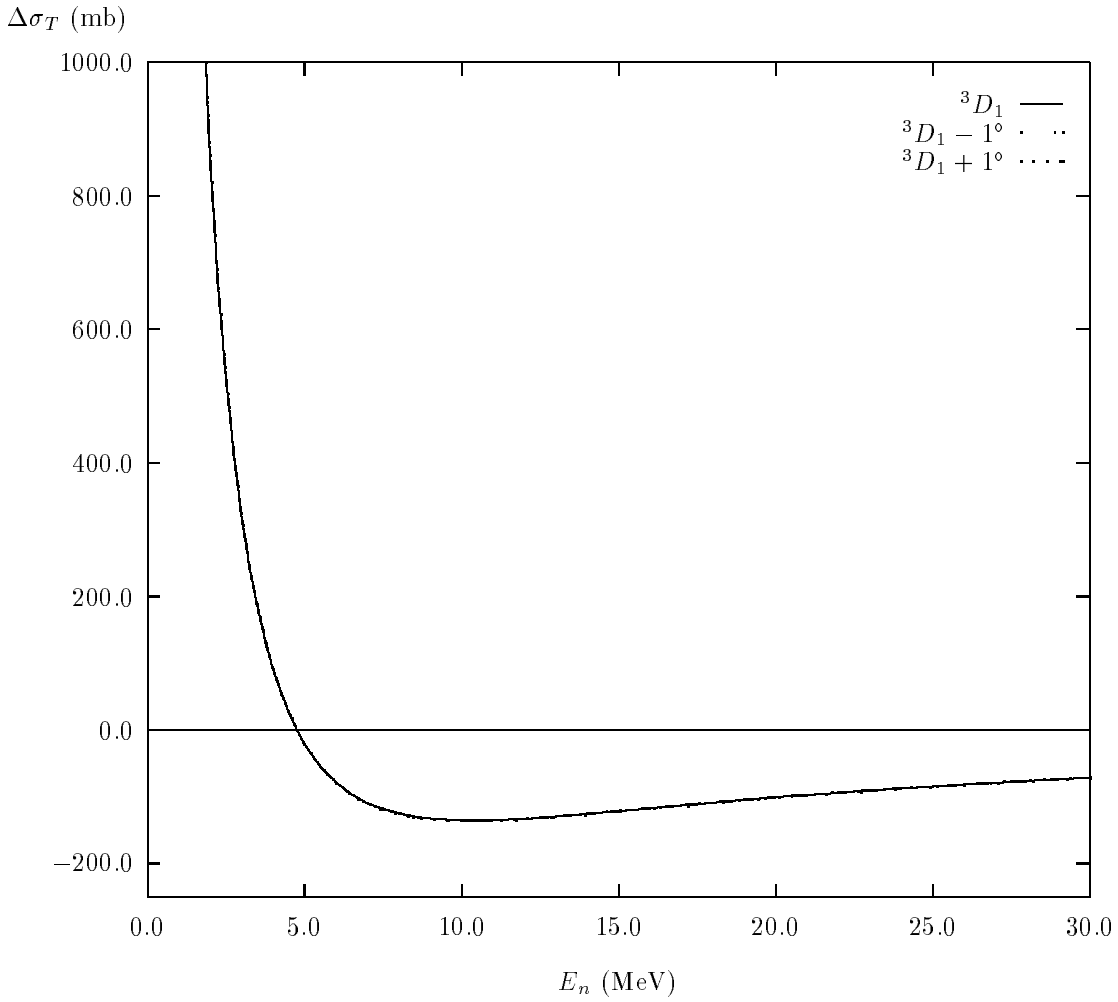

Figure 2.17: Sensitivity of $\Delta\sigma_T$ to a $\pm 1°$ Variation in $^3D_1$ Using Arndt SP89

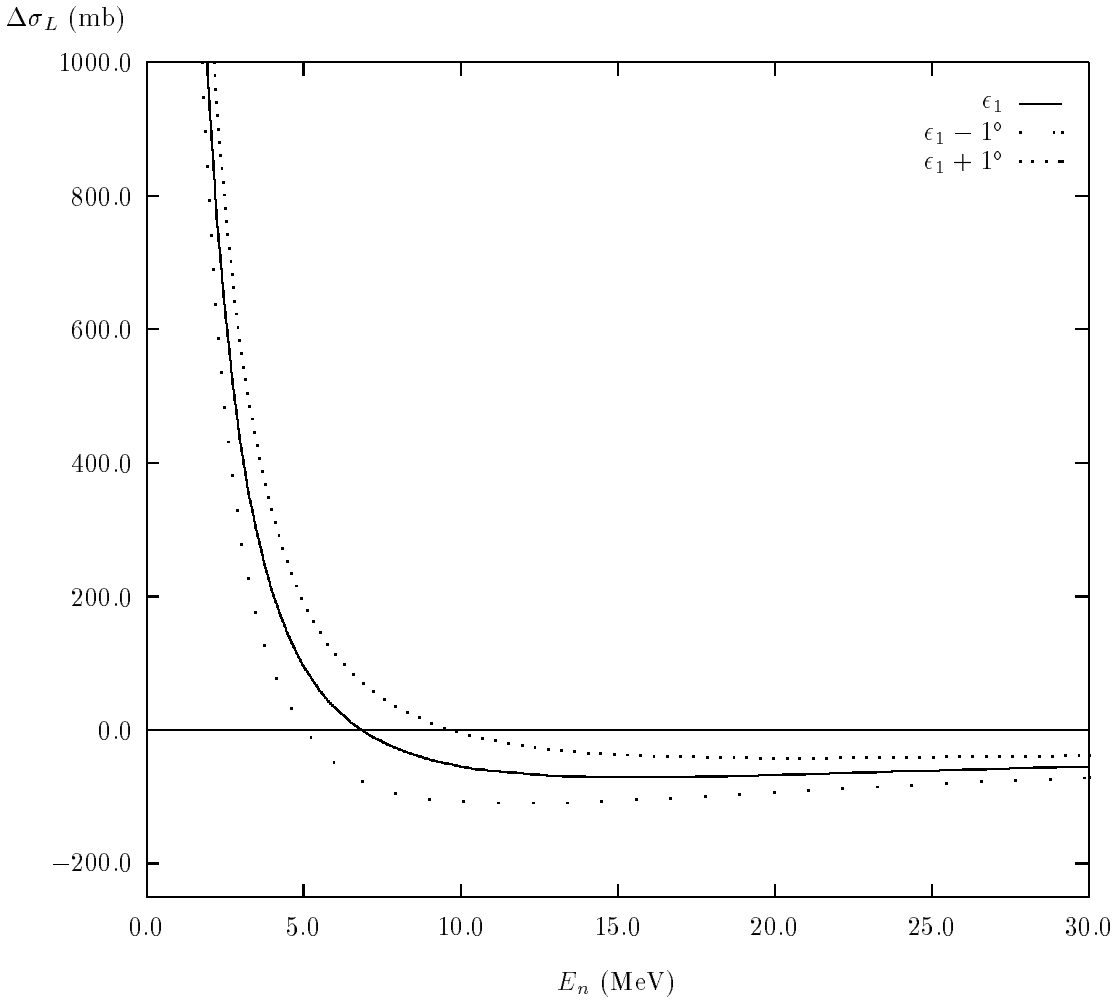

Figure 2.18: Sensitivity of $\Delta\sigma_L$ to a $\pm 1°$ Variation in ϵ_1 Using Arndt SP89

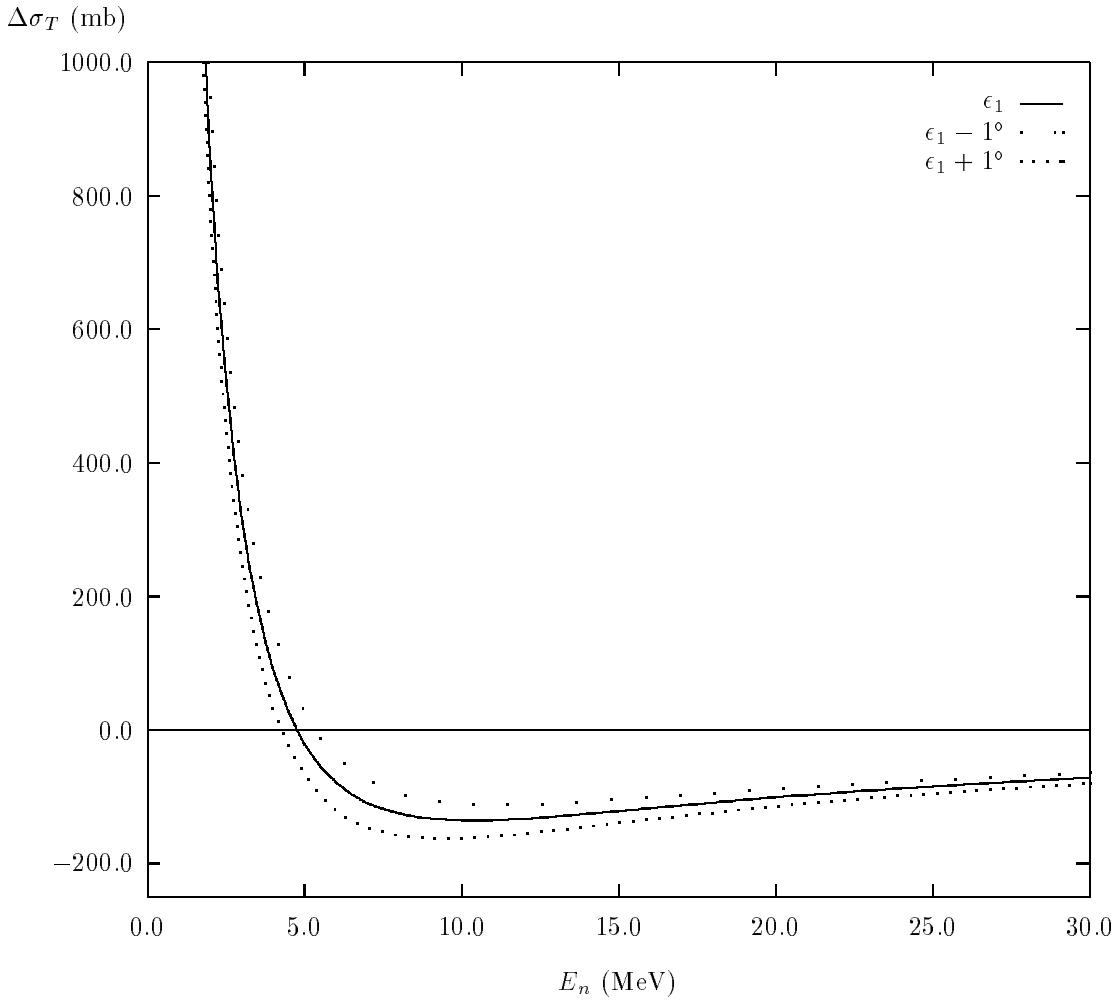

Figure 2.19: Sensitivity of $\Delta\sigma_T$ to a $\pm 1°$ Variation in ϵ_1 Using Arndt SP89

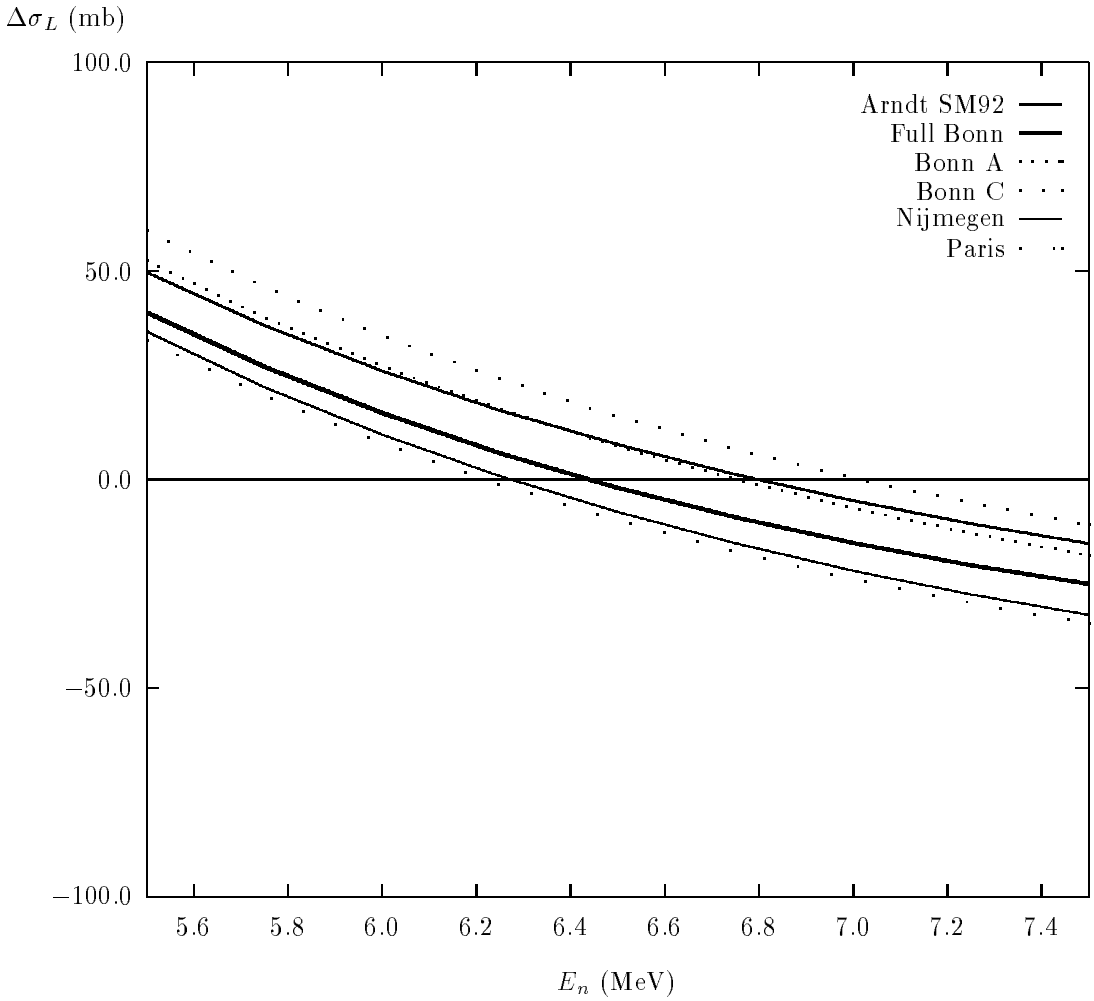

Figure 2.20: Zero-Crossing Predictions for $\Delta\sigma_L$

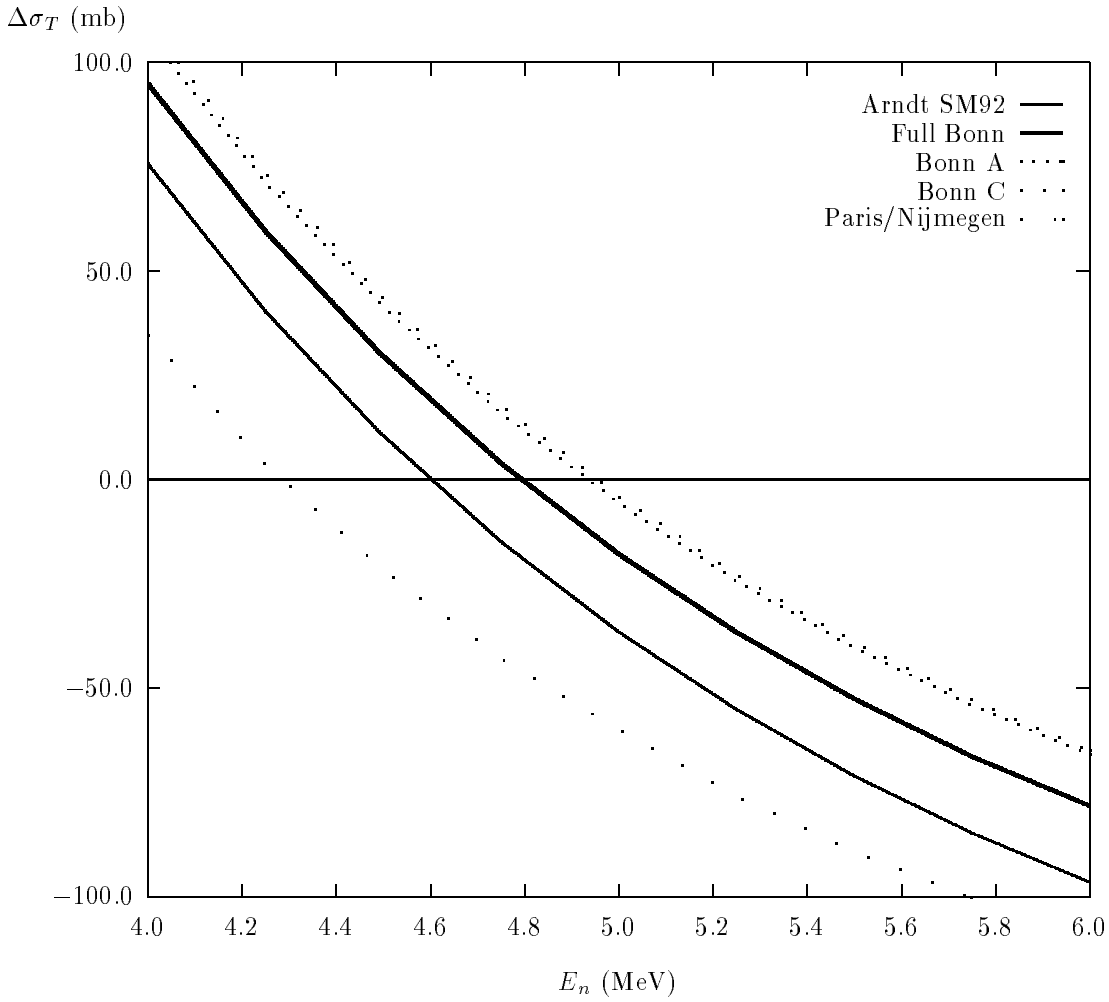

Figure 2.21: Zero-Crossing Predictions for $\Delta\sigma_T$

Chapter 3

Experimental Apparatus

3.1 Charged-Particle Beam

Since it is not possible to accelerate neutral particles directly, polarized neutron beams must be produced as secondary beams from charged-particle reactions. In this experiment, the charged-particle beam consists of polarized protons. The beam is created by an ion source capable of producing nuclear spin-polarized beams of negative hydrogen ions. The beam must be transported to the accelerator where its energy is increased and then to the neutron production target where a polarized neutron beam is created via the ^{3}H($\vec{\text{p}}$,$\vec{\text{n}}$)^{3}He reaction. In addition, the spin direction of the beam must be set to its proper orientation.

3.1.1 Polarized Ion Source

The polarized proton beam used in this experiment is produced in the TUNL Atomic Beam Polarized Ion Source [Cle89]. The ABPIS is capable of producing high-intensity beams of vector polarized protons, or vector or tensor polarized deuterons. It is an atomic beam source and it uses an electron cyclotron resonance (ECR) ionizer. Positive beams are extracted directly from the ionizer, while negative beams for acceleration by the tandem Van de Graaff are produced by passing the positive beam through a cesium charge-exchange oven. The source can produce negative hydrogen beams with microampere intensities and polarizations of approximately 60%. The entire source rests on a high-voltage platform biased to -72 kV to provide the beam with

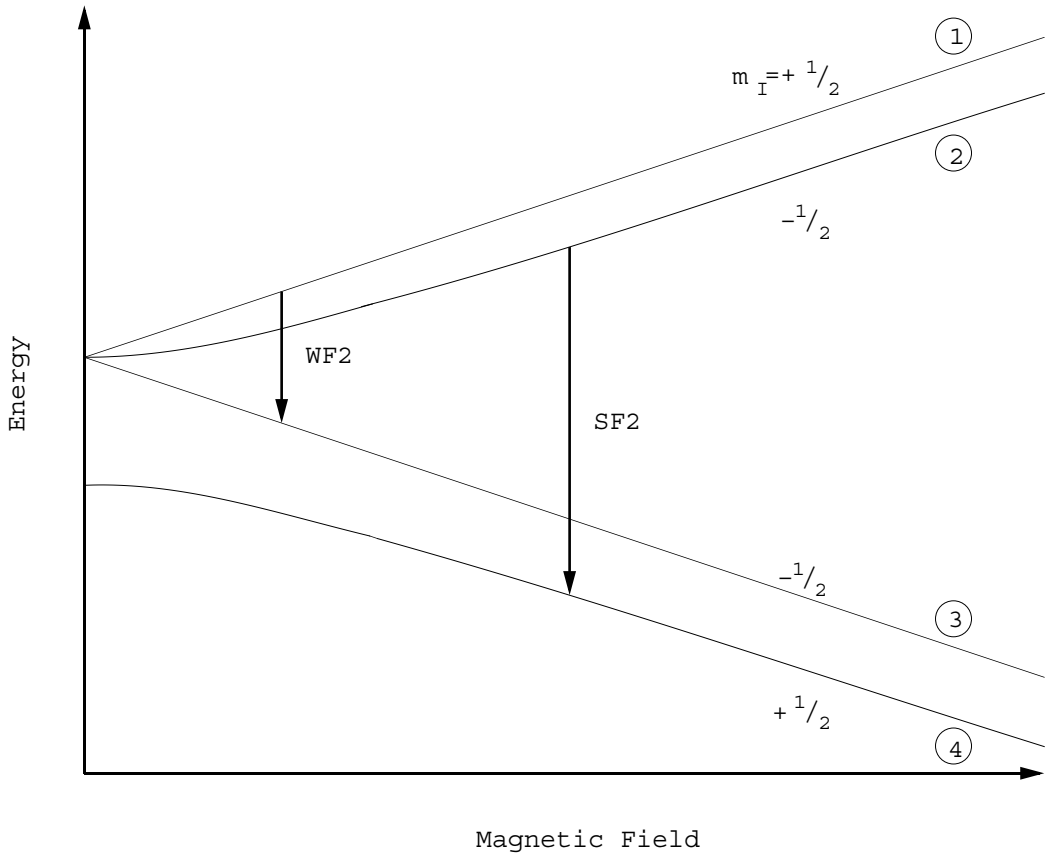

Figure 3.1: Energy Level Diagram for the Hydrogen Atom

sufficient energy to be transported to the accelerator.

The polarized ion source produces nuclear polarization in a neutral atomic beam through a combination of two sextupole magnets and two adiabatic fast-passage transition units. The atomic beam is created by a dissociator which uses an RF discharge to break the molecular bonds of hydrogen. The atomic beam sprays out of a copper nozzle and passes through two sextupole magnets. The nozzle is cryogenically cooled and continuously coated with nitrogen to reduce molecular recombination. Atomic beam type polarized ion sources make use of the separation in energy of the magnetic substates of the hydrogen atom in a magnetic field (Figure 3.1). The magnetic field of a sextupole increases as a linear function of radial distance, thus focusing the hydrogen states labeled 1 and 2, and defocusing states 3 and 4. This effect is used to produce atomic polarization. Nuclear polarization is then obtained by using one

of the two transition units. The first transition unit operates with a strong magnetic field and is called SF2, while the second operates with a weak magnetic field and is called WF2. SF2 consists of a DC magnetic field of approximately 100 G and an oscillating field with a frequency of 1450 MHz. This unit produces a transition from state 2 to state 4, giving a positive nuclear polarization along the $\hat{z}$-direction, P_z, defined by

$$P_z = \frac{N_+ - N_-}{N_+ + N_-} \tag{3.1}$$

where N_+ and N_- are the numbers of atoms with nuclear spin projections $+1/2$ and $-1/2$. WF2 consists of a DC magnetic field of approximately 10 G and an RF field with a frequency of approximately 15 MHz. This unit causes a transition from state 1 to state 3, giving a negative P_z. The transition units can be rapidly toggled on and off by modulating the RF supplies, allowing the beam polarization to be quickly reversed. The spin state produced by SF2 will be referred to as spin *up*, while that produced by WF2 will be called spin *down*.

After exiting from the sextupoles and transition units, the atomic beam is ionized by the ECR ionizer. This type of ionizer uses a plasma driven by microwave radiation to strip the electrons from the neutral hydrogen atoms. The plasma consists mostly of nitrogen introduced into the ionizer through a mass-flow controller. Electrons from this buffer gas are excited to high energy by the microwaves to perform the task of ionization. The plasma is confined in the radial direction by permanent magnets in a sextupole configuration and in the axial direction by two solenoids. Electrostatic lenses extract and focus the beam from the ionizer. Following the ionizer, a cesium oven converts the H^+ beam to H^- through double charge exchange with an efficiency of approximately 10%. The beam is then accelerated to 26 keV after which it passes through the Wien filter where the spin direction is rotated (Section 3.1.3). Upon leaving the Wien filter, the beam receives an additional 46 keV acceleration.

3.1.2 Acceleration and Transport

The beam produced by the polarized ion source, having an energy of approximately 72 keV,[1] is analyzed by a magnet with a 30° deflection. This angle aligns the direction

[1]Since charge exchange occurs in the cesium oven, the net acceleration increases the beam energy by $2eV_{Cs}$, where V_{Cs} is the voltage applied to the Cs oven, typically a few hundred volts.

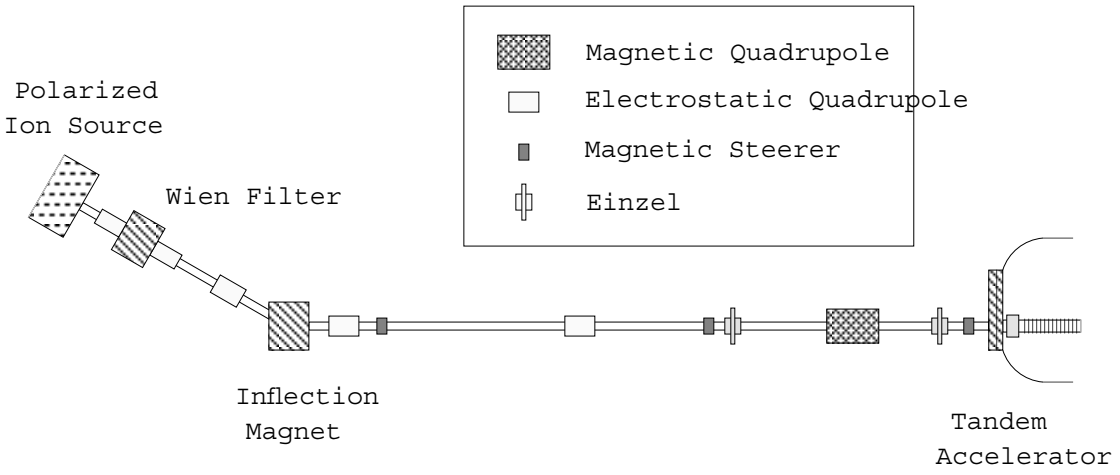

Figure 3.2: Low Energy Beam Transport

of the beam with the axis of the accelerator. Magnetic steerers are manually tuned to control the beam position, while a combination of three electrostatic quadrupole triplets, two einzels lenses, and one magnetic quadrupole doublet focuses the beam into the low energy end of the accelerator (Figure 3.2). Typically, beam currents of about 4 μA are obtained on the low energy Faraday cup.

The accelerator is a tandem Van de Graaff, High Voltage Engineering Model FN. A tandem accelerator operates by accelerating a negative beam (in this case H^-) toward a positively charged terminal, changing the charge of the beam, and then accelerating the positive beam (H^+) away from the terminal [VdG60], giving the beam an energy of $2eV_{Terminal}$. The charge state of the beam is changed by passing it through a thin carbon foil which strips away the electrons. In this experiment, a foil with a thickness of approximately 5 $\mu g/cm^2$ is used. The terminal of the accelerator is biased by two National Electrostatics Corporation (NEC) Pelletron charging chains. The chains consist of aluminum pellets joined by nylon links. The chains are mounted on pulleys driven by motors so that they run continuously between the terminal and each end of the accelerator. Charge is induced on the pellets by high-voltage DC supplies at the ground potential ends and is removed in the terminal. A corona current feedback system regulates the voltage of the terminal to keep the energy of the beam constant. The accelerator is contained in a pressure vessel filled with a mixture of carbon dioxide, nitrogen, and sulfur hexafluoride. The beam is transmitted

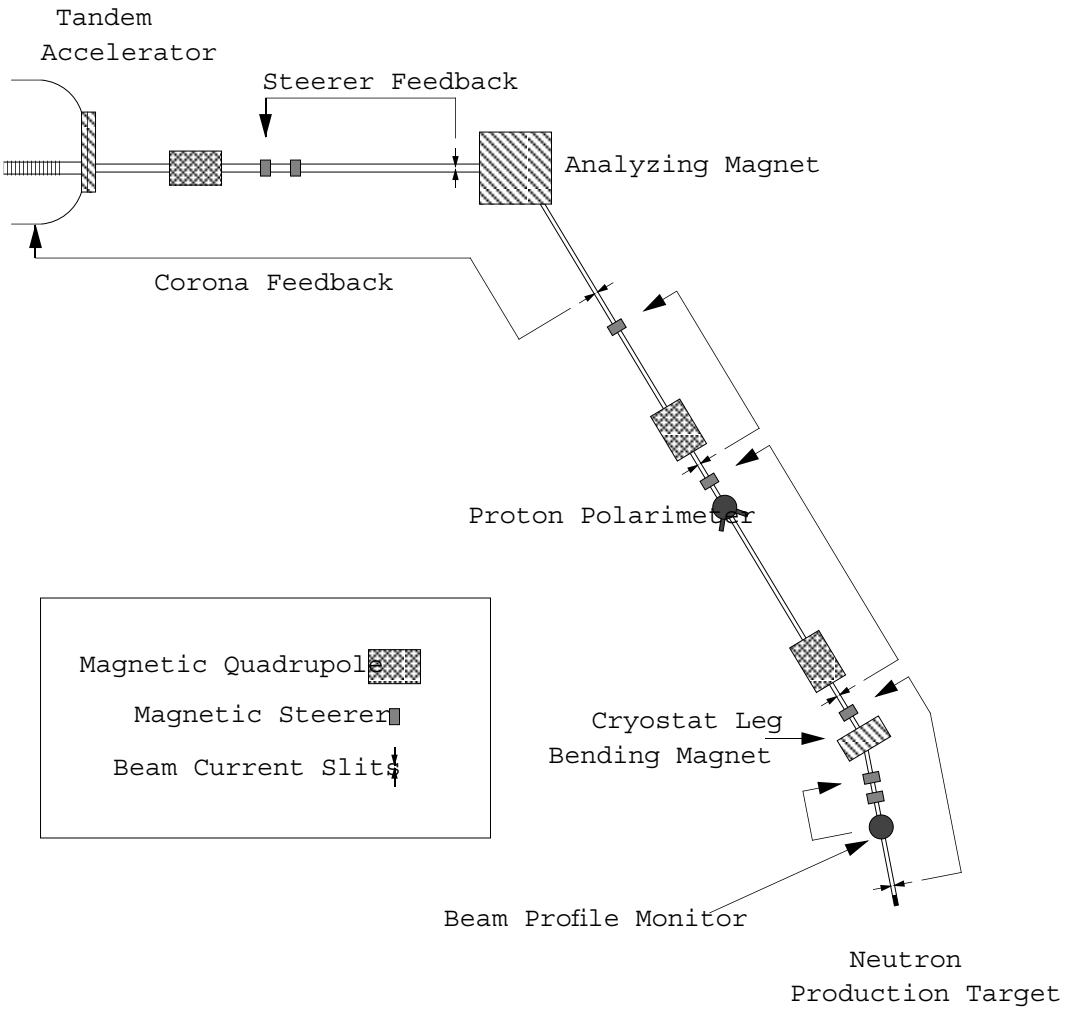

Figure 3.3: High Energy Beam Transport

through a series of four evacuated acceleration tubes, consisting of alternating glass and stainless steel sections. The efficiency for transporting the beam through the accelerator typically ranges from 55% at the lowest energies used in this experiment to 70% at the highest.

Upon leaving the accelerator, the proton beam must be transported to the neutron production target (Figure 3.3). The beam is analyzed by passing through the switching magnet with a deflection of 59°. The field of the magnet is regulated by feedback from a nuclear magnetic resonance probe. Currents from horizontal slits placed at the exit of the magnet feedback to the corona circuit of the accelerator, keeping the

energy of the beam constant. A final bending magnet (cryostat leg bending magnet) directs the beam toward the neutron production target. The beam is focused by three magnetic quadrupole doublets. A carbon-foil polarimeter allows the measurement of the beam polarization (Section 3.2). Most of the beam steering between the exit of the accelerator and the cryostat leg bending magnet is accomplished by three sets of slit feedback loops. These feedback loops keep the beam centered on the slits in the horizontal plane by steering the beam such that the difference in current from the left slit and the right slit is zero. Similarly, the beam is centered in the vertical plane using currents from the up and down slits [Gou84]. The first feedback loop keeps the beam centered at the entrance to the analyzing magnet. The second centers the beam at the entrance to the polarimeter, and the third centers the beam at the entrance to the cryostat leg bending magnet. The size of the slit openings can be adjusted to fit the size of the beam.

After the cryostat leg bending magnet, the beam is transported approximately 2 m to the neutron production target. A NEC beam profile monitor allows the shape of the beam to be viewed on an oscilloscope. In addition, signals from the beam profile monitor are read into the data acquisition system and used to steer the beam so that its centroid is centered on the beam pipe (Section 3.6). A final slit feedback loop holds the beam centered on the neutron production target. This set of slits is a fixed quad collimator and is described in Section 3.3.1. Since the proton beam must approach the cryostat quite closely, it must be shielded from the field of the superconducting magnet. For this reason, the last 1.2 m of the beam pipe is made of soft iron with 5.6 mm walls. Inside of the pipe are two concentric cylinders of a high permeability alloy,[2] 1 mm thick. The beam current striking the neutron production target is integrated using a Brookhaven Nuclear Instruments 1000 whose output is a series of pulses with a frequency proportional to the current. These pulses are converted to a NIM level signal by a Ortec 416A gate and delay generator and then the width is set with a LeCroy 222 gate and delay before being sent to the data acquisition electronics (Figure 3.4). The analog output of the current integrator goes to a discriminator with upper and lower levels. The discriminator sends an inhibit signal to the computer to stop data acquisition when the beam current is outside of the window defined by the upper and lower levels. The beam current on target is

[2]CO-NETIC AA, Magnetic Shield Corporation, Perfection Mica Company.

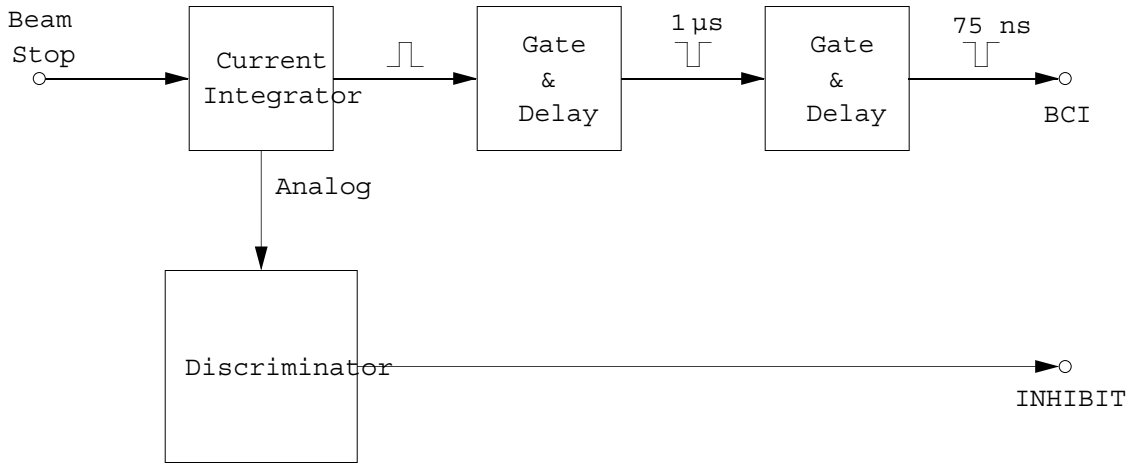

Figure 3.4: Beam Current Integration Electronics

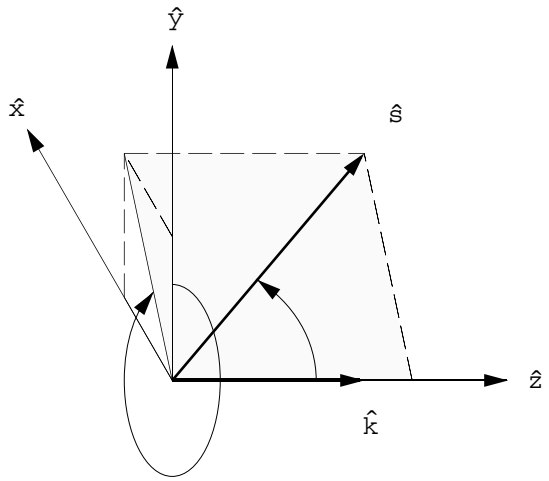

Figure 3.5: Madison Convention Coordinate System

typically 0.5–1.5 μA.

3.1.3 Spin Transport

Just as important as transporting the polarized proton beam to target is having it arrive with the proper spin orientation. The Madison convention [Sat71] defines a coordinate system for describing the polarization of the beam (Figure 3.5). In order

to produce the transversely polarized neutron beam required for the $\Delta\sigma_T$ measurements, the proton beam must arrive at the neutron production target with its spin oriented transverse to the beam direction ($\hat{z}$) and in the horizontal plane ($\hat{x}$ direction). Although the proton beam emerges from the polarized ion source with a longitudinal spin orientation, its direction can be changed by the Wien filter spin precessor. Propagation of the beam through dipole bending magnets can affect the spin direction and must be taken in to account in setting the spin precessor. For beams polarized in the $\hat{y}$ direction (transverse vertical), spin precession does not occur in the bending magnets and the only consideration is to properly set the initial spin direction at the polarized ion source. For beams polarized in the $\hat{x}$ direction (transverse horizontal), however, spin precession does occur in the bending magnets and must be compensated for by setting the spin direction at the source. This is the case for the $\Delta\sigma_T$ measurements as the spin of the beam must be in the same direction as that of the polarized target, which is determined by the superconducting magnet.

When a beam of spin 1/2 particles is bent by a magnet, the spin direction is not necessarily changed by the same angle as the propagation direction. A spin component normal to the magnetic field will precess. If the angle of deflection is θ, and the angle of spin precession is α, it can be shown that the two angles are related by the g-factor of the particle [Lew87].

$$\alpha = g\theta \tag{3.2}$$

For the special case $g = 1$, the spin precession angle is the same as the deflection angle, maintaining the relationship between the beam propagation direction and the spin direction. For $g \neq 1$, the angle between the propagation and spin directions, β, changes. In the case of a proton beam with spin oriented in the x-z plane, β increases according to

$$\beta^{+}_{final} = \beta^{+}_{initial} + (g_p - 1)\theta \tag{3.3}$$

where $g_p = 2.7927$. For a negative hydrogen ion beam, however, the beam deflection is in the opposite direction.

$$\beta^{-}_{final} = \beta^{-}_{initial} - (g_p + 1)\theta \tag{3.4}$$

Since the spin precession depends only on the angle of deflection, the spin orientation at any point along the beam path can be calculated (Figure 3.6). Because the

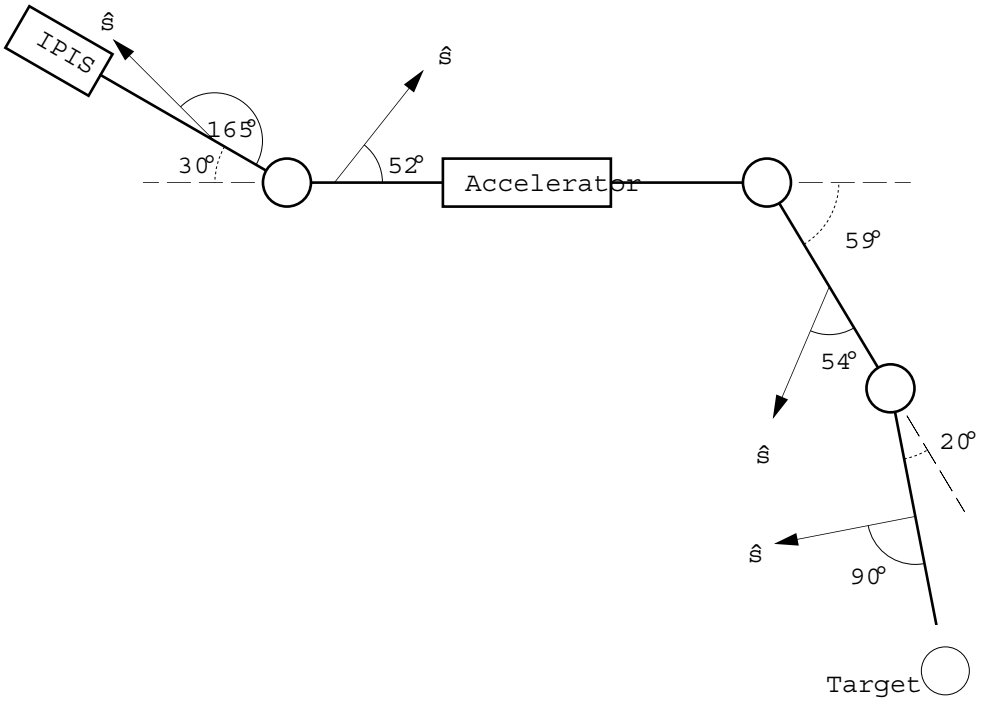

Figure 3.6: Spin Precession for a Proton Beam, Transverse Horizontal on Target

cryostat leg bending magnet is located between the polarimeter and the target, there is a difference in spin angle between the two. The deflection of the magnet has been determined by surveying to be 19.82±0.04°. This gives a difference in spin angle of 35.53±0.07°. All beam polarization measurements made with the carbon-foil polarimeter (Section 3.2) when the spin is transverse horizontal on target must then be corrected by cos(35.53°).

Since the beam produced by the polarized ion source is polarized along the beam direction, a spin precessor is needed to produce transverse polarization. The Wien filter[3] performs this task with crossed electric and magnetic fields. The magnetic field precesses the spin, while the electric field compensates for the deflection to keep the beam straight. Electrostatic quadrupole doublets reduce the size of the beam so that all particles traverse nearly the same magnetic field. The Wien filter can be mechanically rotated about the beam direction, allowing any spin orientation to be achieved. The Wien filter has been calibrated by measuring the polarization in the $\hat{x}$ direction at the polarimeter as a function of magnetic field (Figure 3.7). The non-linearity observed at the higher fields is due to a problem with the gaussmeter used to measure the magnetic field.[4] For this reason, only field settings below 1200 G are used for spin precession. The portion of the curve from 0 to −1200 G has been fit to a sine function

$$P_x = P_x^{max} \sin\left(\frac{2\pi B}{B_0} + \beta_0\right) \tag{3.5}$$

where $B_0 = 1653.12$ G and $\beta_0 = 2.3224$. From this data, Wien filter magnetic field and mechanical angle settings, B and ϕ, can be determined for any spin orientation.[5] Table 3.1 lists the settings which are important for this experiment.

3.2 Charged-Particle Polarimeter

Since $\Delta\sigma_T$ is proportional to the neutron polarization, the beam polarization must be determined for each measurement. Although it is difficult to measure the neutron beam polarization directly, it is relatively easy to monitor the polarization of the

[3] ANAC model 2170 Spin Precessor.

[4] The gaussmeter has since been replaced. The new unit does not exhibit this behavior.

[5] It should be noted that a magnetic field is in the $\hat{y}$-direction ($\phi = 0°$) rotates the spin orientation in the x-z plane.

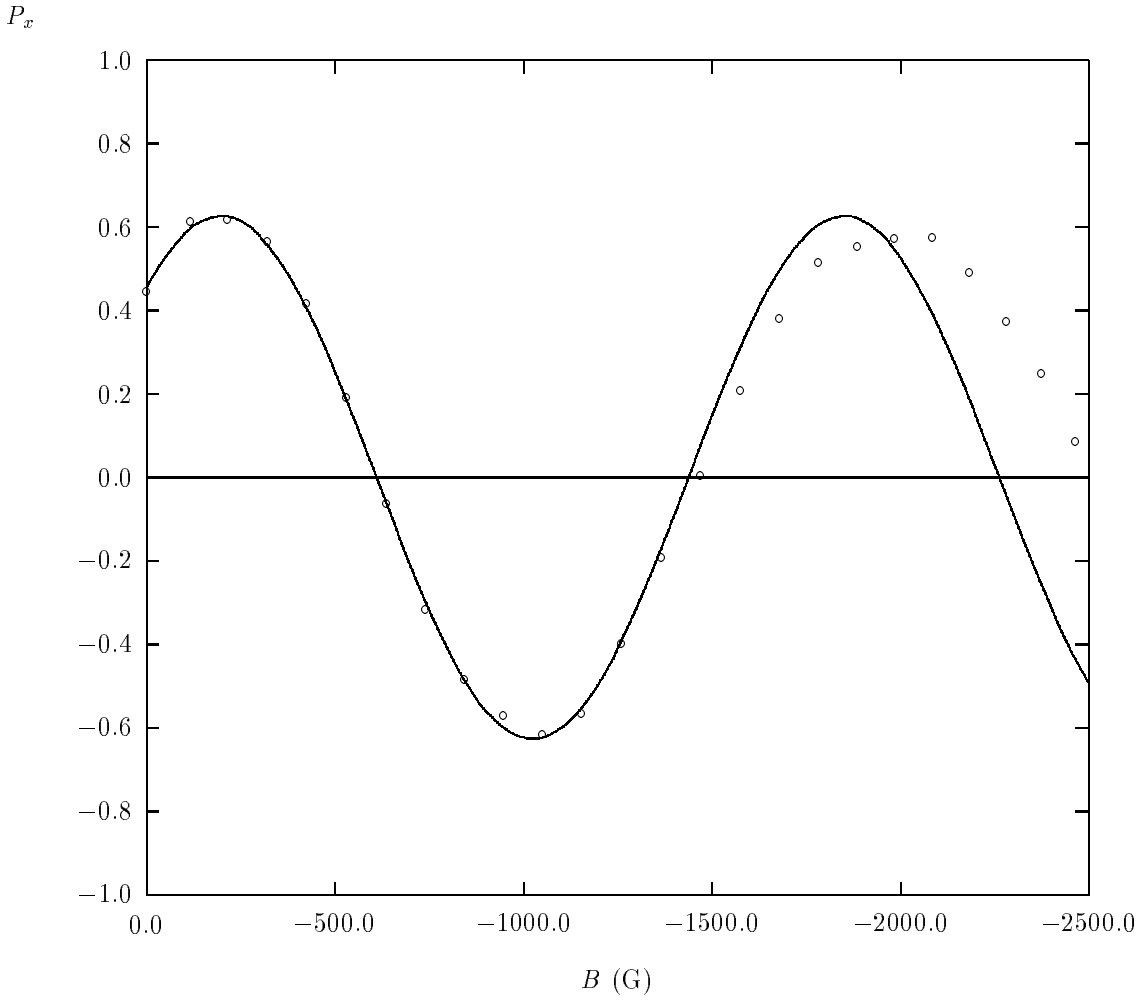

Figure 3.7: Wien Filter Calibration for the 59° Beam Line as Measured by the Proton Polarimeter

ϕ	B (G)	Spin Orientation
0°	−861.17	$-\hat{x}$ (Target)
0°	−1024.32	$-\hat{x}$ (Polarimeter)
0°	−34.61	$+\hat{x}$ (Target)
0°	−197.76	$+\hat{x}$ (Polarimeter)
+90°	−413.28	$-\hat{y}$
+90°	+413.28	$+\hat{y}$
0°	+378.67	$-\hat{z}$ (Target)
0°	+215.52	$-\hat{z}$ (Polarimeter)
0°	−447.89	$+\hat{z}$ (Target)
0°	−611.04	$+\hat{z}$ (Polarimeter)

Table 3.1: Wien Filter Settings

charged-particle beam and then relate this value to the neutron beam using known polarization-transfer coefficients, $K_y^{y'}$. For this reason, a carbon-foil polarimeter is used to monitor the polarization of the proton beam during $\Delta\sigma_T$ measurements. This polarimeter has been calibrated by a neutron polarimeter in separate measurements (Section 4.2).

The polarimeter consists of a carbon foil and two solid state charged-particle detectors contained within a small scattering chamber (Figure 3.8). The chamber is made of a cylindrical body with two arms as particle flight paths in order to minimize the internal volume and thus reduce the need for vacuum pumping. The chamber is constructed of aluminum with the arms welded to the body. Dependex flanges are used at the entrance and exit of the chamber and at the ends of the arms. The detectors are mounted on blank dependex flanges at the ends of the arms with three sets of tantalum collimators defining the scattered beams with an angular acceptance of ±3.46°. The carbon foil is 22 mm in diameter and 5 μg/cm^2 thick and is mounted on a plunger so that it can be removed from the beam when not in use. Slits in front of the polarimeter define the beam to be 12.7 mm × 12.7 mm. The slit currents are fed back to a steerer which keeps the beam centered on the entrance of the polarimeter. The detectors and all but the first set of collimators are electrically isolated to reduce noise pickup. The detectors are silicon charged-particle detectors with 300 mm^2 active

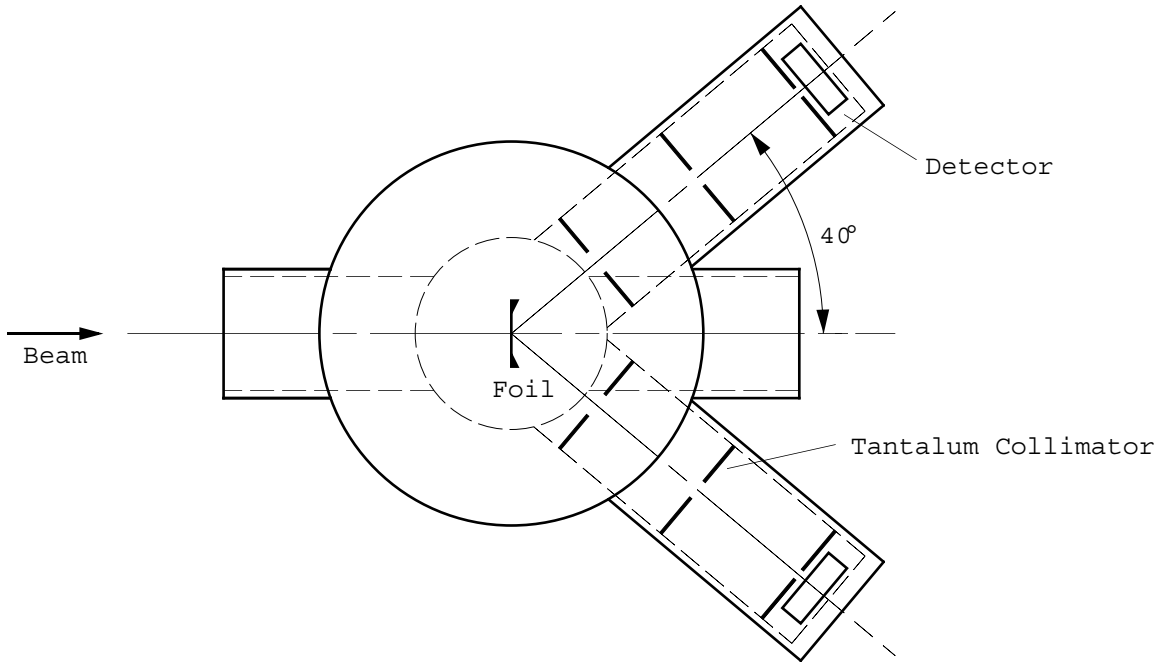

Figure 3.8: Proton Beam Polarimeter

areas and depletion depths of 1000 μm. The angle of the arms is fixed, for simplicity, at $\pm 40°$. This angle is chosen to provide a relatively large analyzing power over a range of energies for protons elastically scattered from carbon.

The signals from the detectors pass through Ortec 142 preamplifiers at the polarimeter and are then further amplified by Ortec 572 amplifiers in the control room. The unipolar outputs of the amplifiers are fed to Ortec 551 timing single-channel analyzers (TSCA). This setup is shown schematically in Figure 3.9. The TSCA windows are set to select one peak in the linear energy spectrum from the amplifiers and the outputs are sent to the data acquisition electronics. The window is set by observing the delayed output of the amplifier on an oscilloscope while triggering on the TSCA output.

When a proton beam is used, only three peaks are observed. In order of increasing energy of the detected particle they are ^{1}H(p,p)^{1}H, ^{12}C(p,p$_1$)^{12}C, and ^{12}C(p,p$_0$)^{12}C. In the case of elastic scattering from hydrogen, it is the recoiling proton which is detected. Note that because of its excitation energy of 4.44 MeV, the first excited state of carbon will not be observed at lower beam energies. The TSCA windows are

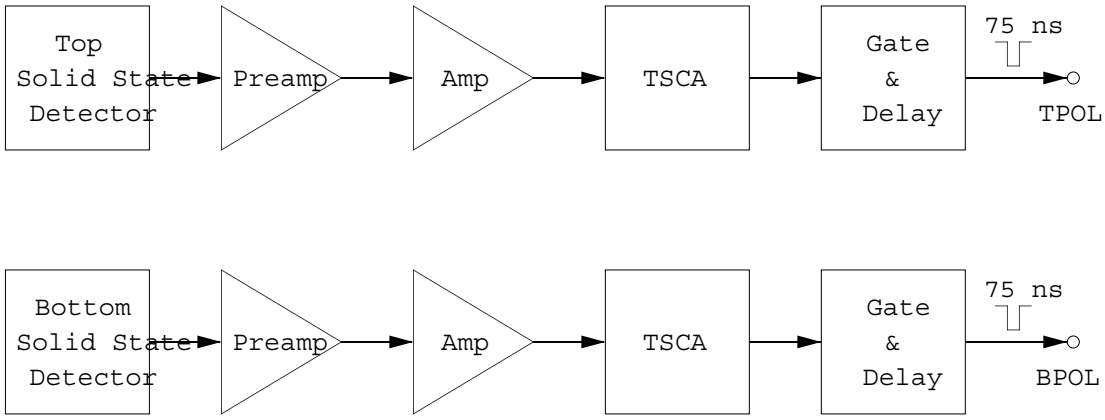

Figure 3.9: Proton Beam Polarimeter Electronics

set around the ^{12}C(p,p$_0$)^{12}C peak and the counts from both detectors are read by the data acquisition electronics into scalers. Asymmetries between the number of counts from each detector, ε_{ppol}, are then calculated for each spin state.

$$\varepsilon_{ppol} = \frac{N_L - N_R}{N_L + N_R} \tag{3.6}$$

Here, N_L and N_R refer to the number of counts in the left and right detectors by convention, although the detectors are physically up and down for most measurements. The proton beam polarization, P_p, is given by

$$P_p = \frac{\varepsilon_{ppol}}{A_y \sin\beta} \tag{3.7}$$

where A_y is the analyzing power at 40° for ^{12}C(p,p$_0$)^{12}C (Table 3.2) and β is the azimuthal angle of the spin axis in the polarimeter.[6] The analyzing powers are obtained by fitting published analyzing power data as a function of angle [Mos65, Ter68] (Section 5.1.2). The neutron beam polarization is then obtained by knowing the polarization transfer coefficient $K_y^{y'}$ for the ^{3}H($\vec{\text{p}}$,$\vec{\text{n}}$)^{3}He source reaction.

$$P_n = K_y^{y'} P_p \tag{3.8}$$

Beam polarizations have been observed to remain very constant with time [Kos90], allowing the polarization measurements to be made every 2–4 hours. Removing the

[6] Since the polarimeter is placed before the last bending magnet, the angle of the spin is not the same in the polarimeter and on target. For protons the difference is 35.53±0.07°.

E_p	A_y	ΔA_y
4.66	−0.496	0.022
5.04	−0.724	0.009
5.41	−0.535	0.024
5.78	−0.775	0.015
5.89	−0.812	0.022
6.18	−0.851	0.009
6.77	−0.520	0.009

E_p	A_y	ΔA_y
7.21	−0.278	0.015
7.55	−0.339	0.016
7.99	−0.131	0.017
8.66	−0.015	0.014
8.90	0.125	0.041
9.15	−0.010	0.015
9.60	−0.348	0.054

Table 3.2: Analyzing Powers for ^{12}C(p,p$_0$)^{12}C at $\theta_{lab} = 40°$

carbon foil between polarization measurements increases the beam current on target by approximately 40–100%, depending on the beam energy.

3.3 Neutron Beam

The polarized neutron beam is produced as a secondary beam from the polarized proton beam. The beam is produced by an essentially unshielded source and is collimated after passing through the polarized proton target. The neutron detectors are placed at 0° inside a large shield. It is important to know the characteristics of the beam including its polarization, average energy, and energy spread. In addition, it is important to determine the amount of unpolarized background in the beam and the amount of depolarization caused by the superconducting magnet used in the polarized target.

3.3.1 Neutron Beam Production

The polarized neutron beam is produced by the ^{3}H($\vec{\text{p}}$,$\vec{\text{n}}$)^{3}He reaction [Don71, Sim73]. This reaction is chosen because the threshold of 0.764 MeV makes the production of low energy neutron beams with an acceptable energy spread possible. By comparison, the ^{2}H($\vec{\text{d}}$,$\vec{\text{n}}$)^{3}He reaction [Lis75] has a positive Q value of 3.3 MeV making it difficult to produce neutron beams at 0° with energies less than 6 MeV. In addition, the ^{3}H($\vec{\text{p}}$,$\vec{\text{n}}$)^{3}He reaction has a large polarization transfer coefficient at 0° (Section 5.2). The tritium is in the form of tritiated-titanium on a 0.51 mm thick ^{58}Ni backing. A

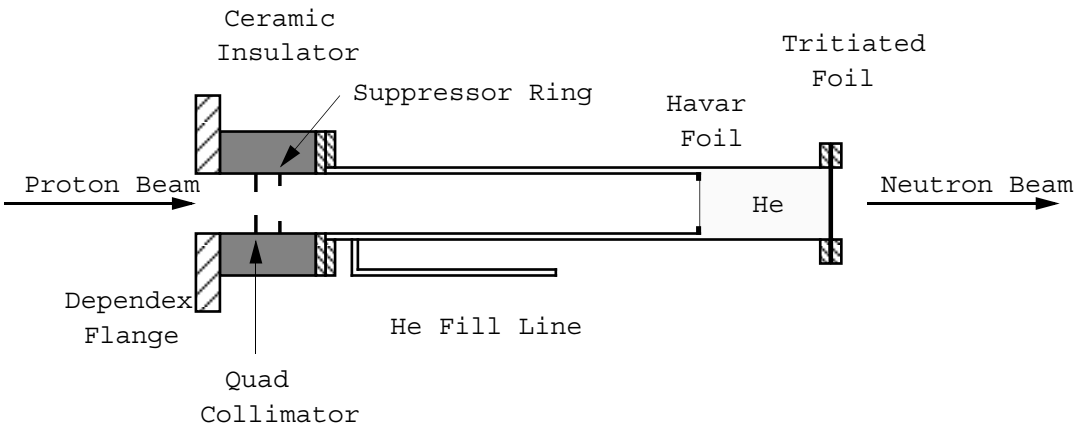

Figure 3.10: Tritiated-Titanium Foil Holder

solid compound is used instead of gaseous tritium for safety considerations. The ^{58}Ni backing stops the proton beam without producing neutrons due to the high threshold of 9.44 MeV for the ^{58}Ni(p,n)^{58}Cu reaction. To contain any tritium which might be released from the foil, as well as flakes of Ti $^3H_2$, a 1 bar helium cell with a 2.5 μm Havar entrance foil is placed in front of the tritium foil [deR89]. A four-segment tantalum collimator defines the proton beam to be 4.76 mm $\times$ 6.35 mm (vertical $\times$ horizontal) and provides feedback to a magnetic beam steerer. The foil holder, shown in Figure 3.10, is electrically isolated to allow beam current integration and a suppressor voltage of -300 V is applied to prevent leakage currents from secondary electrons. Since the number of neutrons produced is proportional to the number of protons incident on the tritiated-titanium foil, it is not necessary to measure the neutron flux directly. Because tritiated-titanium foils cannot hold as much tritium as a gas cell, the neutron count rates are low, typically of order 100 s^{-1} after being attenuated by the target and with a detector efficiency of approximately 25%.

The proton beam loses energy in passing through the havar foil, the helium gas, and the tritiated-titanium, making the energy of the neutron beam difficult to determine exactly. In addition, these losses determine the energy spread of the neutron beam. For these reasons, it is important to both estimate the energy losses for the proton beam and to directly measure the energy of the neutron beam. The energy losses are calculated using the FORTRAN code BABEL [Bow82]. The average energy of the beam is taken to be that of the neutrons produced half way through the tritiated-

E_p (MeV)	$\bar{E}_n$ (MeV)	ΔE_n (keV)
3.02	2.00	114.5
4.66	3.71	80.6
5.41	4.48	71.7
5.89	4.97	67.1
6.18	5.27	64.6
6.77	5.87	60.2
7.21	6.31	57.3

Table 3.3: Calculated Average Neutron Energies and Energy Widths

titanium. The energy width is taken to be the difference in energy between neutrons produced at the start and the end of the tritiated-titanium added in quadrature to the straggling of the proton beam as it passes through the havar and the helium. The straggling is estimated to be one tenth the total energy loss in these materials. The results are shown for the energies of interest in Table 3.3. To determine the neutron energy more accurately, direct measurements are needed. For this purpose, yield curves have been measured for carbon and oxygen targets for neutron energies in the vicinity of known resonances using an unpolarized beam [Nat91, Nat90]. Figure 3.11 shows the total cross section for carbon in this region, while Figure 3.12 shows the total cross section for oxygen. The carbon target is a block of graphite approximately 130 mm thick and the oxygen target is a plastic cylinder of water approximately 127 mm thick. The targets are placed between the cryostat and the collimator and the number of neutrons at 0° counted for a fixed amount of proton beam charge. The measurement is repeated with the target removed in the case of carbon, and with the target replaced by an empty plastic cylinder in the case of oxygen. The total cross section is then given by

$$\sigma_{Total} = -x \ln\left(\frac{N_{in}}{N_{out}}\right) \tag{3.9}$$

where N_{in} and N_{out} are the number of neutrons counted with the target in and out and x is the target thickness. The results of this measurement are shown in Figure 3.13 for carbon and in Figure 3.14 for oxygen. Since only the positions of the resonances are important, it is not necessary to know x accurately. Comparing the positions of the resonances with the known values gives a calibration for the relationship between

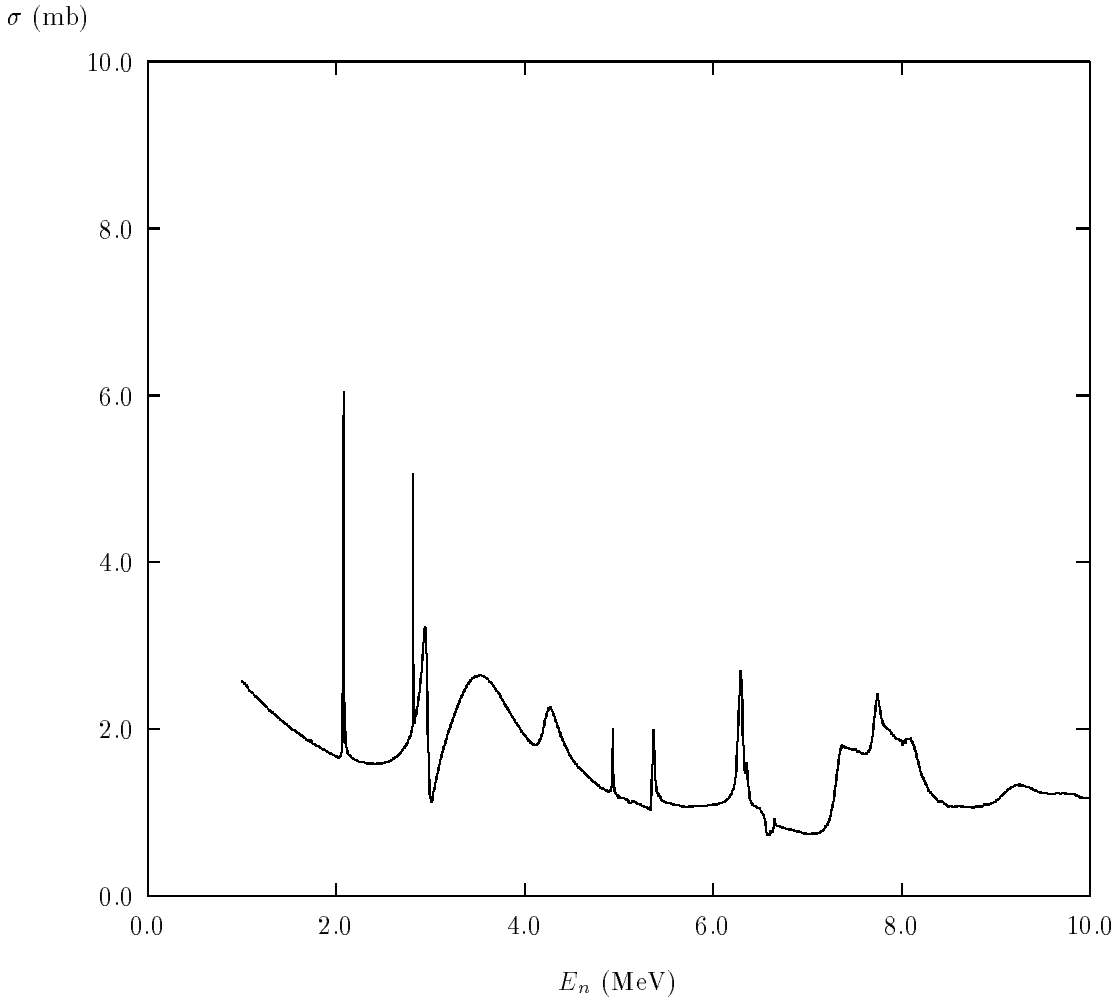

Figure 3.11: ENDF/B-VI Evaluation for the Total Neutron Cross Section of Carbon

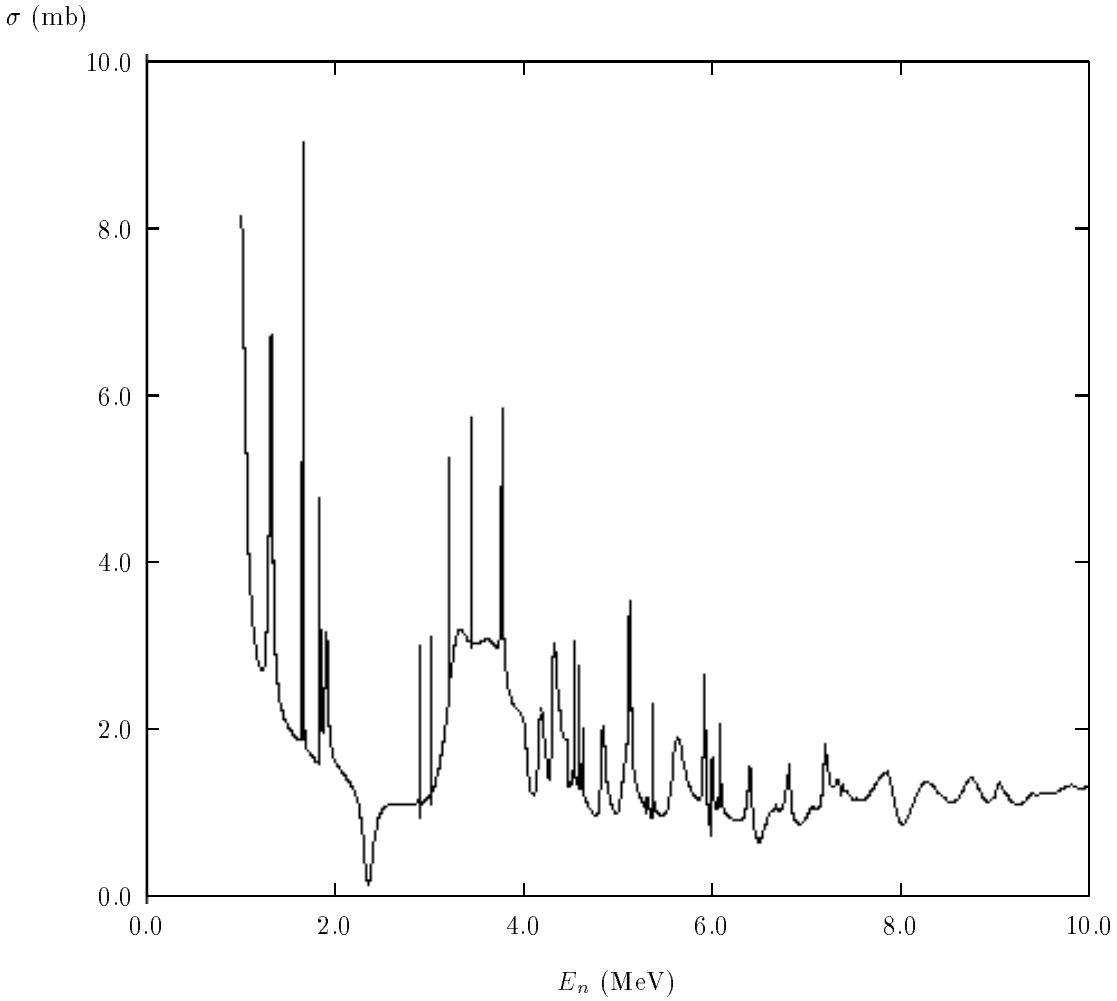

Figure 3.12: ENDF/B-VI Evaluation for the Total Neutron Cross Section of Oxygen

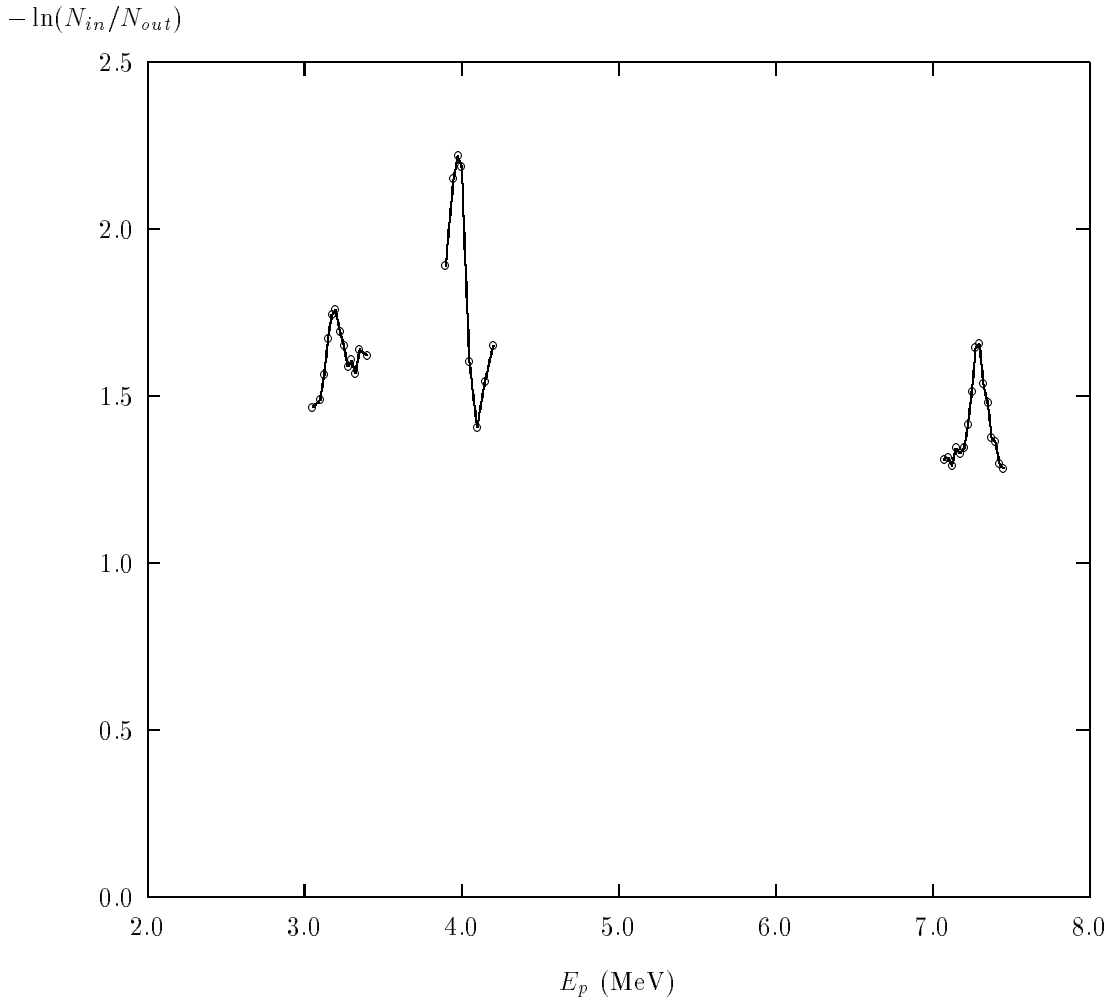

Figure 3.13: Measured Total Neutron Cross Section of Carbon

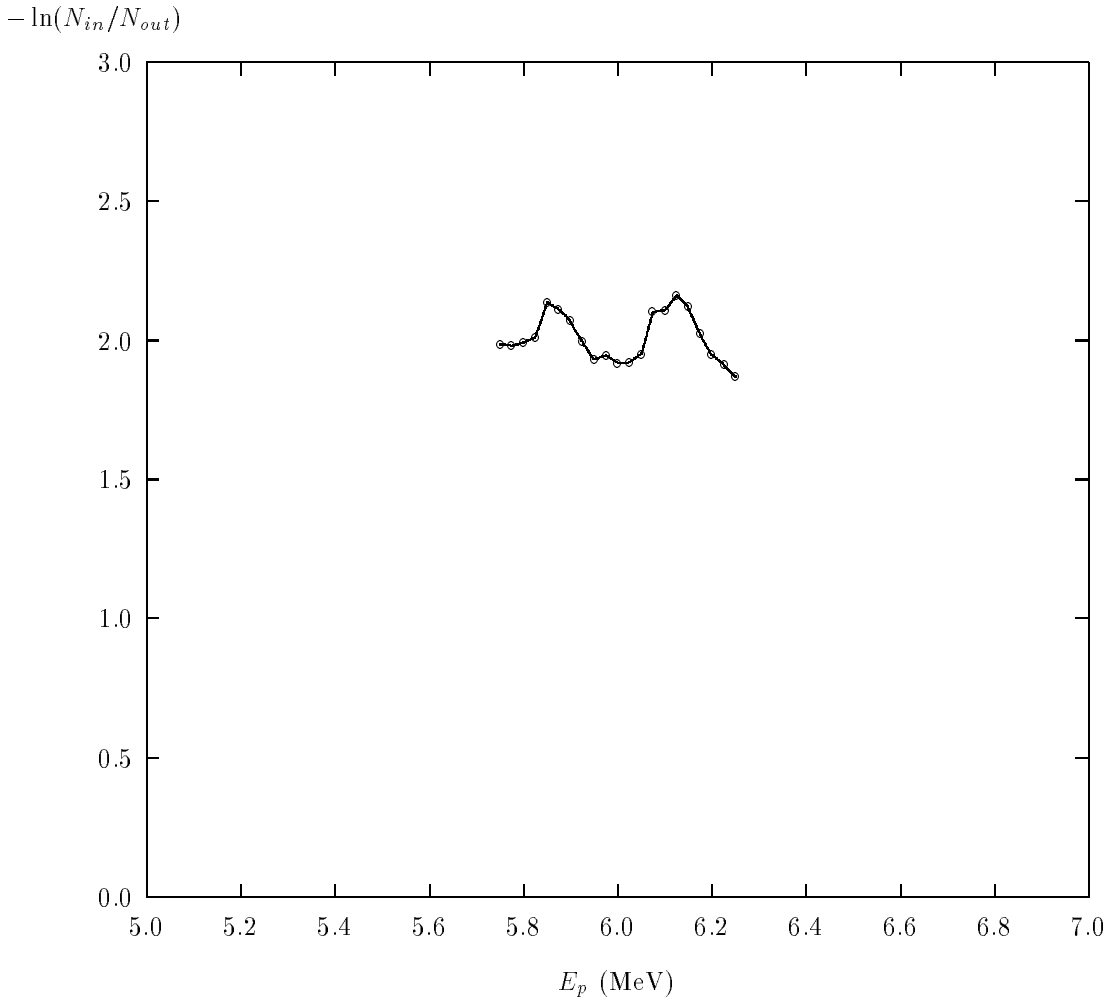

Figure 3.14: Measured Total Neutron Cross Section of Oxygen

E_p (MeV)	$\bar{E}_n$ (MeV)
3.02	1.94
4.66	3.65
5.41	4.42
5.89	4.91
6.18	5.21
6.77	5.81
7.21	6.25

Table 3.4: Measured Average Neutron Energies

E_n (MeV)	ρ
1.94	1.000
3.65	1.077
4.42	1.450
4.91	1.500
5.21	1.530
5.81	1.330
6.25	1.430

Table 3.5: Asymmetry Dilution Factor Due to the Unpolarized Neutron Background

the incoming proton energy and the outgoing neutron energy (Table 3.4).

Time-of-flight studies using an unpolarized beam have shown that although no neutrons are produced by the ^{58}Ni beam stop, background neutrons are produced by the slits, the havar foil, and titanium in the Ti $^3H_2$, as well as by ^{13}C deposited on the havar. No polarization has been observed of these neutrons in measurements using the polarized beam and the neutron polarimeter. The net effect of this background is to dilute the measured asymmetries by a factor ρ. Values of ρ as determined from the time-of-flight spectra are listed in Table 3.5. The values of ρ do not increase monotonically with energy as they depend upon the detector thresholds.

Since the neutron beam must pass through the field of the superconducting magnet, there is the possibility of spin precession. Fortunately, the neutron spins are

E_n (MeV)	P/P_0
1.94	0.978
3.65	0.984
4.42	0.986
4.91	0.987
5.21	0.988
5.81	0.989
6.25	0.989

Table 3.6: Calculated Neutron Depolarization Due to the Superconducting Magnet

parallel to the direction of the magnetic field and ideally are not effected. There are, however, regions where neutrons not exactly on the beam axis, due to the finite extent of the beam, experience small transverse field components. This effect is greatest as the beam passes between the two coils of the split-coil magnet. The precession caused by these fields acts in opposite directions for neutrons on either side of the beam axis so that the average spin direction is preserved and the net effect is to depolarize the beam by some amount. In order to calculate this effect the FORTRAN code NEUTRONS is used (Appendix A). This program performs a Monte Carlo simulation of the beam passing through the magnetic field. The trajectories chosen are a random sampling of those allowed by the collimator. The spin precession of each neutron is tracked and averages calculated over all trajectories. The results for 10,000 neutrons, tabulated in Table 3.6, are used in determining the neutron polarization during $\Delta\sigma_T$ measurements.

3.3.2 Neutron Beam Collimation

In order to obtain a large solid angle, the neutron source must be placed as close as possible to the polarized target as its size limits that of the beam. For this reason, the collimator is placed after the target instead of in front of it as in a shielded source arrangement. Having a completely unshielded neutron source would, however, illuminate the superconducting magnet and other parts of the cryostat, greatly increasing the background. To alleviate this problem, a small pre-collimator is used. In addition, the neutron detectors are placed within a large shield (Figure 3.15) to further

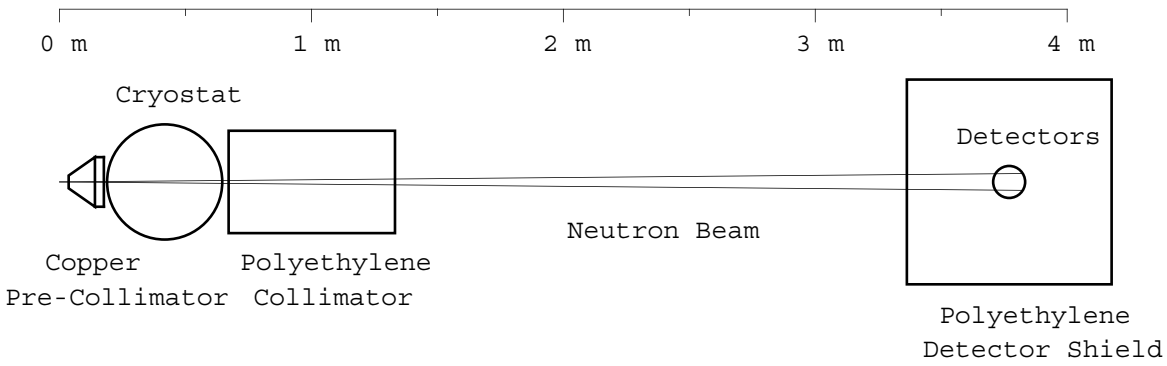

Figure 3.15: Neutron Collimation and Shielding

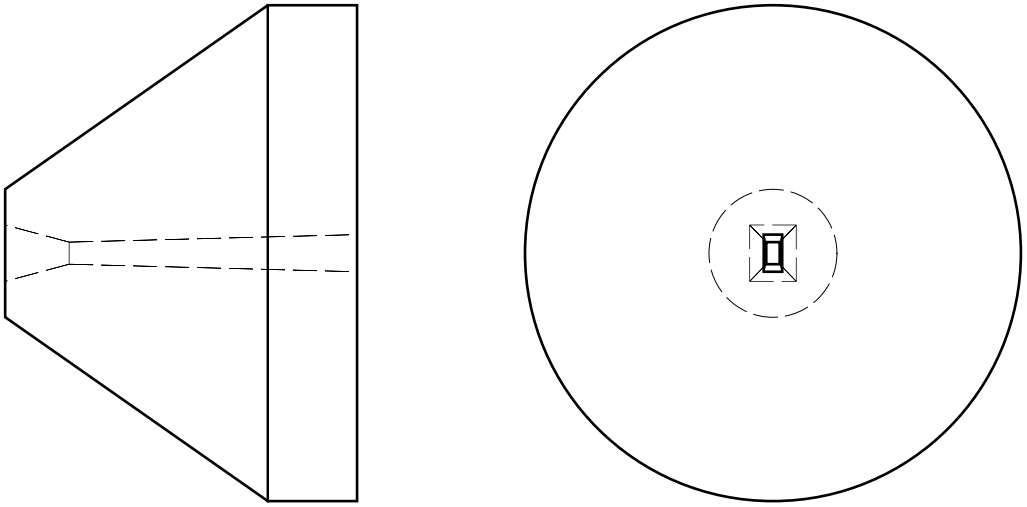

Figure 3.16: Neutron Pre-Collimator

suppress the background.

The pre-collimator, shown in Figure 3.16, is constructed of a copper cone with a rectangular double-truncated bore. The entrance opens at a total included angle of 30° in each plane, while the exit opens at an angle of 1.0° in the horizontal plane and 3.0° in the vertical plane. The size of the opening at the narrowest point is 5.33 mm × 8.76 mm. The total included angle of the copper cone is 70° and is 197 mm in diameter at its base. The thickness of the cone in the beam direction is 133 mm, giving a neutron attenuation factor of 44 at 10 MeV [Che87]. The pre-collimator is mounted on three stainless-steel rods 25.4 mm in diameter. Each rod

has a turnbuckle in the center and a dial indicator, allowing vertical adjustment to ± 25 μm. The rods are connected to a rotating stage which sits on an x-y translation table. This arrangement allows precise control of the axial, horizontal, and vertical position of the pre-collimator as well as the horizontal and vertical angles. The positioning mechanism is constructed such that the pre-collimator tilts and rotates about its narrowest opening. This defines a beam spot at the center of the polarized target having dimensions 9.35 mm $\times$ 25.65 mm with a solid angle of 0.53 msr.[7]

The collimator is a rectangular block of polyethylene with a tapered rectangular bore. It is 500 mm high, 400 mm wide, and 660 mm long. As in the case of the pre-collimator, the bore opens with a total included angle of 1.0° in the horizontal plane and 3.0° in the vertical plane. The opening at the entrance is 12.70 mm $\times$ 38.10 mm and at the exit is 24.23 mm $\times$ 72.69 mm. The collimator is mounted on precision linear bearings which ride on cylindrical rails. This allows the collimator to be rolled away from the cryostat, allowing access for maintenance. The frame supporting this mechanism is made of stainless-steel angle stock welded together. Non-magnetic materials are used whenever possible in order to minimize the force on the superconducting magnet. The collimator is designed to provide an attenuation factor of at least 400 for neutron energies up to 14 MeV. The entrance and exit of the collimator are used as reference points in aligning all other devices along the neutron beam path. The alignment of the collimator with the target has been verified with the target at 4 K using X-ray film. The film is exposed by bombarding a deuterium gas cell with 5 MeV deuterons. Gammas produced in the gas and in the tantalum beam stop are believed to be responsible for exposing the film. Two films are used, one between the cryostat and the collimator and one after the collimator with an exposure time of 30 minutes. Rare-earth radiators are placed in front of the film to improve the sensitivity.

The detector shield (Figure 3.17) is a rectangular block of polyethylene measuring 806 mm $\times$ 806 mm $\times$ 1016 mm. It has a straight rectangular bore, 57 mm $\times$ 190 mm. The two neutron detectors are inserted from the top and bottom into a cylindrical hole. They are attached to aluminum plates on the top and bottom of the shield and contained within an iron pipe to provide magnetic shielding. This arrangement allows

[7]Since the pre-collimator is not very thick at the narrowest point, the actual solid angle is closer to the value of 0.9 msr defined by the collimator.

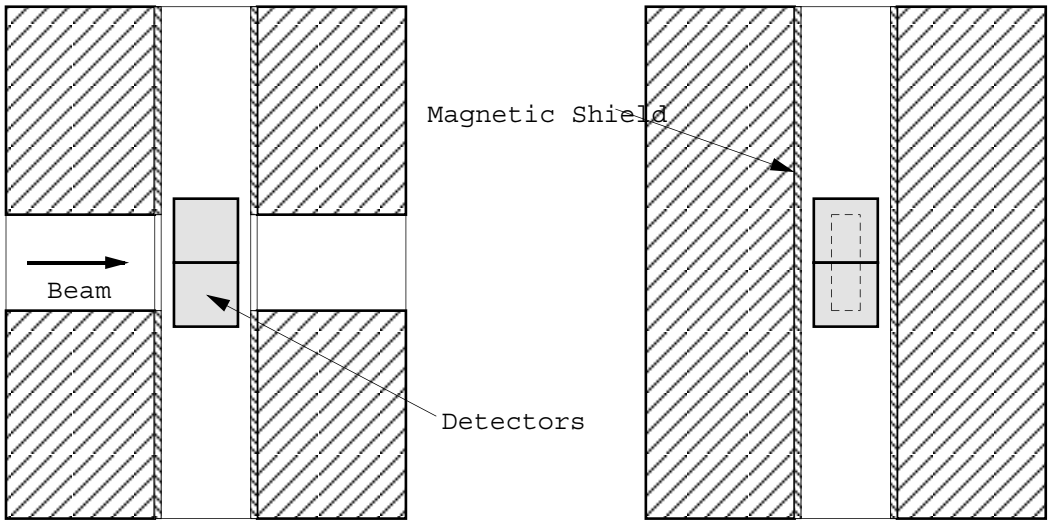

Figure 3.17: Neutron Detector Shield

the detectors to be easily removed for sighting through the collimation assembly. The shield is constructed of stacked 25.4 mm thick sheets of polyethylene with aluminum plates on the top and bottom and with vertical rods compressing the entire stack. The bore of the shield extends all the way through, allowing the neutron beam to exit without scattering back into the detectors. The iron pipe also has windows to reduce the attenuation of the beam. Additional shielding is placed around the beam entrance and around the detector access holes on the top and bottom.

3.3.3 Neutron Detection

In order to measure $\Delta\sigma_T$, the transmitted neutron flux at 0° must be detected. Unlike charged particles, neutrons are not detected directly, but through secondary reactions. Recoil protons from a hydrogen-rich target provide one such method, and in the case of organic liquid scintillators, the scintillation fluid is also the hydrogen target. The neutron detectors in this experiment consist of such scintillators attached to photomultiplier tubes which detect the flashes of light from the neutron events. These detectors are also sensitive to gammas, and a means of discriminating the two particles is necessary. Pulse-shape discrimination provides this information and is implemented using commercially available electronic modules. Two detectors are used to cover the entire solid angle of the neutron beam, using readily available equipment.

Organic liquid scintillators operate by detecting the recoil protons from ^{1}H(n,n)^{1}H reactions. The protons then interact with the scintillator, either by excitation or ionization, which emits light during de-excitation or recombination [Swa60]. This light strikes the photocathode of the photomultiplier tube, producing electrons. The number of electrons is increased through secondary emission by the dynodes of the electron multiplier. The final electron current is collected by the anode. As the light has different decay times for neutrons and gammas, the current appears as a pulse with different rise and fall times. This property is exploited by the pulse-shape discrimination electronics.

The scintillator cells are aluminum cylinders 127 mm in diameter and 127 mm in length with one face made of glass to allow the light to exit. The insides of the cells are coated with a white reflector paint to reduce light loss. The scintillator fluid is Bicron BC-501 and an expansion tube is provided to accommodate thermal expansion of the liquid without bubbles. The photomultiplier tubes are Hamamatsu type R1250, which have 127 mm diameter photocathodes. As photomultiplier tubes are greatly affected by magnetic fields, shields made of a high permeability material are placed around them. The scintillator-photomultiplier assembly (Figure 3.18) is mounted to a flange which bolts to the detector shield.

The electronics for the neutron detectors, shown in Figure 3.19, take the anode signals and produce a NIM level output pulse for each neutron detected. Signals used for determining dead-time corrections are also produced. The Link 5020 modules perform the functions of amplification, pulse-shape discrimination, and single-channel energy analysis [Ada78, Lin]. This module distinguishes between neutrons and gammas by measuring the signal decay-times. The neutron output of the Link 5020 is converted to a fast NIM signal using a LeCroy 222 gate and delay generator before being sent to the data acquisition electronics. A second LeCroy 222 is configured as a 100 kHz pulser. Its output is ANDed with the live-time signal from the Link 5020. This signal and the ungated pulser signal are sent to the data acquisition system for calculating a dead-time correction, δ.

$$\delta = \frac{N_{pulser}}{N_{gated}} \tag{3.10}$$

Although this calculation only takes into account the 400 ns per event dead-time of the Link 5020, this is a valid assumption since the dead-time of the detector is approximately 25 ns per event.

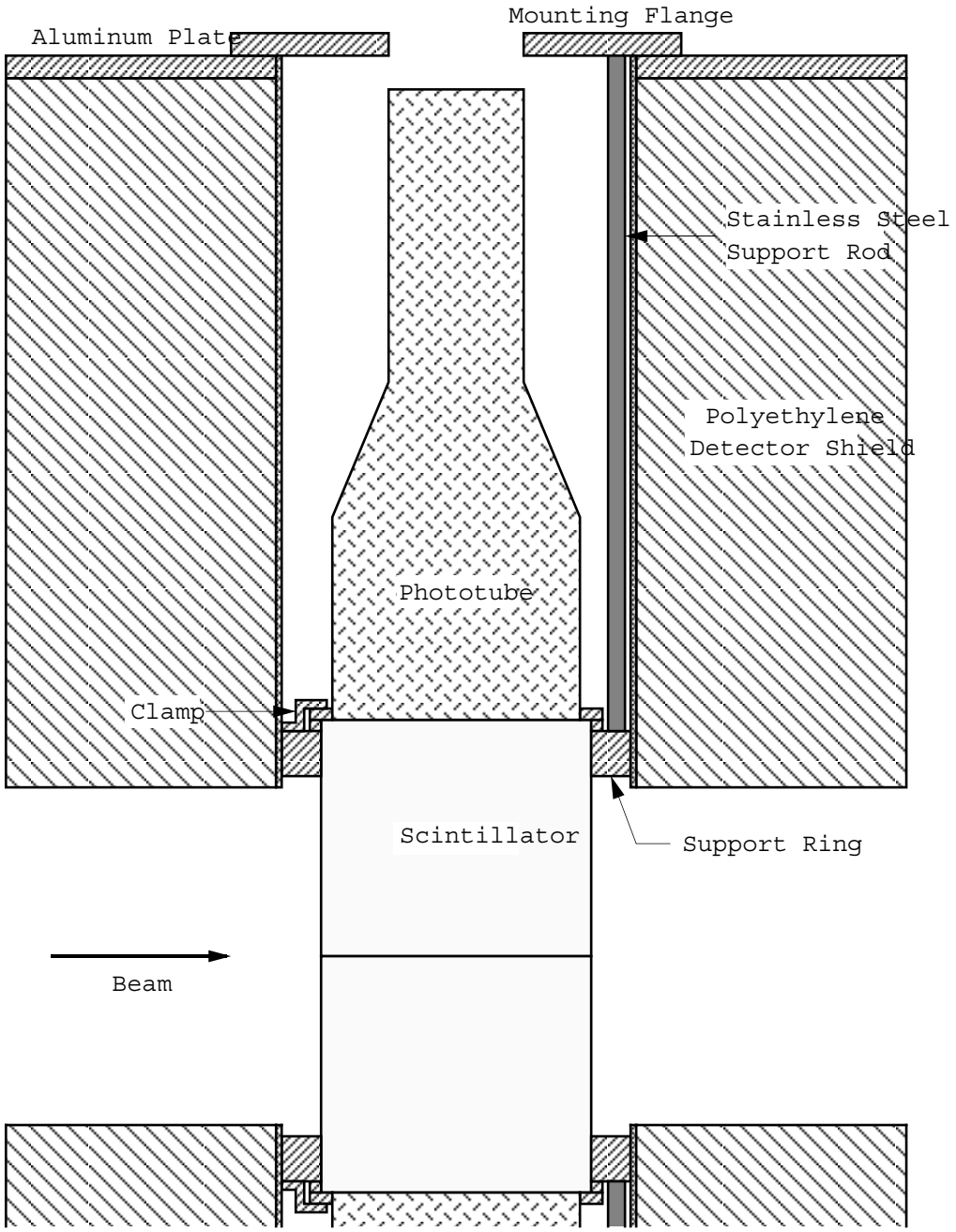

Figure 3.18: Neutron Detector Assembly

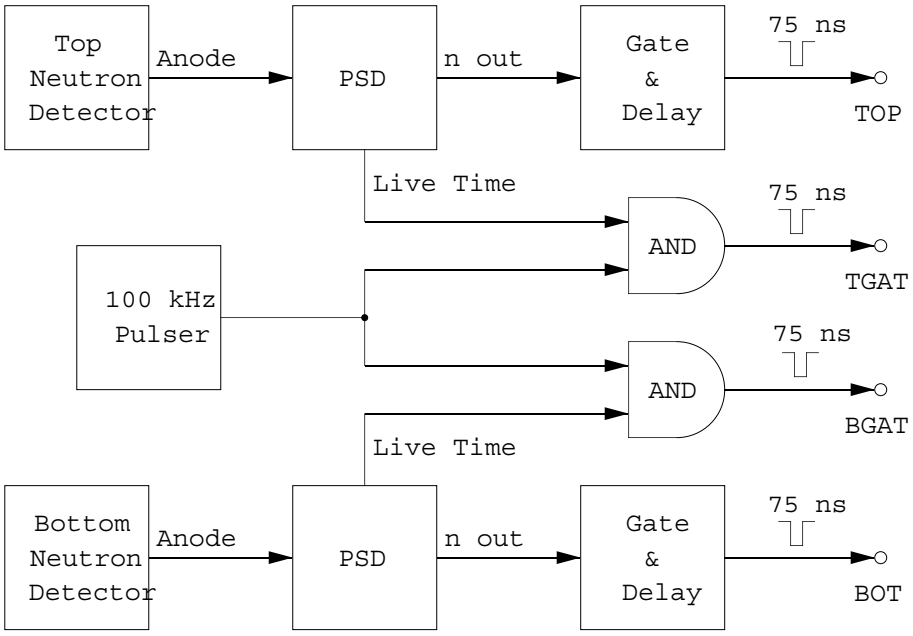

Figure 3.19: Neutron Detector Electronics

3.4 Neutron Polarimeter

Although the polarization of the neutron beam is usually determined by measuring the polarization of the charged-particle beam, it is important to be able to measure the neutron polarization directly. A neutron polarimeter provides a means of calibrating such secondary polarimeters and measuring polarization transfer coefficients. The polarimeter consists of a ^{4}He target and neutron detector pairs placed symmetrically about the beam direction (Figure 3.20). Since the analyzing power of neutrons scattering elastically from helium can be calculated with an accuracy of approximately ± 0.01, the neutron beam polarization can be extracted from the measured left-right asymmetry. The polarimeter is placed between the neutron collimator and the detector shield when in use and is oriented to measure polarization in the $\hat{x}$ direction (horizontal plane). The distance from the neutron source to the center of the polarimeter target is 1.79 m.

The target consists of helium gas at a pressure of 100 bar in a steel cylinder with 1 mm walls [Tor74]. The active volume of the cell has a diameter of 44.6 mm and a height of 158.2 mm. The gas has approximately 5% xenon added in order

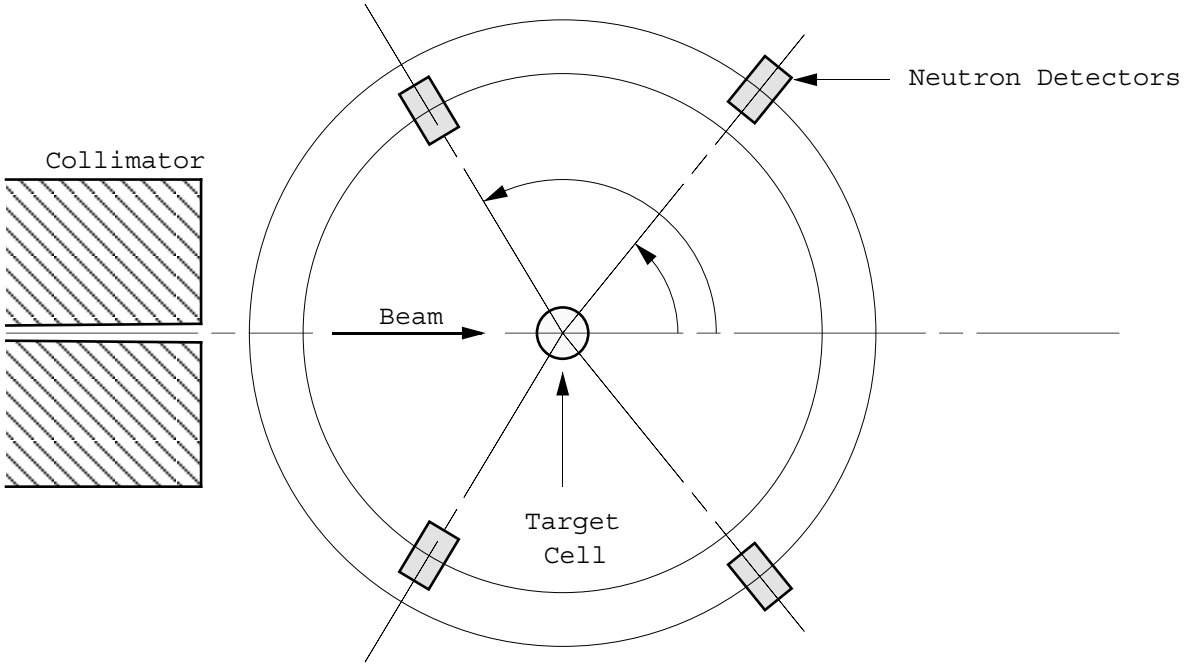

Figure 3.20: Neutron Polarimeter

to make it scintillate with the recoiling alpha particles. This arrangement makes it an active target and allows the measurement of timing coincidences and alpha energy, reducing the background from the neutron detectors. The gas cell, shown in Figure 3.21, has windows at both ends to allow the light from scintillations to be detected in photomultiplier tubes. The inside of the gas cell is coated with 0.8 mm of magnesium oxide as a reflector. Evaporated on top of the reflector is 120 μg/cm^2 of p-quaterphenyl which acts as a wavelength shifter, improving the response of the photomultiplier tubes. The photomultiplier tubes are Hamamatsu type H1161 having a diameter of 51 mm. The cell is filled using the system shown in Figure 3.22. The xenon is loaded first by liquefying the gas in the condensation chamber and then allowing it to evaporate and expand into the target cell until a pressure of approximately 5 bar is attained. This method is necessary as the xenon is stored at too low of a pressure to fill the cell directly. Then, 99.999% helium is bled into the cell in stages until the final pressure of 100 bar is reached. The gas filling system is constructed completely of stainless-steel with viton o-rings used as valve stem seals and is designed to withstand pressures of 330 bar. A sintered stainless-steel filter

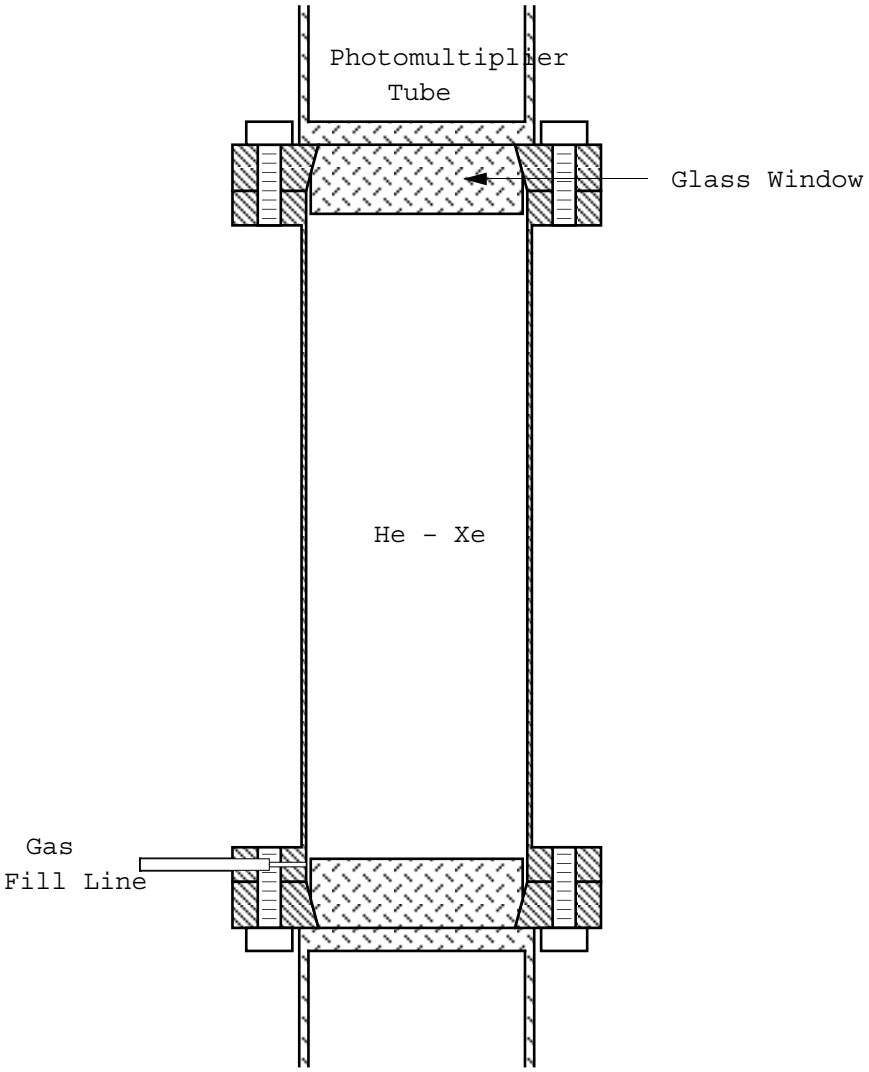

Figure 3.21: High-Pressure Helium Gas Cell

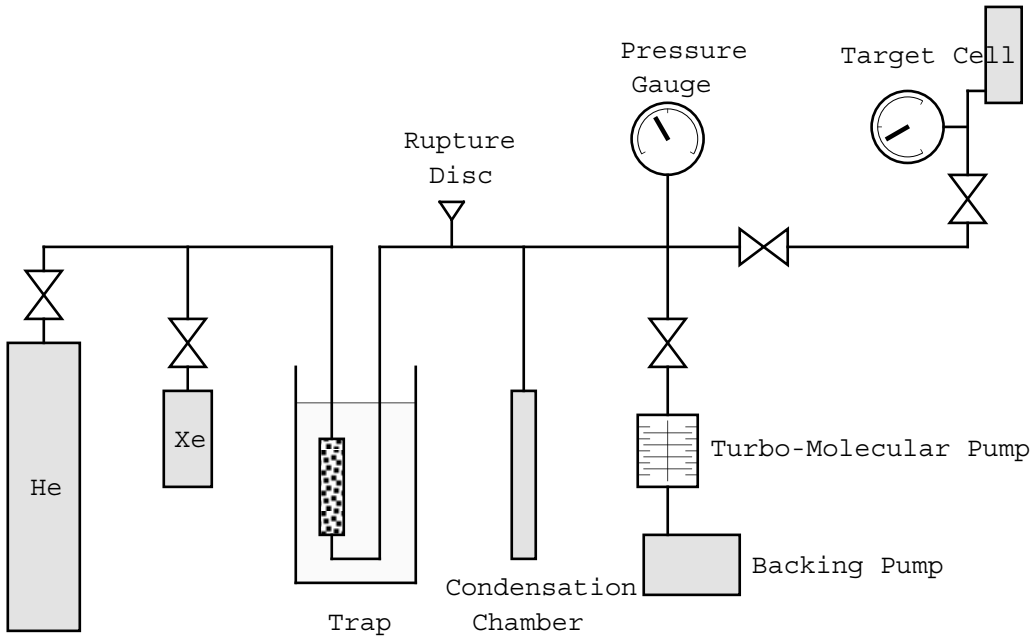

Figure 3.22: Helium Cell Filling System

cooled to liquid nitrogen temperatures is used to trap contaminants during the helium fill. The filter must be warmed above the melting point of xenon when filling with this gas. As small amounts of contaminants, such as nitrogen and oxygen, greatly reduce the performance of the cell by absorbing the light of scintillation, the cell and gas filling system are pumped by a turbo-molecular pump before use.

The neutron detectors are placed symmetrically about 0° at angles where the product of the square of the analyzing power and the cross section is a maximum for ^{4}He(n,n)^{4}He. There are two such angle pairs, one forward and one backward, and two detector pairs are used. At the lowest energy measured, however, one maximum is too low in magnitude to be useful and only one detector pair is used. The detectors are organic liquid scintillators coupled to photomultiplier tubes through light guides. The light guides match the geometry of the 45 mm $\times$ 158 mm $\times$ 76 mm thick rectangular scintillator cells to the 51 mm diameter phototubes. The photomultiplier tubes are Hamamatsu type H1161. The neutron detectors are mounted to a detector ring having 1° graduations. The entire apparatus has been aligned optically with the neutron beam collimator. The forward detector pair uses an electronic setup (Figure 3.23) similar to that used for the main neutron detectors (Section 3.3.3). Since there are

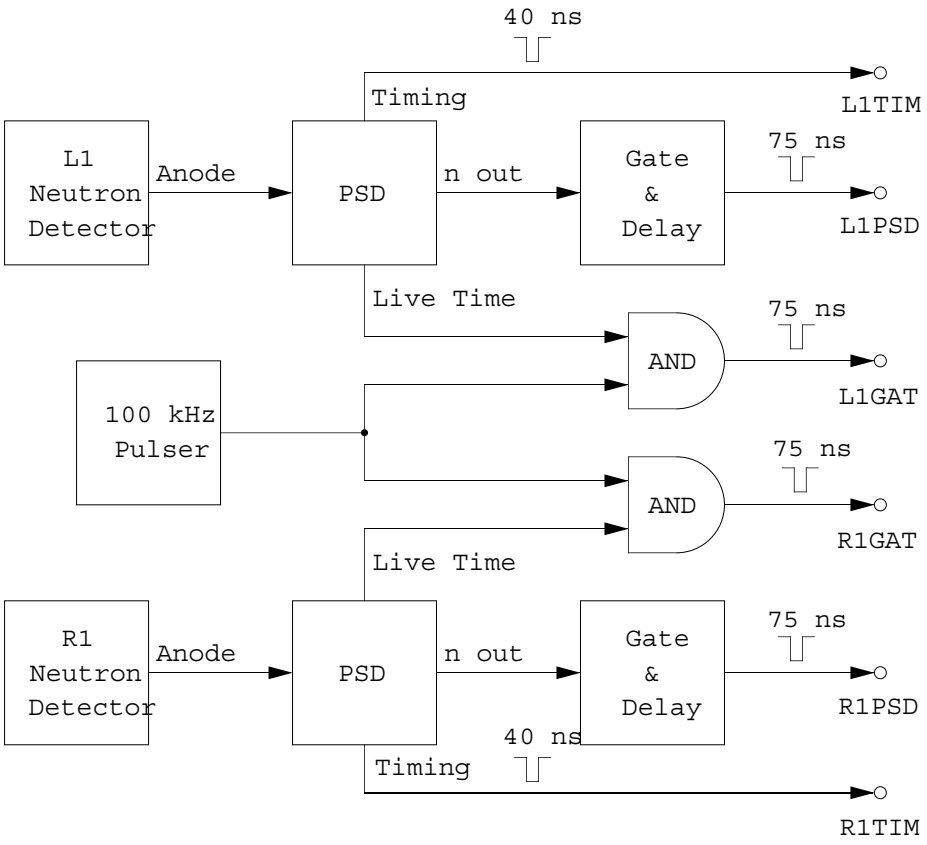

Figure 3.23: Electronics for the Forward Neutron Detector Pair

not enough Link 5020 PSD modules for all four detectors, a different setup must be used for the backward angle pair (Figure 3.24). In this setup, a Canberra 2160A PSD module is used to determine the zero-crossing of the anode signal after the peak of the pulse [Can83]. By measuring the time between the start of the pulse, determined by a constant-fraction discriminator (CFD), and this zero-crossing, neutrons can be distinguished from gammas.

Monte Carlo techniques have been used to calculate the effective analyzing power of the neutron polarimeter [Tor75]. These calculations make corrections for the finite geometry of the target cell and neutron detectors, and for double-scattering events. Double scattering which includes neutrons scattering from materials in the target cell other than helium must be considered. The double-scattering events which are considered are He-He, He-Xe, Xe-He, He-Fe, and Fe-He. Since only events which

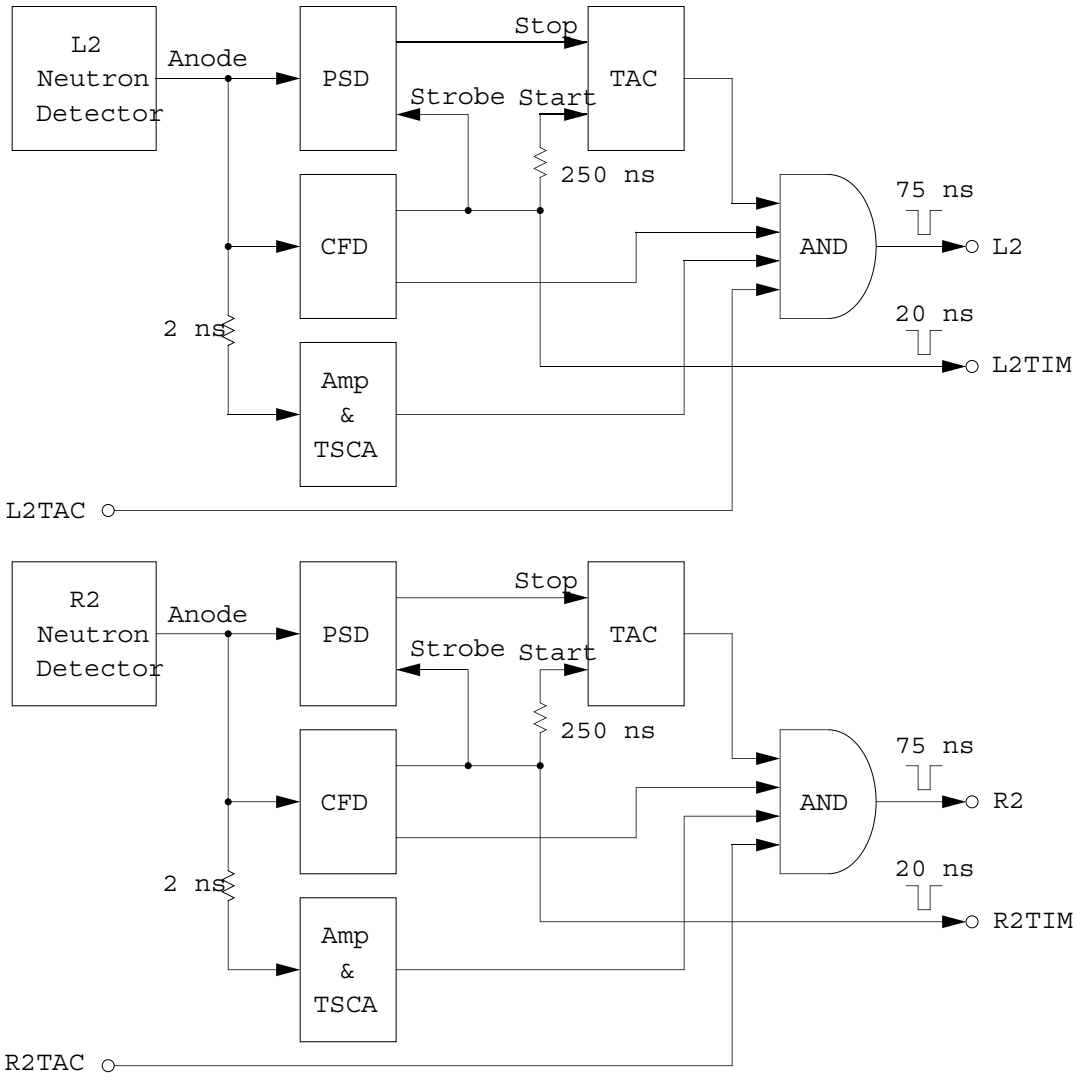

Figure 3.24: Electronics for the Backward Neutron Detector Pair

E_n (MeV)	θ	d (mm)	A_y
1.94	107°	408	0.764 ± 0.010
5.21	50°	408	-0.629 ± 0.010
	121°	338	0.919 ± 0.015
5.81	51°	408	-0.632 ± 0.010
	121°	308	0.916 ± 0.015

Table 3.7: Effective Analyzing Powers for the Neutron Polarimeter

include the detection of an alpha are recorded, single scattering events from elements other than helium need not be considered. Cross sections and analyzing powers are obtained from phase-shift data sets. The phase shifts for helium come from experimental data [Sta72] as do the phase shifts for xenon and iron at the higher energies. At the lowest energy measured, 1.94 MeV, experimental cross section data for xenon are used with analyzing powers assumed to be zero. The calculated effective analyzing powers, A_y, are shown in Table 3.7 for the neutron energies at which measurements have been made. The length of the flight paths, d, from the center of the target cell to the center of the detector is also given.

For an event to be considered valid, three criteria must be satisfied. First, there must be a coincidence between the top and bottom photomultiplier tubes of the target cell, reducing the noise from the tubes. Second, the signal from the neutron detector must meet pulse-shape discrimination requirements, eliminating signals from gammas. Third, there must be a coincidence between the target cell signal and one of the neutron detector signals, in order to reject neutron background events. Figure 3.25 shows the electronic setup which performs these functions. The anode signals from the target cell photomultiplier tubes are used to form the coincidences, while the dynode signals provide the alpha recoil energy information. Summing the dynode signals improves the energy resolution of the detector as only part of the light of scintillation is deposited in each photomultiplier tube. The gains of the two tubes are matched using a ^{137}Cs source. Since the alpha recoil energy is quite different for the forward and backward angles, the summed dynode signal is split into two signals which are amplified and delayed by different amounts before being recombined. This process creates two pulses for each alpha, one large in amplitude and one small. The large

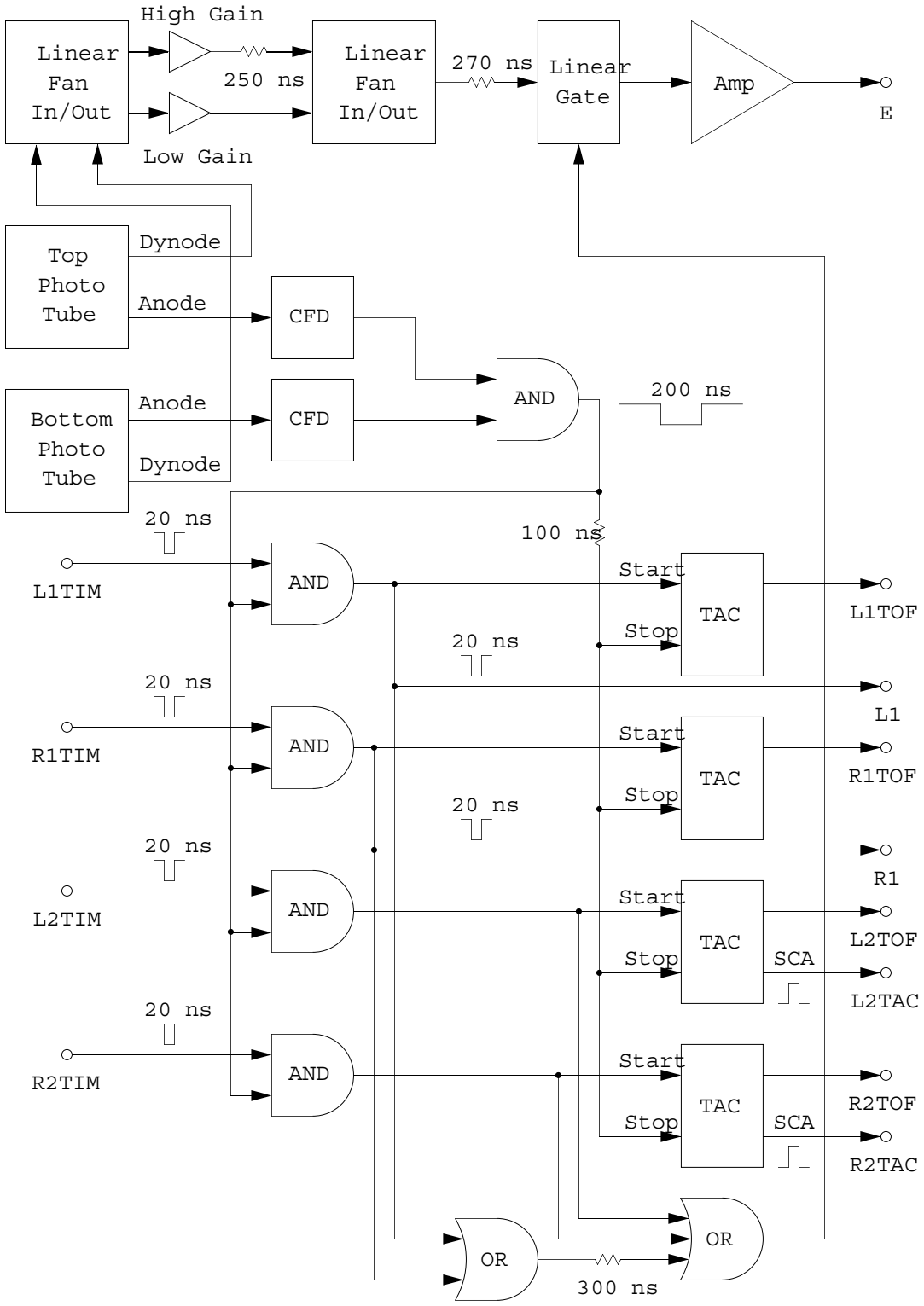

Figure 3.25: Coincidence Electronics for the Neutron Polarimeter

amplitude pulse is gated through to the data acquisition system only when an event occurs in one of the backward angle detectors. Conversely, the small amplitude pulse is gated through only when an event occurs in one of the forward angle detectors. This arrangement allows a single ADC to digitize the alpha recoil energy for both detector pairs. Neutron time-of-flight from the target cell to the neutron detectors is determined using Ortec 467 time-to-amplitude converters (TAC). The start signal for each TAC comes from the timing signal of the corresponding neutron detector after the coincidence with the target cell anode coincidence signal. The coincidences are formed such that the timing signal from the neutron detector determines the timing of the TAC start signal. The stop signal comes from a delayed version of the target cell anode signal. This delay is adjusted to give a suitable range for the neutron time-of-flight signals (typically 100–200 ns). Because of the coincidence requirements, the count rates are low, typically a few per second.

3.5 Polarized Proton Target

The polarized proton target uses the brute-force technique [SP86] of cooling the target material to low temperatures in a large magnetic field. This method has the advantage of producing very thick targets with fewer polarized impurities than other methods such as laser pumping. The brute-force method makes use of the energy difference between the different nuclear magnetic substates. The population p_m of a substate with spin projection m measured in the direction of the magnetic field B is given by

$$p_m = \frac{e^{mgB/kT}}{\sum_{m=-I}^{m=+I} e^{mgB/kT}} \tag{3.11}$$

where g is the nuclear g-factor and k is the Boltzmann constant. For protons, $I = 1/2$ and the target polarization P_T is given by

$$P_T = \frac{p_{+1/2} - p_{-1/2}}{p_{+1/2} + p_{-1/2}}. \tag{3.12}$$

For a given temperature T and magnetic field B, the polarization is then

$$P_T = \tanh\left(\frac{gB}{kT}\right). \tag{3.13}$$

The magnetic field is produced using a 7 T superconducting magnet.[8] The magnet is a split-coil solenoid with Nb-Ti windings. The magnetic field in the sample region is uniform, having a homogeneity of 0.1% over 1 cm. The magnet is charged to its rated current of 86.2 A and placed in persistent mode, causing the field to be essentially constant over the course of the measurement. The inductance of the magnet is approximately 30 H, storing over 100 kJ of energy at full field. For protons in a 7 T field, the polarization is given by

$$P_T = \tanh(T_0/T) \tag{3.14}$$

with T_0 =7.15 mK. The sample must then be cooled to a temperature of order T_0 to produce significant polarization. A ^{3}He-^{4}He dilution refrigerator is used to achieve these temperatures.

3.5.1 Dilution Refrigerator

Since measurements of $\Delta\sigma_T$ require that the proton target remain polarized for several days at a time, a means of continuous cooling at temperatures of 10–20 mK is required. The only continuous method for cooling below 300 mK is the ^{3}He-^{4}He dilution refrigerator [Lou74]. The principle of operation of the dilution refrigerator [Lon51, Lon62] relies on a phase separation which occurs in ^{3}He-^{4}He mixtures at temperatures below several hundred millikelvin. One phase (dilute phase) is a mixture of approximately 6% ^{3}He and 94% ^{4}He, while the other (concentrated phase) is essentially pure ^{3}He. Below 500 mK, the ^{4}He, obeying Bose-Einstein quantum statistics because of its 0 spin, is superfluid in its ground state and has no entropy. The ^{3}He, however, is spin 1/2 and obeys Fermi-Dirac statistics. Thus it has a non-zero heat capacity and entropy even as the temperature approaches absolute zero. A diffusion of ^{3}He from the concentrated phase to the dilute phase is analogous to evaporation and produces cooling. A dilution refrigerator (Figure 3.26) maintains an osmotic pressure gradient across the phase boundary by continuously pumping ^{3}He from the dilute phase and restoring it to the concentrated phase. The phase separation occurs in the mixing chamber. ^{3}He which is to be returned to the mixing chamber is first condensed by the cold plate and is then cooled as much as possible by heat exchangers

[8] American Magnetics, Incorporated, Oak Ridge, Tennessee.

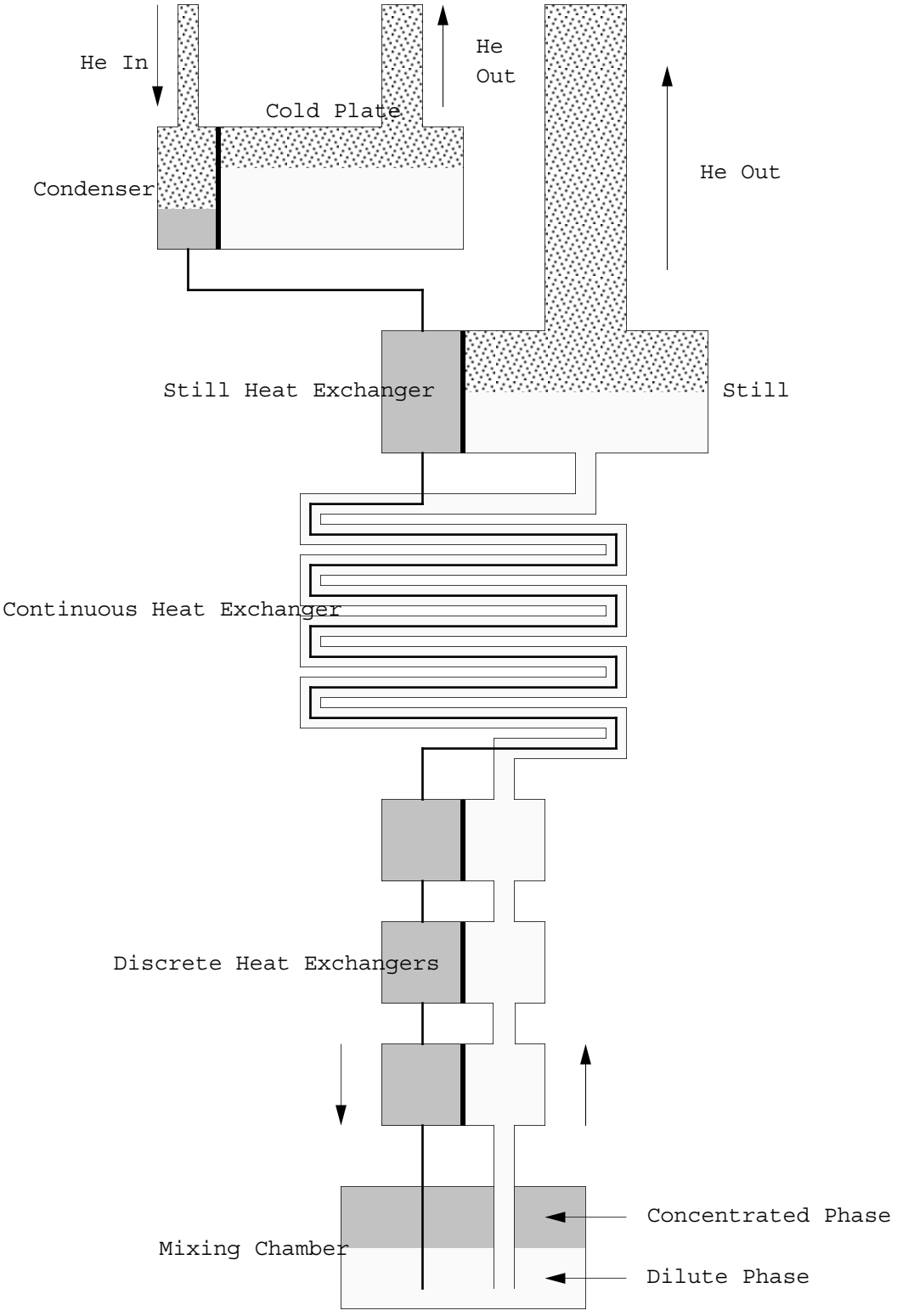

Figure 3.26: Dilution Refrigerator

in thermal contact with the dilute phase. ^{3}He is removed from the dilute phase in the still. A heater in the still increases the recirculation rate by raising the vapor pressure of the ^{3}He. The ^{4}He, having a much lower vapor pressure remains behind. The cold plate is cooled to approximately 1 K by pumping on liquid ^{4}He obtained from the surrounding liquid helium bath. In principle, the ultimate temperature of a dilution refrigerator is limited only by the efficiency of the heat exchangers and temperatures of a few millikelvin have been reached by this method.

The dilution refrigerator used in this experiment is an S. H. E. Model 430. The refrigerator has an ultimate temperature of 4.5 mK and a cooling power of 1.5 μW at 10 mK. The ^{3}He is recirculated at a rate of 500 μmol/s by an Edwards 9B3 diffusion pump backed by a hermetically sealed mechanical pump. A copper cold finger is connected to the mixing chamber for attaching the target. The dilution refrigerator and the superconducting magnet are contained within a liquid helium cryostat (Figure 3.27). The cryostat holds the liquid helium necessary for operating the refrigerator and cooling the magnet, and provides thermal insulation. The cryostat requires 100 liters of liquid helium for the initial cooldown, and approximately 30 liters each day thereafter. Hollow brass cylinders are inserted in the magnet bore as spacers to remove most of the liquid helium from the neutron beam, reducing the attenuation of the beam.

3.5.2 Titanium Hydride Target

The criteria for choosing a suitable material for use as a polarized proton target are very stringent. The hydrogen in the material must be polarizable by a magnetic field and it must have a large heat conductivity at millikelvin temperatures. All other nuclei contained in the material must not be polarized by the magnetic field. Molecular hydrogen, H_2, is not suitable since the two nuclei in the molecule pair off with opposite spins in the para-hydrogen configuration. The heat capacity associated with converting the para-hydrogen to ortho-hydrogen is too large to be overcome in practice. Most hydrocarbons can be ruled out because of their low heat conductivities and because of the presence of ^{13}C, which becomes polarized. Many other hydrogen compounds do not have a sufficiently high hydrogen content or have unwanted contaminants. One material which is suitable for use as a polarized proton target is

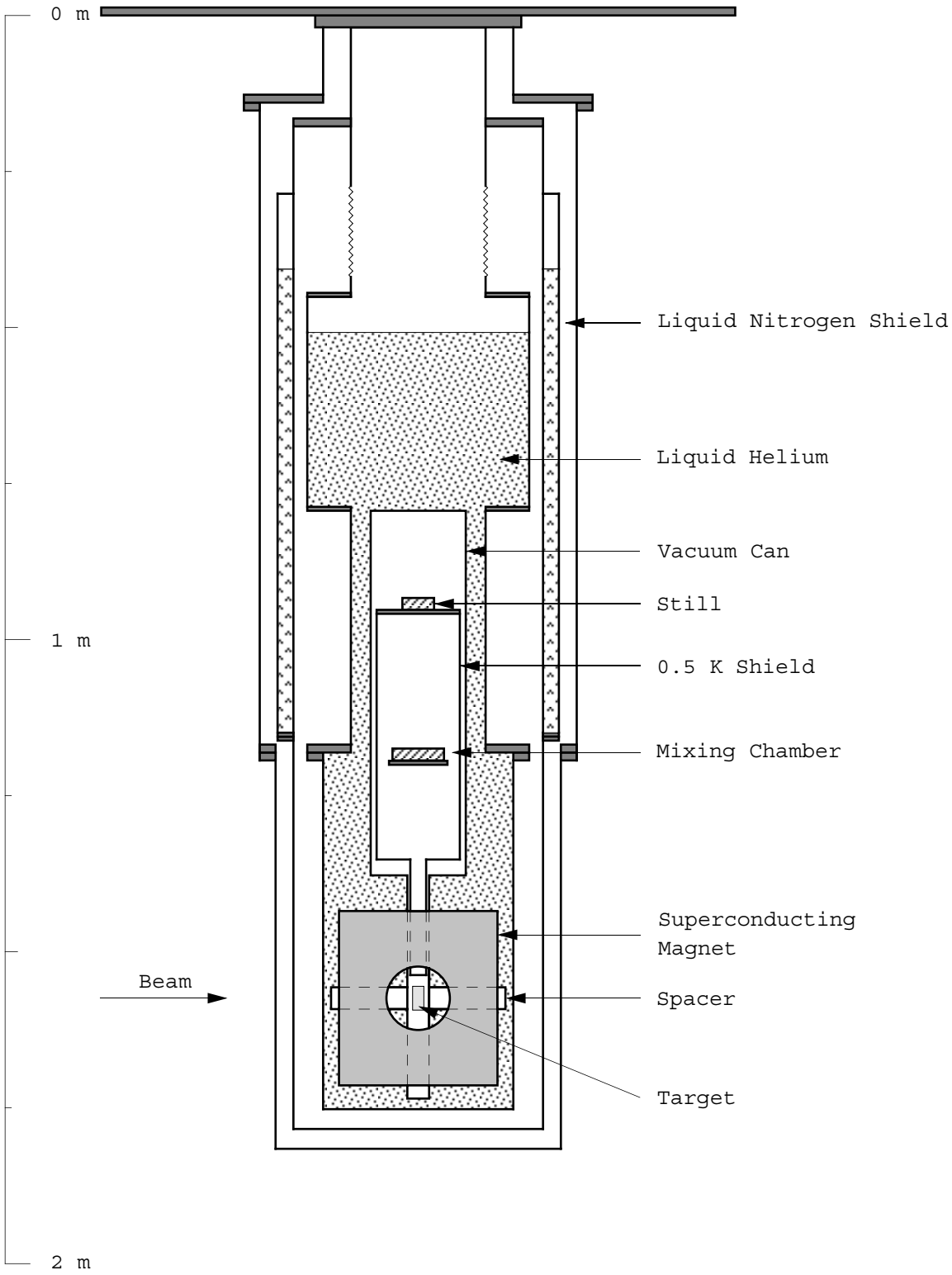

Figure 3.27: Dilution Refrigerator Cryostat

titanium hydride, TiH_2, as demonstrated by Aures et al. [Aur84].

Titanium hydride is made by heating very pure titanium in a hydrogen atmosphere. The TiH_2 is then in the form of a powder which must be compressed to form a solid sample. The proton density of such a target is 9.0×10^{22} cm^{-3} as compared to 5.3×10^{22} cm^{-1} for solid H_2. It has been shown that heat conductivities of approximately 5×10^{-5} W/cm·K at temperatures of 10–20 mK can be attained with this type of sample [Hee85]. This value is an order of magnitude below that of pure titanium [Chi76]. Recent work indicates that the conductivity depends greatly on the purity of the material [Li92]. The first attempts to produce a target for this experiment used commercially available TiH_2 with a purity of 99%. The powder was pressed into a silver box under a pressure of 0.4 GPa. Silver is chosen because of its excellent heat conductivity and because it does not become polarized. The polarization was determined to be only 15% by measuring the asymmetry in the neutron transmission (Section 4.1). This value corresponds to a temperature of approximately 50 mK.

Since polarizing a sample and measuring its polarization is an expensive and time consuming process, a simpler method of determining the quality of the TiH_2 target is needed. The Wiedemann-Franz law

$$\kappa = \mathcal{L} T \sigma \tag{3.15}$$

states that below 1 K the thermal conductivity, κ, of a metal is proportional to its electrical conductivity, σ, where $\mathcal{L} = 25$ nW·Ω/K^2 is the Lorentz constant and T is the temperature. Because of this relation, a measurement of the electrical conductivity as a function of temperature gives an indication of the thermal properties of the material. Electrical resistance measurements of the first TUNL TiH_2 target at 300 K and at 80 K indicate that the resistance decreases as a function of increasing temperature. This behavior indicates the material is behaving as an electrical insulator and suggests that its thermal conductivity will be low as well. Similar measurements for the target used by Aures et al at KFA Karlsruhe, Germany [Hee85] indicate that their sample behaves electrically as a metal, implying a relatively high heat conductivity. The difference is thought to be due to impurities in the commercial TiH_2.

The final TiH_2 target is made from the same material as the Karlsruhe target.[9] The powder is pressed into a rectangular copper box with the front and back faces

[9] We gratefully acknowledge the assistance of H. O. Klages at KFA Karlsruhe, Germany in providing the material for this target.

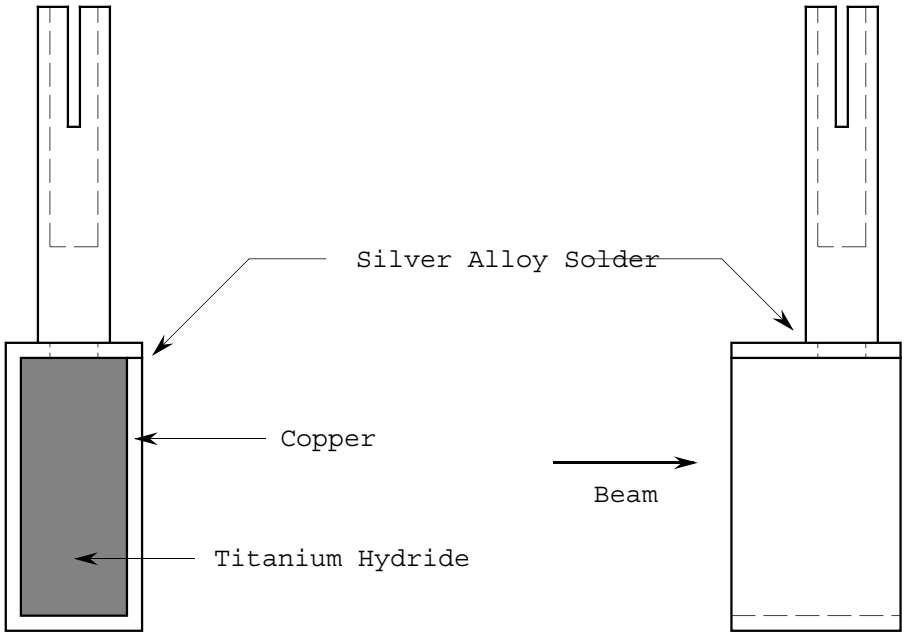

Figure 3.28: Titanium Hydride Target

open, since the copper becomes polarized. Copper is chosen to more closely approximate the Karlsruhe design. The box, made from 2 mm copper plate, is placed within a hardened steel die. The powder is pressed into the box under a pressure of 1.5 GPa. A 0.5 mm silver foil was placed at the bottom of the die to allow the connection of thermometers to the TiH_2, but good thermal contact was not established. As a result, the target polarization must be determined by nuclear measurements (Section 4.1). The rear face, which suffered from mechanical defects, has been machined to give a smooth surface. A bored copper rod is soldered to the top of the box for attachment to the dilution refrigerator cold finger. The TiH_2 target (Figure 3.28) has a density of 3.75 g/cm^3 and a thickness of 22.4 mm giving a proton thickness of 0.203 b^{-1}. The area of the TiH_2 face is 14.0 mm $\times$ 34.1 mm. The total amount of hydrogen contained in the target is 1.6 mol. Electrical resistivity measurements indicate a metallic behavior similar to the Karlsruhe target. Proton polarizations obtained from this target are in the range 40–50%, corresponding to temperatures of 13–17 mK.

3.5.3 Thermometry

Although attempts to accurately measure the temperature of the TiH_2 directly have been unsuccessful, it is still important to monitor various temperatures inside the cryostat as an indication of how well the dilution refrigerator is working. The simplest thermometers are resistors whose resistance changes with temperature. Approximately twelve carbon or thick film resistors are attached to various parts of the refrigerator, including the cold finger, mixing chamber, still, and the discrete heat exchangers. In addition, two calibrated germanium resistors are used, one attached to the cold finger, and one to the mixing chamber. The resistance measurements are made using an AC four-lead resistance bridge. Although the resistance thermometers are the easiest to use, they are not useful below approximately 50 mK as the resistance saturates.

In the temperature range 5–40 mK, nuclear orientation thermometry may be used. ^{54}Mn and ^{60}Co are the most common isotopes used for this purpose [Mar83]. A cobalt nuclear orientation thermometer consists of a small amount of ^{60}Co embedded in a single crystal of natural cobalt. Below about 100 mK, the cobalt nuclei become aligned along the crystal direction, due to the large effective magnetic field (several tesla) of the ferromagnetic material. The ^{60}Co decays with a half-life of 5.3 years, emitting gammas with energies of 1333 keV and 1173 keV. For an unpolarized crystal, the radiation is emitted isotropically. As the crystal becomes more polarized, the radiation becomes anisotropic with a minimum flux along the crystal axis. Such a crystal is mounted inside the cryostat in thermal contact with the cold finger. The cobalt is located outside of the bore of the superconducting magnet to minimize the effect of the magnetic field on its polarization. An intrinsic germanium gamma detector is placed outside of the cryostat along the crystal axis. The gamma count rate is measured and compared to the rate at temperatures above 40 mK to determine the temperature. Measurements to an accuracy of 1 mK can be obtained by counting for approximately 300 s. Since the presence of a neutron beam makes accurate measurements impossible, this method is not always practical. In addition, since warm counts are required, the germanium detector cannot be moved once the refrigerator is cold.

A third type of thermometer which is used to measure the temperature of the dilution refrigerator is the ^{3}He melting curve thermometer (MCT) [Kei90, Kei92].

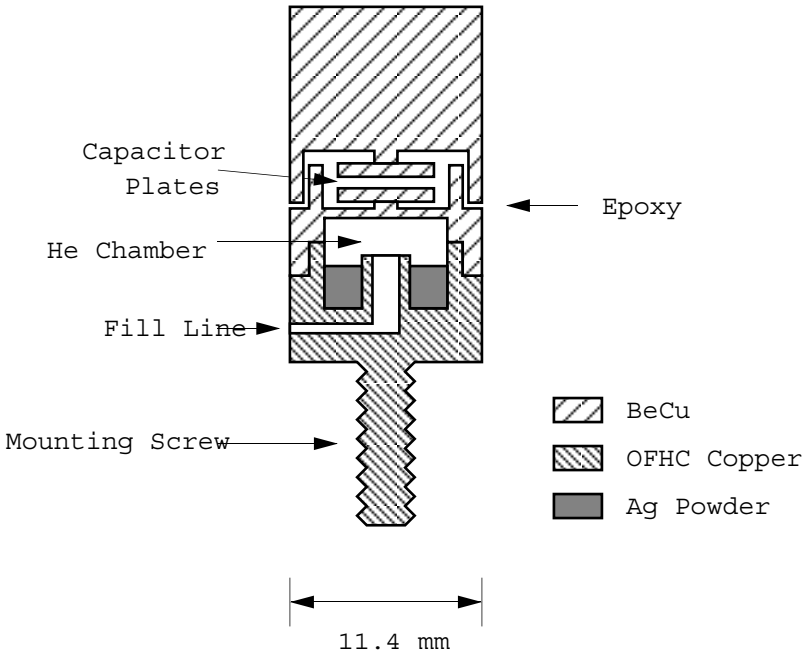

Figure 3.29: ^{3}He Melting Curve Thermometer

The MCT relies on the precise knowledge of the pressure versus temperature of ^{3}He along the melting curve at low temperatures [Gre86]. The MCT contains a mixture of solid and liquid ^{3}He in what is essentially a constant volume (Figure 3.29). The cell is filled at 1 K through a capillary tube leading to a room temperature gas handling system. As the temperature decreases, a plug of solid ^{3}He forms in the tube, sealing the cell at a constant average density. The top of the ^{3}He chamber is a 250 μm thick diaphragm to which one plate of a capacitor is attached. Changes in pressure are observed as changes in the capacitance, which can be measured to an accuracy of 1×10^{-5} pF out of a total capacitance on the order of 10 pF. This corresponds to a temperature sensitivity of approximately 1.5 μK at 10 mK. By calibrating the capacitance versus pressure characteristics of the cell at 1 K with a precision Bourdon tube gauge, the absolute accuracy of the temperature measurement is estimated to be 0.36 mK. Two such devices are installed in the cryostat, one attached to a silver foil which touches the TiH_2 target and one attached to the cold finger.

3.6 Data Acquisition Electronics

Data from the measurements are collected by CAMAC modules controlled by a MBD-11 Multiple Branch Driver [Rob81]. The MBD is connected to a Digital Electronics Corporation VAXStation 3200 which supervises the data acquisition, stores the data, and performs online analysis. In addition, this computer performs part of the feedback steering of the proton beam. The data acquisition software runs under the TUNL XSYS data acquisition and analysis system [Gou81].

3.6.1 $\Delta\sigma_T$ Measurements

For the $\Delta\sigma_T$ measurements it is necessary to measure count-rate asymmetries to an accuracy of order 1×10^{-4}. Instrumental asymmetries due to the data acquisition system must therefore be of order 1×10^{-5} or less. To achieve this level of stability, several methods are employed. First, the spin of the neutron beam is rapidly reversed at a rate of 10 Hz to reduce the effects of detector gain drifts and other instrumental shifts. Precision timing is used to insure that the same amount of time is spent counting in each spin state. Finally, the data are collected and stored in 800 ms time slices, allowing asymmetries to be calculated for very short periods of time before being averaged together. All the data are collected by counting pulses in scalers since all particle discrimination takes place in hardware (Section 3.3.3). In addition to the neutron detector and polarimeter counts, pulses from the beam current integration and dead-time measurements are recorded.

The fast spin-reversal is controlled by a NIM Spin State Control (SSC) module constructed in the TUNL electronics shop. The module produces an eight-step spin sequence: $+--+-++-$ which cancels the effects of detector drifts to second order in time [Kos90]. All data fed to the data acquisition system pass through a Phillips 706 sixteen-channel discriminator. Gate and delay generators are used to create a veto signal which blocks the data during a spin reversal (Figure 3.30). One pair of gate and delay generators determine the exact timing, vetoing the data starting 2 ms before a spin reversal until 5 ms past. This amount of time is needed to insure that the polarization of the source has stabilized [Kos90]. A second pair of gate and delay generators blank the output of the first when an inhibit signal is received by the SSC. This arrangement allows the timing circuits of the first set to

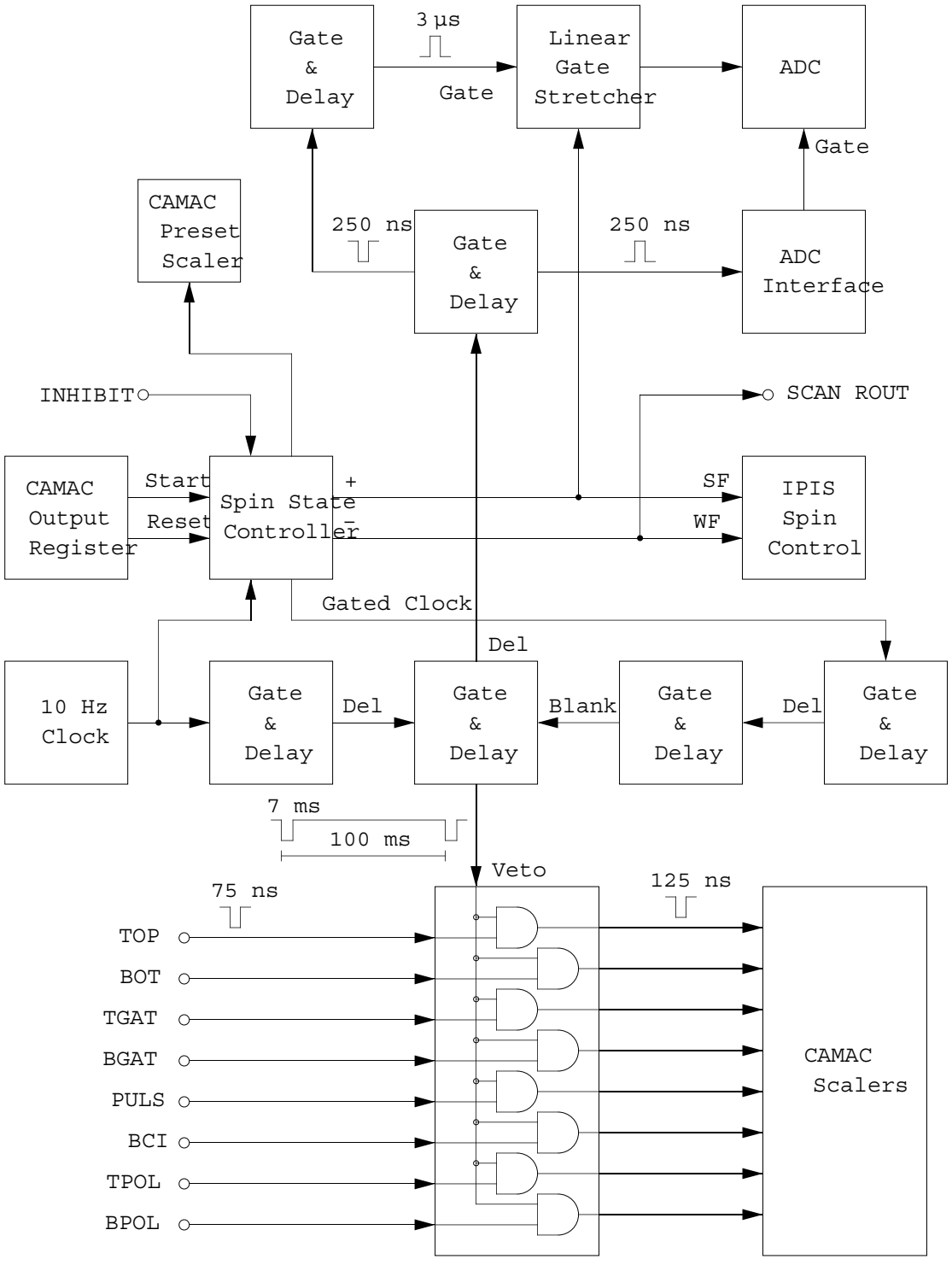

Figure 3.30: Data Acquisition Electronics for $\Delta\sigma_T$ Measurements

run continuously, avoiding drifts which occur when they are turned on and off. Data collection is inhibited when the beam current drops below a preset level and while writing the data to disk at the end of a run. The SSC determines the spin state of the ion source by sending TTL level signals to the ABPIS through fiber optic cables. The signals modulate the RF supplies of the two transition units. The SSC provides duplicates of these signals, labeled "+" and "−", for routing information. The "+" signal is read into an analog-to-digital converter (ADC) to signal the computer that a spin reversal has occurred. The computer reads all the CAMAC scalers and stores them according to spin state, a high value in the ADC indicating spin *up*, and a low spin *down*. At the end of an eight-step sequence, the CAMAC preset is decremented. A timing diagram is shown in Figure 3.31. The data are stored in the computer as spectra of counts versus time. Each time channel corresponds to one 800 ms eight-step spin sequence. There are two spectra for each scaler, corresponding to the two spin states. A run is comprised of 1023 such spin sequences. At the end of a run, the data are written to disk and asymmetries are calculated for display on the control-room monitor. The end of a run is signaled by the CAMAC preset scaler reaching zero.

The beam profile monitor (BPM) operates by rotating a helical wire through the proton beam. The geometry is such that the wire travels across the beam first horizontally and then vertically [Nat84]. The current collected by the wire is preamplified before being sent to the control room. In addition, a magnetic pickup on the rotating shaft picks up signals from three magnets mounted on the chamber. The first magnet produces the strongest signal and is used as a trigger to indicate the beginning of a scan. The other magnets generate fiducial marks which indicate the centers of the x and y passes, respectively. The signals from the collector and the fiducials pass through isolation amplifiers since they are referenced to dirty ground. In addition, the fiducial signal is split with one branch going through a broad-band isolation transformer to preserve timing information. The trigger signal (the largest of the fiducial marks) fires an EG&G T140/N zero-crossing detector. The output of the zero-crossing detector starts a linear ramp. The collector signal, the fiducial signal, and the ramp are sampled by linear gate stretchers before being sent to ADC's. The gate signals are generated by a variable frequency clock which runs during the ramp. This setup is shown in Figure 3.32.

The beam profile information (Figures 3.33 and 3.34) is stored in two sets of

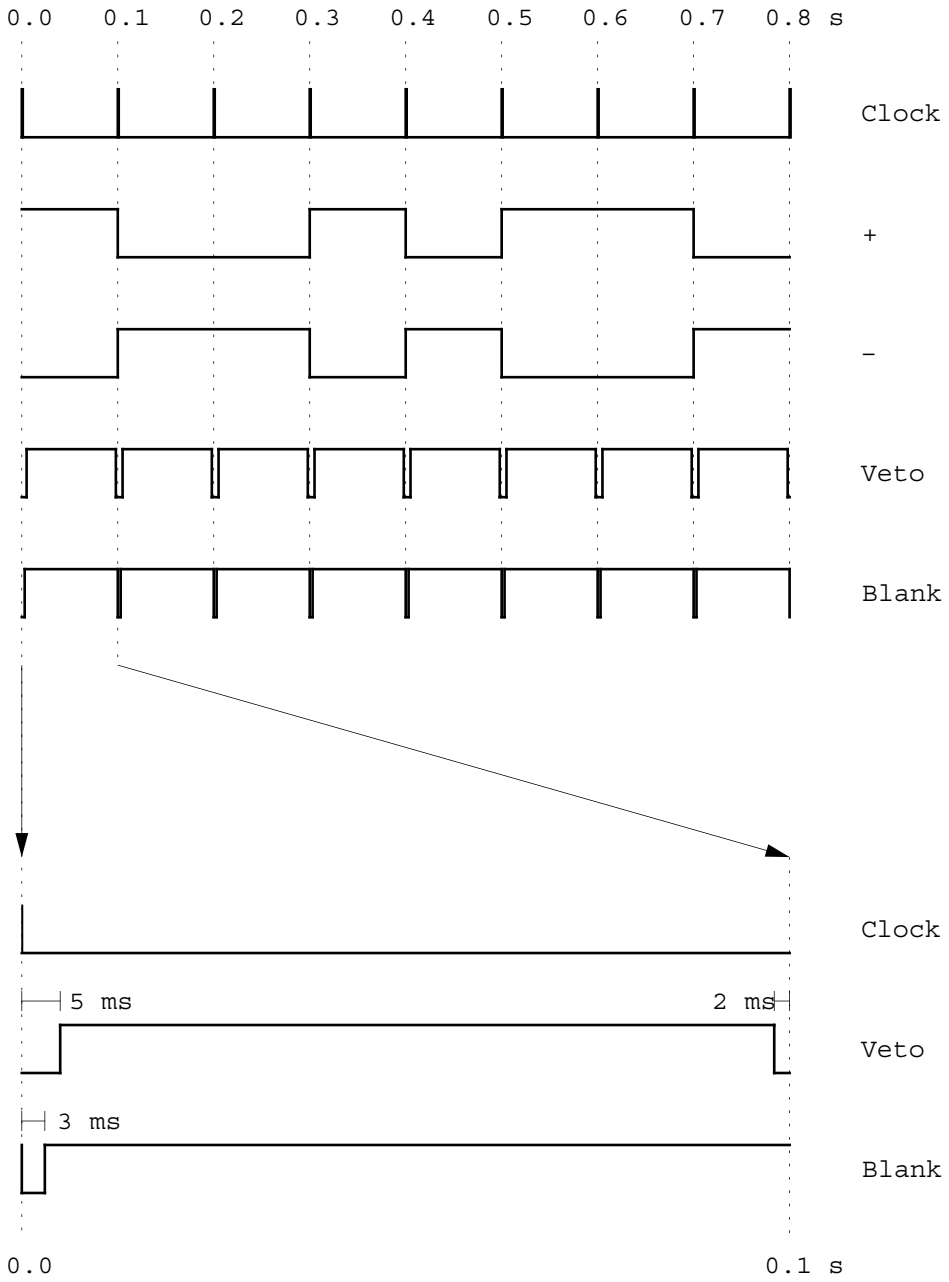

Figure 3.31: Data Acquisition Timing Diagram

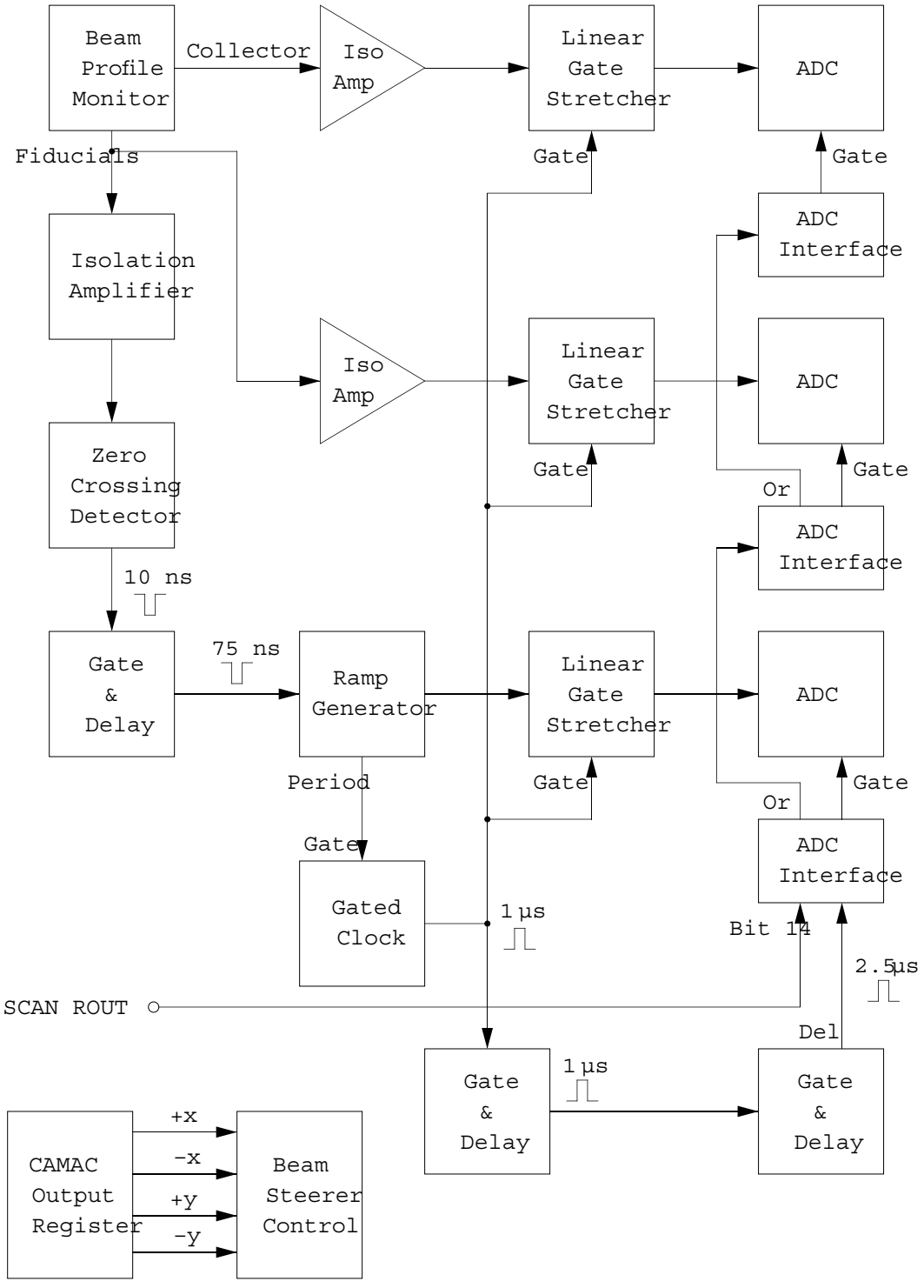

Figure 3.32: Beam Profile Monitor Feedback Steering Electronics

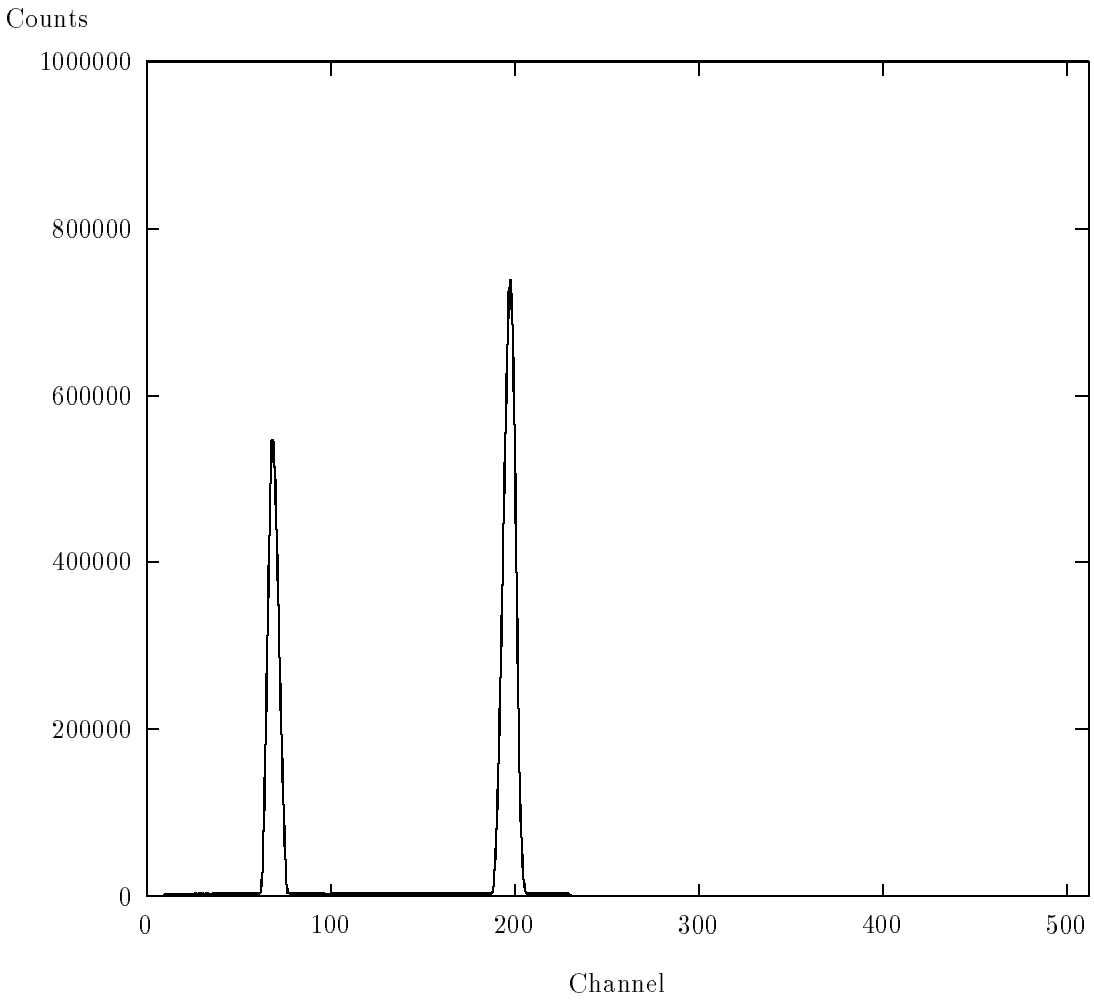

Figure 3.33: Beam Profile Monitor Collector Spectrum

spectra. The first set has the ramp as the x-axis and the collector as the y-axis. The second again has the ramp as the x-axis, and the fiducials as the y-axis. Each set has one spectrum for spin *up*, one for spin *down*, and one which is the sum of the two. A FORTRAN code running as a subprocess calculates the centroids of the two collector peaks and the centers of the x and y fiducial marks. Bits are sent at 1 s intervals to an automatic steerer according to the relative position of the centroids and fiducial marks. The output signals are capacitively coupled to preserve the ground isolation.

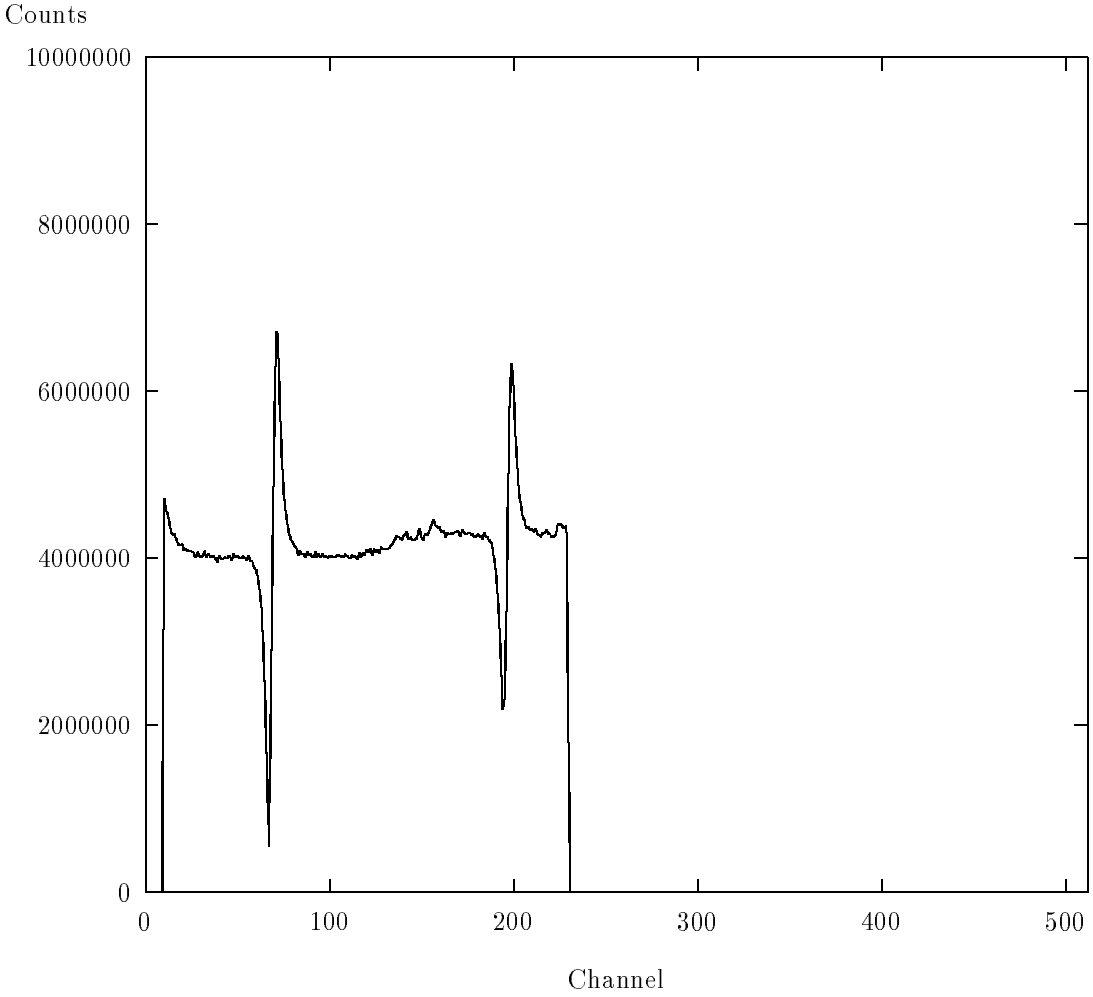

Figure 3.34: Beam Profile Monitor Fiducial Spectrum

3.6.2 Neutron Polarization Measurements

For the neutron polarization measurement, it is necessary to measure asymmetries to an accuracy of order 5×10^{-3}. Although this requirement is somewhat relaxed compared to the $\Delta\sigma_T$ measurements, the fast spin reversal techniques described above are used. There are three major differences, however. First, the signals obtained from the polarimeter are in the form of energy and time-of-flight information and must be read by ADC's. In contrast, the detector signals for the $\Delta\sigma_T$ measurements are simply read by scalers. Second, the routing of the scaler signals is performed by fanning out the signals to two sets of scalers and selectively enabling just one set according to the spin state (Figures 3.35 and 3.36) instead of using software to perform the routing. Third, the ADC and scaler data is accumulated for an entire run instead of being stored in 800 ms time slices.

Two ADC's are used for the neutron polarimeter. The first records the alpha recoil energy signal from the center detector. Gates for this ADC can come from coincidences with any of the four neutron detectors (Section 3.4). The gates pass through the Phillips 706 discriminator module so that they are vetoed during spin reversal as are the scaler signals. Next, coincidences are formed between gates from the forward detectors and their corresponding PSD signals. The PSD coincidences for the backward detectors are generated at an earlier stage. Routing information is created by the ADC interface according to the neutron detector and the spin state. Delays are applied to the linear signal and the gates to allow a proper time relation to be established. The second ADC records the neutron time-of-flight signals from the four neutron detectors. The linear signals are are fanned together using sum and invert amplifiers. The gate for this ADC comes from the interface for the first ADC so that the ADC's are triggered together and both alpha energy and neutron time-of-flight are recorded for each event. The events are stored in two-dimensional spectra with neutron time-of-flight as the x-axis and alpha recoil energy as the y-axis. There are two spectra for each of the four neutron detectors, corresponding to the two spin states.

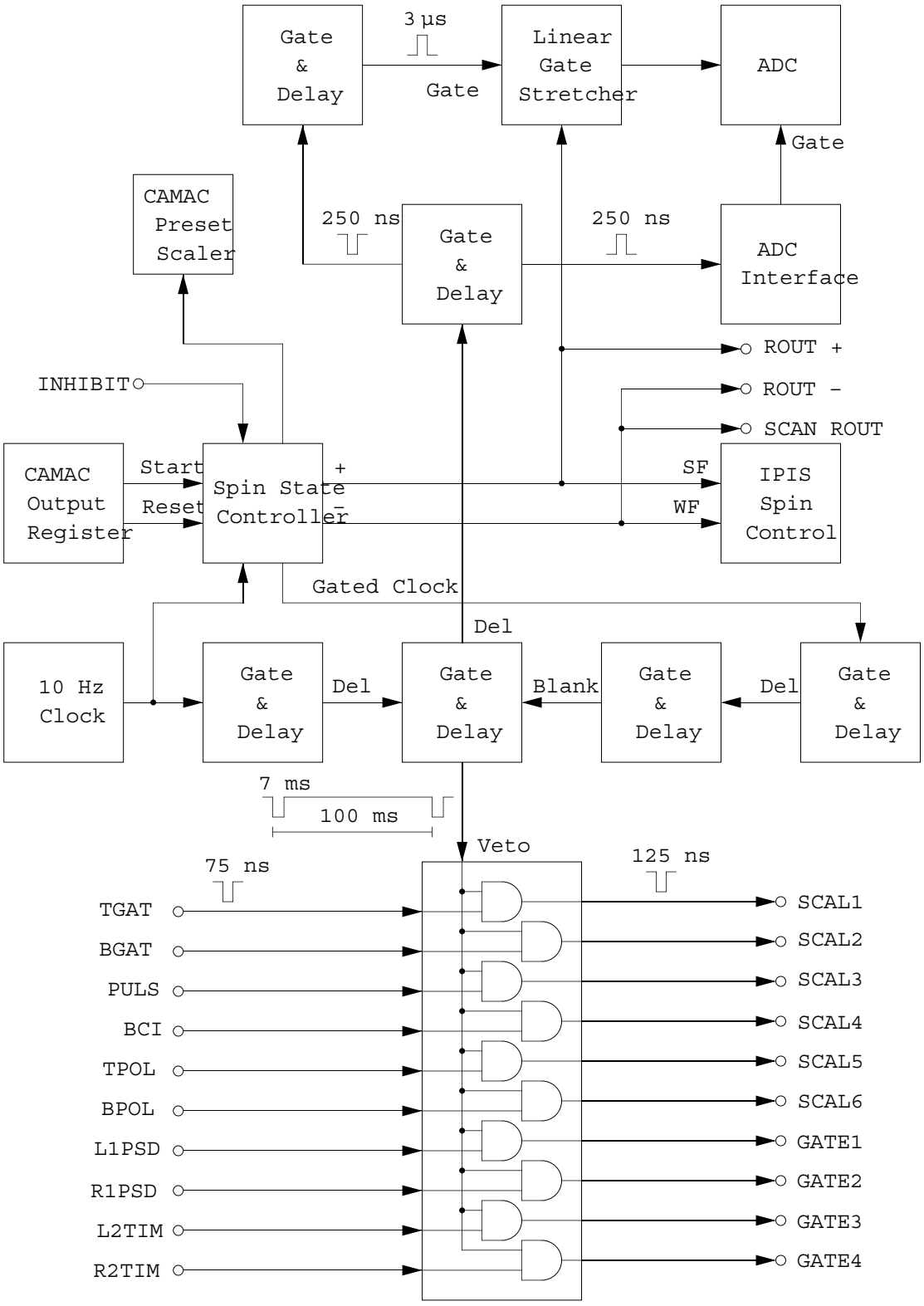

Figure 3.35: Neutron Polarimeter Data Acquisition Electronics (Part 1)

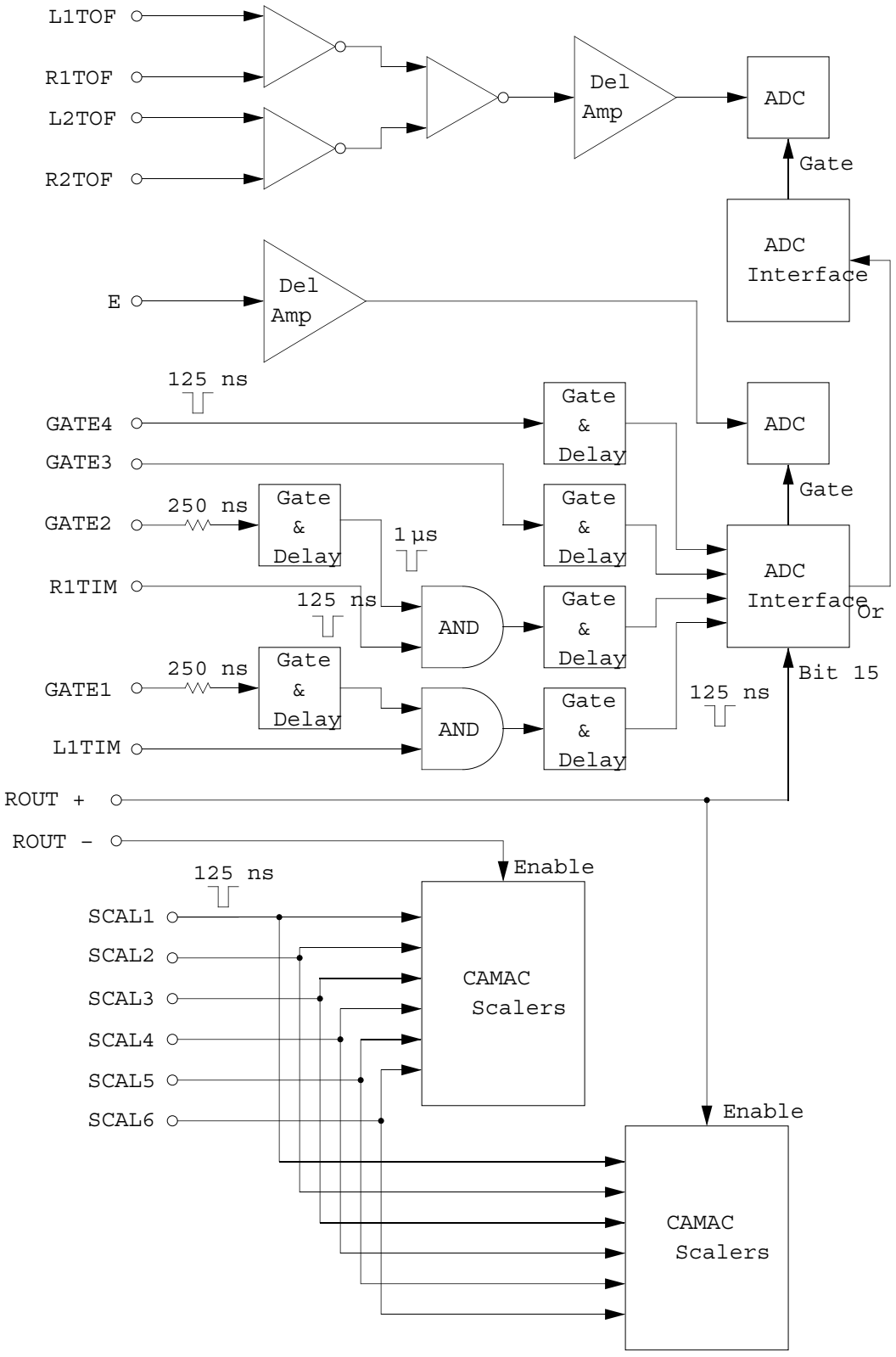

Figure 3.36: Neutron Polarimeter Data Acquisition Electronics (Part 2)

Chapter 4

Experimental Procedure

4.1 $\Delta\sigma_T$ Measurements

As the total cross section is related to the forward scattering amplitude by the optical theorem, $\Delta\sigma_T$ can be measured by observing the change in transmitted neutron flux through the polarized target upon reversing the beam polarization. The transmitted flux, N, is given by

$$N = N_0 e^{-x\sigma} \tag{4.1}$$

where N_0 is the incident flux, x is the target thickness, and σ is the cross section. For the case of a polarized beam and a polarized target, the cross section can be expressed as

$$\sigma_{\pm} = \sigma_0 - \frac{1}{2} P_n^{\pm} P_T \Delta\sigma \tag{4.2}$$

where σ_0 is the unpolarized cross section, P_T is the proton target polarization, and $P_n^{\pm}$ are the neutron beam polarizations for the two spin-states. The beam polarizations can be expressed in a more convenient form as

$$P_n^{\pm} = \bar{P}_n \pm P_n \tag{4.3}$$

where

$$\begin{aligned} \bar{P}_n &= \frac{P_n^+ + P_n^-}{2}, \\ P_n &= \frac{P_n^+ - P_n^-}{2}. \end{aligned} \tag{4.4}$$

The neutron transmissions for the transverse geometry are then

$$N_{\pm} = N_0 e^{-x\left(\sigma_0 - \frac{1}{2}\bar{P}_n P_T \Delta\sigma_T\right)} e^{\pm\frac{1}{2}P_n x P_T \Delta\sigma_T}. \tag{4.5}$$

An asymmetry can be formed using the two beam transmissions

$$\varepsilon = \frac{N_+ - N_-}{N_+ + N_-} \tag{4.6}$$

$$= \frac{e^{+\frac{1}{2}P_n P_T x \Delta\sigma_T} - e^{-\frac{1}{2}P_n P_T x \Delta\sigma_T}}{e^{+\frac{1}{2}P_n P_T x \Delta\sigma_T} + e^{-\frac{1}{2}P_n P_T x \Delta\sigma_T}} \tag{4.7}$$

$$= \tanh\left(\frac{1}{2}P_n P_T x \Delta\sigma_T\right) \tag{4.8}$$

which is independent of the incident flux and the unpolarized cross section. Since the argument of the hyperbolic tangent is small (≤ 0.025), the approximation $\tanh(x) \approx x$ can be made

$$\varepsilon = \frac{1}{2}P_n P_T x \Delta\sigma_T. \tag{4.9}$$

Then in order to determine $\Delta\sigma_T$, the neutron transmission asymmetry, ε, must be measured as well as the two polarizations, P_n and P_T, and the target thickness, x. The neutron beam polarization, P_n, can be inferred from the proton beam polarization measured by the carbon-foil polarimeter. This measurement is relatively fast, with a sufficient statistical accuracy being reached in a few minutes, allowing it to be repeated every few hours. The product of the proton target polarization and target thickness, $P_T x$, is determined by measuring the neutron transmission asymmetry at an energy below 2 MeV where the uncertainty in $\Delta\sigma_T$ is small. This measurement, however, is slow, taking on the order of 12 hours to reach a sufficient statistical accuracy. Because of the length of time required, this measurement is usually only performed once, at the beginning of an experiment. In addition, the instrumental asymmetry of the system due to errors such as beam misalignment must be measured. This requires taking neutron transmission asymmetry data with the target warmed to a high enough temperature (> 800 mK) to depolarize the protons. The true asymmetry is then taken to be the difference between the cold and warm values. Because the cold and warm measurements contribute equally to the final uncertainty, the most efficient use of time is to measure them to equal statistical precision.

The cooling of the target begins 3–5 days before the start of measurements, which typically last for 7 days. This allows the dilution refrigerator to run for at least 48 hours before the target is needed, giving it time to reach thermal equilibrium. Because of the long time required to polarize the target, the cold measurements are made first. The beam polarization is measured at an energy where the $^{12}C(p,p_0)^{12}C$ analyzing power is known, and the energy is then lowered to $E_n = 1.94$ MeV to determine $P_T x$. TSCA windows are set for the carbon-foil polarimeter and PSD parameters are adjusted for the neutron detectors. The gas cell in front of the tritiated-titanium foil is evacuated and then filled with helium. Helium is added to the cell approximately once per day to replace the gas which diffuses through the beam entrance foil. Neutron transmission asymmetries are measured for approximately 12 hours at this energy. Beam polarization measurements are made every few hours to monitor the state of the polarized ion source.

Once the target polarization has been determined, measurements are made at higher neutron energies where $\Delta\sigma_T$ is not known. With each energy change, the polarimeter TSCA windows and neutron detector PSD settings must be reset. Data is collected for 18–48 hours at each energy, with beam polarization measurements made every few hours. After making measurements at all energies of interest, the target is warmed to approximately 1 K. The asymmetry measurements are then repeated at each energy, including 1.94 MeV.

4.2 $K_y^{y'}$ Measurements for the $^3\mathbf{H}(\vec{\mathbf{p}},\vec{\mathbf{n}})^3\mathbf{He}$ Reaction

The polarization-transfer coefficient, $K_y^{y'}$, can be written as the ratio of outgoing neutron polarization to incoming proton polarization

$$K_y^{y'} = \frac{P_n}{P_p}. \tag{4.10}$$

The measurement of the proton beam polarization is discussed in Section 3.2 (see Equation 3.7). The neutron polarization is measured by scattering the neutrons from helium. The scattered neutron fluxes observed by a pair of detectors placed

symmetrically about the beam direction can be written as [Hai72]

$$\begin{aligned} N_{L\pm} &= N_{0\pm}(1 + P_n^{\pm} A_y)\epsilon_L, \\ N_{R\pm} &= N_{0\pm}(1 - P_n^{\pm} A_y)\epsilon_R, \end{aligned} \tag{4.11}$$

where $\pm$ refers to the spin state, $N_{0\pm}$ are the neutron fluxes into the detector for an unpolarized beam, A_y is the analyzing power, and ϵ contains the detector efficiency and solid angle. Since the flux from the polarized ion source is different for the two spin states, N_{0+} and N_{0-} must be specified separately. $N_{0\pm}$ and ϵ can be eliminated by forming the following ratio of count rates.

$$\frac{N_{L+}}{N_{L-}}\frac{N_{R-}}{N_{R+}} = \frac{N_{0+}\epsilon_L(1 + P_{n+}A_y)N_{0-}\epsilon_R(1 - P_{n-}A_y)}{N_{0-}\epsilon_L(1 + P_{n-}A_y)N_{0+}\epsilon_R(1 - P_{n+}A_y)} \tag{4.12}$$

$$= \frac{(1 + P_{n+}A_y)(1 - P_{n-}A_y)}{(1 + P_{n-}A_y)(1 - P_{n+}A_y)} \tag{4.13}$$

Substituting for $P_{n\pm}$ using Equation 4.3 gives

$$(1 + P_{n\pm}A_y)(1 - P_{n\mp}A_y) = [1 + (\bar{P}_n \pm P_n)A_y][1 - (\bar{P}_n \mp P_n)A_y], \tag{4.14}$$

$$= (1 \pm P_n A_y)^2 - \bar{P}_n^2 A_y^2, \tag{4.15}$$

$$\approx (1 \pm P_n A_y)^2, \tag{4.16}$$

where the approximation $\bar{P}_n^2 A_y^2 \ll 1$ has been made. Since P_{n+} and P_{n-} are opposite in sign and equal in magnitude to within 20%, this is a valid approximation. The neutron polarimeter asymmetry, ε_{npol}, is then defined as

$$\varepsilon_{npol} = \frac{\sqrt{\frac{N_{L+}}{N_{L-}}\frac{N_{R-}}{N_{R+}}} - 1}{\sqrt{\frac{N_{L+}}{N_{L-}}\frac{N_{R-}}{N_{R+}}} + 1}, \tag{4.17}$$

$$= P_n A_y. \tag{4.18}$$

The neutron detectors are placed at an an angle corresponding to a maximum in the product of the square of the ^{4}He analyzing power and the cross section, $A_y^2\sigma$.

At most energies, two detector pairs are used to take advantage of both the forward and backward maxima. The fight path from the helium cell to the neutron detectors is set as a compromise between time resolution and counting rate. The coincidence timing between the center and side detectors is set using a ^{22}Na source. The neutron polarization is measured continuously for a period of approximately 24 hours. Such a long time is necessary due to the low counting rate. The proton polarization is measured approximately every 2 hours. With each change in energy, the detector angles are changed and the amplifier gains and coincidence timing is checked. In addition, PSD must be set for each detector at each energy.

Chapter 5

Data Analysis

5.1 $\Delta\sigma_T$ Measurements

Following Equation 4.8, $\Delta\sigma_T$ can be written in terms of the experimental parameters as

$$\Delta\sigma_T = \frac{2\varepsilon}{xP_TP_n}, \tag{5.1}$$

where ε is the observed asymmetry in neutron transmission, P_n is the neutron beam polarization, P_T is the proton target polarization, and x is the target thickness. As discussed in Section 2.2, $\Delta\sigma_T$ is constrained at low energies by kinematic considerations and by the properties of the deuteron. At energies below 2 MeV, the values of $\Delta\sigma_T$ obtained from potential models, phase-shift analysis, and effective-range parameters are in good agreement. Thus it is possible to write

$$\Delta\sigma_T(E) = \left[\frac{\frac{\varepsilon}{P_n}(E)}{\frac{\varepsilon}{P_n}(E_0)}\right]\Delta\sigma_T(E_0), \tag{5.2}$$

where $E_0 \leq 2$ MeV is the calibration energy at which $\Delta\sigma_T$ can be calculated, and E is a higher energy at which $\Delta\sigma_T$ is to be determined. The asymmetry at E_0 effectively measures the product of target thickness and polarization, xP_T. Normalizing to the asymmetry at E_0 eliminates all energy-independent quantities from the analysis. Additionally, measurements made with the target unpolarized allow the subtraction of instrumental asymmetries due to effects such as target misalignment. The data has been taken in four sets, labelled A, B, C, and D, each having a different target polarization. In two cases, a measurement has been repeated within the same set.

These measurements are distinguished by the subscripts 1 and 2. In the analysis of the data, statistical and systematic errors will be treated separately.

5.1.1 Calculation of the Neutron-Transmission Asymmetries

The data is collected in time-ordered spectra with each channel giving the number of counts collected during one eight-step spin sequence lasting 800 ms. Since the data is sorted by spin state, there are two spectra for each scaler value corresponding to data taken with spin *up* and with spin *down*. Because the amount of time spent collecting data in each spin state is determined by hardware, interrupting the data collection will make these times unequal during the current spin sequence. This problem occurs when the beam current falls outside of the discriminator window and an inhibit signal is sent to the data acquisition system. These events must be detected by the off-line analysis and the data from these spin sequences rejected. This task is accomplished by analyzing the dead-time pulser spectra for irregularities.

The dead-time pulser produces regular pulses with a frequency of approximately 100 kHz, equivalent to 40,000 counts per channel in each spin state. The pulser is stable to approximately 5×10^{-4} over the time spanned by an entire spectrum and any deviations larger than this value indicate that the time spent collecting data was incorrect. When data collection is interrupted, one or both of the pulser spectra will show a spike or dip in an otherwise flat spectrum (Figure 5.1). These irregularities are used to identify the channels to be rejected by the FORTRAN program CHAY. This program makes three passes through each set of spectra in evaluating the data. The first pass generates a histogram of the number of channels versus counts per channel with a bin width of 250 counts. The first-pass average counts per channel is then taken to be that of the bin with the most number of channels. This method of estimating the average removes most of the spikes and dips which would otherwise bias the result, as they are not statistically distributed. The second pass calculates the average pulser counts per channel, excluding all channels which are more than 200 counts away from the first-pass average. This value is essentially the average which would be measured if no interruptions in the data collection occur. In addition, a standard deviation is calculated. The third and final pass extracts the data, excluding

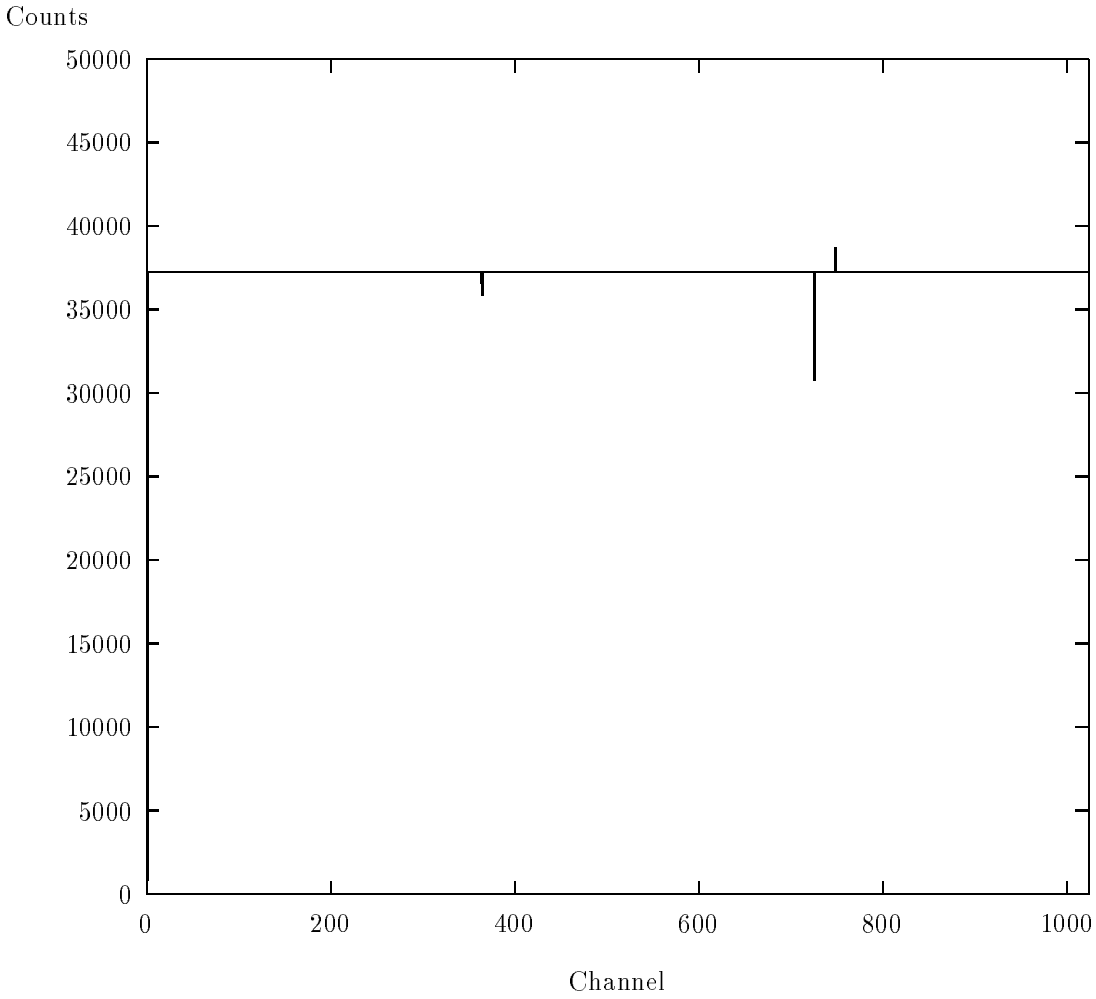

Figure 5.1: Dead-Time Pulser Spectrum

all channels where the pulser counts in either spectrum are more than four standard deviations away from the average. Since the dead-time pulser is independent of the detectors, this process in no way affects the statistical distribution of the neutron data. Typically, less than 1% of the data must be rejected.

The data which is not rejected is used to calculate asymmetries in the transmitted neutron flux on a channel-by-channel basis. First, neutron yields, $\tilde{N}$, are calculated by normalizing the detector counts, N, to the integrated beam current, I, and multiplying by the dead-time correction, δ.

$$\tilde{N} = \frac{N}{I}\delta \tag{5.3}$$

The asymmetry for either of the two neutron detectors is then

$$\varepsilon = \frac{\tilde{N}_+ - \tilde{N}_-}{\tilde{N}_+ + \tilde{N}_-} \tag{5.4}$$

$$= \frac{\eta - \tau}{\eta + \tau} \tag{5.5}$$

where the subscripts "+" and "−" refer to the spin state and

$$\eta = \frac{N_+\delta_+}{N_-\delta_-}, \tag{5.6}$$

$$\tau = \frac{I_+}{I_-}. \tag{5.7}$$

Since the detector counts obey a Poisson distribution, the standard uncertainty is simply given by the square-root of the number of counts.

$$\Delta N = \sqrt{N} \tag{5.8}$$

The counts from the beam current integration, however, are not normally distributed. Instead, the uncertainty arises from the finite resolution due to digitization. An uncertainty of 1/2 count occurs when changing spin state. Because of the order of the eight-step sequence $(+--+-++-)$, three such changes occur for each spin state.[1] Adding the uncertainties in quadrature gives the uncertainty in the integrated

[1]Since the time spent vetoing data during spin reversal is short compared to the time between BCI pulses, $--$ and $++$ are treated as if they are one continuous measurement in this analysis.

current for one spin state.

$$\Delta I = \frac{\sqrt{3}}{2} \tag{5.9}$$

From these results $\Delta\eta$ and $\Delta\tau$ can be found.

$$\Delta\eta = \eta\sqrt{1/N_+ + 1/N_-} \tag{5.10}$$

$$\Delta\tau = \frac{\sqrt{3}}{2}\tau\sqrt{1/I_+^2 + 1/I_-^2} \tag{5.11}$$

The uncertainty in the asymmetry for one detector is then

$$\Delta\varepsilon = \frac{2\eta\tau}{(\eta+\tau)^2}\sqrt{1/N_+ + 1/N_- + \frac{3}{4}(1/I_+^2 + 1/I_-^2)}. \tag{5.12}$$

The asymmetries for the two detectors can be combined in two ways. Averaging the two asymmetries gives the same result as a single detector located at 0°. It is this value which will be used to obtain $\Delta\sigma_T$. Taking the difference of the two asymmetries gives essentially a measure of the analyzing power for the ^{3}H($\vec{\mathrm{p}}$,$\vec{\mathrm{n}}$)^{3}He source reaction and is proportional to the neutron beam polarization. The sum and difference asymmetries are defined as

$$\varepsilon_S = \frac{\varepsilon_T + \varepsilon_B}{2}, \tag{5.13}$$

$$\varepsilon_D = \frac{\varepsilon_T - \varepsilon_B}{2}. \tag{5.14}$$

The uncertainties for these combined asymmetries, however, cannot be obtained simply by adding the uncertainties for the individual asymmetries in quadrature. Since ε_T and ε_B are calculated using the same beam current values, I_+ and I_-, a correlation exists. The uncertainties in ε_S and ε_D are given properly as

$$\Delta\varepsilon_S = \sqrt{\frac{1}{4}(\Delta{\varepsilon_T}^2 + \Delta{\varepsilon_B}^2) + \frac{2\eta_T\eta_B}{(\eta_T+\tau)^2(\eta_B+\tau)^2}\Delta\tau^2}, \tag{5.15}$$

$$\Delta\varepsilon_D = \sqrt{\frac{1}{4}(\Delta{\varepsilon_T}^2 + \Delta{\varepsilon_B}^2) - \frac{2\eta_T\eta_B}{(\eta_T+\tau)^2(\eta_B+\tau)^2}\Delta\tau^2}. \tag{5.16}$$

The correlation term increases the uncertainty in ε_S and decreases it in ε_D.

Once the asymmetries have been calculated for each 800 ms channel and for all runs, they are averaged and standard deviations are calculated.

$$\bar{\varepsilon} = \left(\sum_{i=1}^{n} \frac{\varepsilon_i}{\Delta\varepsilon_i^2}\right) \Delta\bar{\varepsilon}^2 \tag{5.17}$$

$$\Delta\bar{\varepsilon} = \sqrt{\frac{1}{\sum_{i=1}^{n} 1/\Delta\varepsilon_i^2}} \tag{5.18}$$

$$\sigma_{\bar{\varepsilon}} = \sqrt{\frac{\sum_{i=1}^{n} (\varepsilon_i - \bar{\varepsilon})^2/\Delta\bar{\varepsilon}^2}{n(n-1)}} \tag{5.19}$$

Here, n is the total number of 800 ms measurements and $\sigma_{\bar{\varepsilon}}$ is the reduced standard deviation. The results for the neutron detector asymmetries for all measurements are tabulated in Table 5.1. In all subsequent calculations, the standard deviations will be used as the uncertainties in these asymmetries.

5.1.2 Calculation of the Average Neutron Beam Polarization

The neutron polarization is determined by measuring the polarization of the proton beam with a carbon analyzer as described in Section 3.2. These measurements are typically made every 2–4 hours, with the exception of data at the calibration energy $E_0 = 1.94$ MeV. At this energy the analyzing power is small (approximately -0.15), making beam polarization measurements susceptible to systematic effects. For this reason, polarization measurements are made at a higher energy either before or after the data is taken. In some cases, the polarization is measured both before and after and the results averaged. Polarimeter asymmetries are measured for spin *up* and spin *down* and the difference taken to cancel systematic effects.

$$\varepsilon_{ppol} = \frac{\varepsilon_{ppol+} - \varepsilon_{ppol-}}{2} \tag{5.20}$$

Runs taken between two polarization measurements are assigned a polarimeter asymmetry equal to the average of the two. Runs at the beginning or end of a $\Delta\sigma_T$ measurement are assigned an asymmetry by a linear extrapolation from the two closest

Target Polarized											
E_n (MeV)	Set	n	$\bar{\varepsilon}_S$	$\pm$	$\Delta\bar{\varepsilon}_S$	$(\sigma_{\bar{\varepsilon}_S})$	$\bar{\varepsilon}_D$	$\pm$	$\Delta\bar{\varepsilon}_D$	$(\sigma_{\bar{\varepsilon}_D})$	Unit
1.94	A	47,174	179.60	$\pm$	4.36	(4.52)	-70.44	$\pm$	4.08	(4.21)	10^{-4}
	B	48,651	-115.00	$\pm$	5.06	(5.27)	60.72	$\pm$	4.74	(4.90)	10^{-4}
	C	49,428	-177.10	$\pm$	6.26	(6.89)	68.83	$\pm$	6.00	(6.73)	10^{-4}
	D_1	39,448	-107.20	$\pm$	4.18	(4.42)	56.15	$\pm$	3.52	(3.62)	10^{-4}
	D_2	7,127	-114.40	$\pm$	9.97	(11.03)	52.53	$\pm$	8.44	(8.50)	10^{-4}
3.65	C	57,865	-33.81	$\pm$	3.22	(3.31)	-26.09	$\pm$	3.03	(3.13)	10^{-4}
	D	20,263	-25.99	$\pm$	6.29	(6.46)	-23.64	$\pm$	5.38	(5.39)	10^{-4}
4.42	A	63,316	7.45	$\pm$	2.74	(2.75)	-44.47	$\pm$	2.52	(2.52)	10^{-4}
4.91	A	66,302	1.54	$\pm$	2.83	(2.85)	-26.10	$\pm$	2.64	(2.64)	10^{-4}
5.21	D_1	44,931	0.72	$\pm$	5.08	(5.14)	17.75	$\pm$	4.37	(4.40)	10^{-4}
	D_2	185,087	-0.06	$\pm$	1.39	(1.41)	20.96	$\pm$	1.31	(1.31)	10^{-4}
5.81	A	47,236	-4.83	$\pm$	3.00	(3.03)	-10.59	$\pm$	2.84	(2.85)	10^{-4}
6.25	B	42,061	6.24	$\pm$	5.54	(5.59)	15.19	$\pm$	5.16	(5.25)	10^{-4}
	C	142,101	5.06	$\pm$	2.33	(2.36)	16.24	$\pm$	2.24	(2.26)	10^{-4}

Target Unpolarized											
E_n (MeV)	Set	n	$\bar{\varepsilon}_S$	$\pm$	$\Delta\bar{\varepsilon}_S$	$(\sigma_{\bar{\varepsilon}_S})$	$\bar{\varepsilon}_D$	$\pm$	$\Delta\bar{\varepsilon}_D$	$(\sigma_{\bar{\varepsilon}_D})$	Unit
1.94	A	37,624	-7.21	$\pm$	4.94	(5.12)	-68.81	$\pm$	4.60	(4.77)	10^{-4}
	C	54,789	20.21	$\pm$	5.92	(6.70)	60.86	$\pm$	5.65	(6.40)	10^{-4}
	D	47,699	4.54	$\pm$	4.06	(4.80)	60.62	$\pm$	3.50	(3.55)	10^{-4}
3.65	C	67,179	4.76	$\pm$	2.92	(2.98)	-16.61	$\pm$	2.76	(2.85)	10^{-4}
	D	23,126	3.60	$\pm$	4.51	(4.71)	-29.15	$\pm$	4.07	(4.04)	10^{-4}
4.42	A	60,624	2.93	$\pm$	2.51	(2.50)	-51.89	$\pm$	2.37	(2.37)	10^{-4}
4.91	A	64,152	-3.03	$\pm$	2.53	(2.56)	-24.47	$\pm$	2.39	(2.39)	10^{-4}
5.21	D	221,298	-3.32	$\pm$	1.38	(1.39)	23.87	$\pm$	1.30	(1.29)	10^{-4}
5.81	A	68,713	-1.08	$\pm$	2.44	(2.47)	-4.51	$\pm$	2.32	(2.31)	10^{-4}
6.25	B	173,181	-3.11	$\pm$	2.57	(2.59)	23.55	$\pm$	2.40	(2.44)	10^{-4}
	C	128,196	-4.88	$\pm$	2.35	(2.38)	22.04	$\pm$	2.27	(2.30)	10^{-4}

Table 5.1: Average Neutron-Transmission Asymmetries

E_p (MeV)	n	ℓ_{max}	χ^2_ν	$\frac{d\sigma}{d\Omega}$ (mb)	A_y^{exp}	$\pm$	ΔA_y^{exp}	A_y^{fit}	$\pm$	ΔA_y^{fit}
4.66	13	7	1.09	158.0	−0.50	$\pm$	0.03	−0.496	$\pm$	0.022
5.04	13	10	1.56	162.0	−0.72	$\pm$	0.01	−0.724	$\pm$	0.009
5.41	9	8	2.34	132.8	−0.521	$\pm$	0.026	−0.535	$\pm$	0.024
5.78	9	5	0.99	182.5	−0.779	$\pm$	0.041	−0.775	$\pm$	0.015
5.89	13	8	1.12	178.6	−0.849	$\pm$	0.034	−0.812	$\pm$	0.022
6.18	11	7	9.53	195.0	−0.82	$\pm$	0.01	−0.851	$\pm$	0.009
6.77	13	10	3.34	218.0	−0.53	$\pm$	0.01	−0.520	$\pm$	0.009
7.21	13	9	3.28	177.0	−0.30	$\pm$	0.02	−0.278	$\pm$	0.015
7.55	13	9	1.16	125.0	−0.36	$\pm$	0.02	−0.339	$\pm$	0.016
7.99	13	9	0.72	148.0	−0.14	$\pm$	0.02	−0.131	$\pm$	0.017
8.66	13	6	1.48	133.0	+0.00	$\pm$	0.02	−0.015	$\pm$	0.014
8.90	16	8	1.53	102.3	+0.124	$\pm$	0.041	+0.125	$\pm$	0.041
9.15	20	6	1.29	129.9	−0.011	$\pm$	0.044	−0.010	$\pm$	0.015
9.66	12	8	0.77	85.0	−0.342	$\pm$	0.058	−0.348	$\pm$	0.054

Table 5.2: Analyzing Power Fits for ^{12}C(p,p$_0$)^{12}C at $\theta_{lab} = 40°$

polarimeter measurements. The average polarimeter asymmetry for an entire $\Delta\sigma_T$ measurement is then calculated, weighting each asymmetry by the number of runs which it spans.

Analyzing powers for the polarimeter are determined from published data [Mos65, Ter68] for the elastic scattering of protons from carbon. The products of differential cross section, $\frac{d\sigma}{d\Omega}$, and analyzing power, A_y, are fit as a function of center-of-mass angle using first-order associated Legendre polynomials. The number of terms used in the fit, ℓ_{max}, is chosen at each energy to minimize the reduced chi-square, χ^2_ν. The results of the fit, A_y^{fit}, as well as the experimental value, A_y^{exp}, at the angle of interest ($\theta_{lab} = 40°$) are shown in Table 5.2, where n is the number of experimental data used in each fit. Proton beam polarizations are calculated using Equation 3.7 and neutron beam polarizations using Equation 3.8 and the depolarization factor listed in Table 3.6.

$$P_n = \frac{K_y^{y'} P_p}{P/P_0} \tag{5.21}$$

Table 5.3 lists the average beam polarizations, $\bar{P}_p$ and $\bar{P}_n$, for each measurement. The uncertainties, $\Delta\bar{P}_p$ and $\Delta\bar{P}_n$, come from uncertainties in the values of the carbon analyzing power and in the polarization-transfer coefficient and will be treated as

Target Polarized									
E_n (MeV)	E_p (MeV)	Set	$\bar{\varepsilon}_{ppol}$	$\bar{P}_p$	$\pm$	$\Delta\bar{P}_p$	$\bar{P}_n$	$\pm$	$\Delta\bar{P}_n$
1.94	5.89	A	-0.499	0.755	$\pm$	0.020	0.496	$\pm$	0.030
	7.21	B	0.151	-0.667	$\pm$	0.036	-0.438	$\pm$	0.034
	4.66	C	0.279	-0.691	$\pm$	0.031	-0.454	$\pm$	0.032
	4.66	D_1	0.245	-0.607	$\pm$	0.027	-0.399	$\pm$	0.028
	6.18	D_2	0.314	-0.453	$\pm$	0.005	-0.298	$\pm$	0.017
3.65	4.66	C	0.270	-0.669	$\pm$	0.030	-0.471	$\pm$	0.033
		D	0.213	-0.528	$\pm$	0.023	-0.372	$\pm$	0.025
4.42	5.41	A	-0.276	0.634	$\pm$	0.028	0.439	$\pm$	0.028
4.91	5.89	A	-0.496	0.751	$\pm$	0.020	0.532	$\pm$	0.023
5.21	6.18	D_1	0.290	-0.419	$\pm$	0.004	-0.310	$\pm$	0.011
		D_2	0.412	-0.595	$\pm$	0.006	-0.440	$\pm$	0.015
5.81	6.77	A	-0.285	0.673	$\pm$	0.012	0.547	$\pm$	0.020
6.25	7.21	B	0.153	-0.676	$\pm$	0.036	-0.559	$\pm$	0.036
		C	0.162	-0.716	$\pm$	0.039	-0.592	$\pm$	0.038

Target Unpolarized									
E_n (MeV)	E_p (MeV)	Set	$\bar{\varepsilon}_{ppol}$	$\bar{P}_p$	$\pm$	$\Delta\bar{P}_p$	$\bar{P}_n$	$\pm$	$\Delta\bar{P}_n$
1.94	5.41	A	-0.291	0.668	$\pm$	0.030	0.439	$\pm$	0.031
	7.21	C	0.150	-0.663	$\pm$	0.036	-0.436	$\pm$	0.034
	4.66	D	0.273	-0.675	$\pm$	0.030	-0.444	$\pm$	0.031
3.65	4.66	C	0.268	-0.664	$\pm$	0.029	-0.468	$\pm$	0.032
		D	0.273	-0.676	$\pm$	0.030	-0.476	$\pm$	0.033
4.42	5.41	A	-0.294	0.675	$\pm$	0.030	0.468	$\pm$	0.030
4.91	5.89	A	-0.440	0.666	$\pm$	0.018	0.472	$\pm$	0.021
5.21	6.18	D	0.430	-0.621	$\pm$	0.007	-0.460	$\pm$	0.016
5.81	6.77	A	-0.256	0.605	$\pm$	0.010	0.491	$\pm$	0.017
6.25	7.21	B	0.149	-0.659	$\pm$	0.036	-0.545	$\pm$	0.035
		C	0.154	-0.681	$\pm$	0.037	-0.563	$\pm$	0.036

Table 5.3: Average Proton and Neutron Beam Polarizations

systematic uncertainties. The analysis of the polarization-transfer coefficient, $K_y^{y'}$, is discussed in Section 5.2.

Knowledge of the beam polarizations allows neutron asymmetry measurements made at the same energy and target polarization to be combined. In order to simplify the calculation of uncertainties, whenever possible constants containing systematic uncertainties are not included in the normalization. Instead, they are factored in at a later stage. Thus, the neutron asymmetries are normalized to the proton polarimeter asymmetries whenever the analyzing power is the same for all measurements at that energy. This is possible at all energies except E_0 where the polarization has been determined at a variety of beam energies. In this case the neutron asymmetries are normalized to the proton beam polarization. Since the polarization-transfer coefficients are the same for all measurements at a given energy, $K_y^{y'}$ is not included until later in the analysis. Once normalized, the values are weighted by their statistical variance and averaged.

$$\bar{y} = \left[\sum_{i=1}^{n} \frac{y_i}{(\Delta_{stat}\, y_i)^2}\right] (\Delta_{stat}\, \bar{y})^2 \tag{5.22}$$

$$\Delta_{stat}\, \bar{y} = \sqrt{\frac{1}{\sum_{i=1}^{n} 1/(\Delta_{stat}\, y_i)^2}} \tag{5.23}$$

$$\Delta_{sys}\, \bar{y} = \left[\sum_{i=1}^{n} \frac{\Delta_{sys}\, y_i}{(\Delta_{stat}\, y_i)^2}\right] (\Delta_{stat}\, \bar{y})^2 \tag{5.24}$$

In these expressions y_i refers to either $\bar{\varepsilon}/\bar{\varepsilon}_{ppol}$ or $\bar{\varepsilon}/\bar{P}_p$. Note that unpolarized target data taken in different sets can be combined as the target polarization is the same in all cases, namely zero. This is not true, however, for the polarized target data, and asymmetries from different data sets cannot be combined at this point. Finally, instrumental asymmetries are removed by subtracting the warm data (target unpolarized) from the cold data (target polarized).

$$\bar{\varepsilon}/\bar{\varepsilon}_{ppol} = (\bar{\varepsilon}/\bar{\varepsilon}_{ppol})_c - (\bar{\varepsilon}/\bar{\varepsilon}_{ppol})_w \tag{5.25}$$

$$\bar{\varepsilon}/\bar{P}_p = (\bar{\varepsilon}/\bar{P}_p)_c - (\bar{\varepsilon}/\bar{P}_p)_w \tag{5.26}$$

The normalized asymmetries for the cases cold, warm, and cold minus warm as well

as the appropriate averages are shown in Tables 5.4, and 5.5. Here, Δ_{stat} and Δ_{sys} refer to the statistical and systematic uncertainties, respectively.

5.1.3 Calculation of $\Delta\sigma_T$

The next step in the analysis of the data is to combine measurements made at the same energy, but in different data sets which have different target polarizations. Since the target polarization information is contained in the calibration data, the other energies are normalized to these values, forming the ratio ξ.

$$\xi = \frac{\frac{\bar{\varepsilon}}{\bar{\varepsilon}_{ppol}}(E)}{\frac{\bar{\varepsilon}}{\bar{P}_p}(E_0)} \tag{5.27}$$

The averaging is performed as before and the results shown in Table 5.6.[2] $\Delta\sigma_T$ values can now be determined by including the constants from Equation 5.2 and multiplying by the calculated value of $\Delta\sigma_T$ at E_0.

$$\Delta\sigma_T = \left\{ A_y(E) \left[\frac{\rho(E)}{\rho(E_0)}\right] \left[\frac{K_y^{y'}(E_0)}{K_y^{y'}(E)}\right] \left[\frac{\frac{P}{P_0}(E_0)}{\frac{P}{P_0}(E)}\right] \Delta\sigma_T(E_0) \right\} \xi \tag{5.28}$$

The ^{12}C(p,p$_0$)^{12}C analyzing power for the calibration measurement does not appear in this expression as it was included at an earlier stage of the analysis. The corrections for unpolarized neutron background, ρ, are obtained from Table 3.5 and values for the polarization-transfer coefficient, $K_y^{y'}$ from Table 5.14. $\Delta\sigma_T(E_0)$ is obtained by taking the average of predictions from potential models, phase-shift analysis, and effective-range parameter calculations (Table 5.7).[3] The full Bonn is a relativistic meson exchange model. Bonn A, B, and C are one-boson exchange approximations to the full Bonn. The three differ only in the strength of the tensor interaction. A systematic uncertainty is assigned equal to the standard deviation of the predicted values. Table 5.8 lists the values of $\Delta\sigma_T$ obtained from the analysis of the data. The total uncertainty, Δ, is given by

$$\Delta = \sqrt{(\Delta_{stat})^2 + (\Delta_{sys})^2}. \tag{5.29}$$

[2] There exists a correlation in the values being averaged due to using the same warm asymmetries in both cases. The effect, however, is small in practice and will be ignored in this analysis.

[3] Predictions from the Paris and Nijmegen Potentials are not included as they use $^1S_0$ phase shifts obtained from p-p scattering. $^1S_0$ for n-p scattering is known to be different by several degrees.

Target Polarized							
E_n (MeV)	Set	$(\bar{\varepsilon}/\bar{\varepsilon}_{ppol})_c$	$\pm$	Δ_{stat}	$\pm$	Δ_{sys}	Unit
3.65	C	-125.22	$\pm$	12.26	$\pm$	0.00	10^{-4}
	D	-122.02	$\pm$	30.33	$\pm$	0.00	10^{-4}
4.42	A	-26.99	$\pm$	9.96	$\pm$	0.00	10^{-4}
4.91	A	-3.11	$\pm$	5.75	$\pm$	0.00	10^{-4}
5.21	D_1	2.48	$\pm$	17.72	$\pm$	0.00	10^{-4}
	D_2	-0.15	$\pm$	3.42	$\pm$	0.00	10^{-4}
	Average	-0.06	$\pm$	3.36	$\pm$	0.00	10^{-4}
5.81	A	16.95	$\pm$	10.63	$\pm$	0.00	10^{-4}
6.25	B	40.78	$\pm$	36.54	$\pm$	0.00	10^{-4}
	C	31.24	$\pm$	0.00	$\pm$	0.00	10^{-4}

Target Unpolarized							
E_n (MeV)	Set	$(\bar{\varepsilon}/\bar{\varepsilon}_{ppol})_w$	$\pm$	Δ_{stat}	$\pm$	Δ_{sys}	Unit
3.65	C	17.76	$\pm$	11.11	$\pm$	0.00	10^{-4}
	D	13.19	$\pm$	17.25	$\pm$	0.00	10^{-4}
	Average	16.42	$\pm$	9.34	$\pm$	0.00	10^{-4}
4.42	A	-9.97	$\pm$	8.50	$\pm$	0.00	10^{-4}
4.91	A	6.89	$\pm$	5.82	$\pm$	0.00	10^{-4}
5.21	D	-7.72	$\pm$	3.23	$\pm$	0.00	10^{-4}
5.81	A	4.22	$\pm$	9.65	$\pm$	0.00	10^{-4}
6.25	B	-20.87	$\pm$	17.38	$\pm$	0.00	10^{-4}
	C	-31.69	$\pm$	15.46	$\pm$	0.00	10^{-4}
	Average	-26.91	$\pm$	11.55	$\pm$	0.00	10^{-4}

Target Polarized Minus Target Unpolarized							
E_n (MeV)	Set	$\bar{\varepsilon}/\bar{\varepsilon}_{ppol}$	$\pm$	Δ_{stat}	$\pm$	Δ_{sys}	Unit
3.65	C	-141.64	$\pm$	16.55	$\pm$	0.00	10^{-4}
	D	-138.44	$\pm$	31.74	$\pm$	0.00	10^{-4}
4.42	A	-17.02	$\pm$	13.09	$\pm$	0.00	10^{-4}
4.91	A	-10.00	$\pm$	8.18	$\pm$	0.00	10^{-4}
5.21	D	7.66	$\pm$	4.66	$\pm$	0.00	10^{-4}
5.81	A	12.73	$\pm$	14.36	$\pm$	0.00	10^{-4}
6.25	B	67.69	$\pm$	38.32	$\pm$	0.00	10^{-4}
	C	58.15	$\pm$	18.59	$\pm$	0.00	10^{-4}

Table 5.4: Neutron-Transmission Asymmetries Normalized to the Proton Polarimeter Asymmetry

Target Polarized							
E_n (MeV)	Set	$(\bar{\varepsilon}/\bar{P}_p)_c$	$\pm$	Δ_{stat}	$\pm$	Δ_{sys}	Unit
1.94	A	237.88	$\pm$	5.99	$\pm$	6.30	10^{-4}
1.94	B	172.41	$\pm$	7.90	$\pm$	9.31	10^{-4}
1.94	C	256.30	$\pm$	9.97	$\pm$	11.50	10^{-4}
1.94	D_1	176.61	$\pm$	7.28	$\pm$	7.86	10^{-4}
	D_2	252.54	$\pm$	24.35	$\pm$	2.79	10^{-4}
	Average	182.84	$\pm$	6.98	$\pm$	7.44	10^{-4}

Target Unpolarized							
E_n (MeV)	Set	$(\bar{\varepsilon}/\bar{P}_p)_w$	$\pm$	Δ_{stat}	$\pm$	Δ_{sys}	Unit
1.94	A	-10.79	$\pm$	7.67	$\pm$	0.47	10^{-4}
	C	-30.48	$\pm$	10.11	$\pm$	1.66	10^{-4}
	D	-6.72	$\pm$	7.11	$\pm$	0.30	10^{-4}
	Average	-13.20	$\pm$	4.63	$\pm$	0.65	10^{-4}

Target Polarized Minus Target Unpolarized							
E_n (MeV)	Set	$\bar{\varepsilon}/\bar{P}_p$	$\pm$	Δ_{stat}	$\pm$	Δ_{sys}	Unit
1.94	A	251.08	$\pm$	9.73	$\pm$	6.33	10^{-4}
1.94	B	185.61	$\pm$	9.16	$\pm$	9.33	10^{-4}
1.94	C	269.50	$\pm$	10.99	$\pm$	11.52	10^{-4}
1.94	D	196.04	$\pm$	8.38	$\pm$	7.47	10^{-4}

Table 5.5: Neutron-Transmission Asymmetries Normalized to the Proton Beam Polarization

E_n (MeV)	Set	ξ	$\pm$	$\Delta_{stat}\,\xi$	$\pm$	$\Delta_{sys}\,\xi$	Unit
3.65	C	-52.56	$\pm$	6.50	$\pm$	2.25	10^{-2}
	D	-70.62	$\pm$	16.48	$\pm$	2.69	10^{-2}
	Average	-54.99	$\pm$	6.05	$\pm$	2.31	10^{-2}
4.42	A	-6.78	$\pm$	5.22	$\pm$	0.17	10^{-2}
4.91	A	-3.98	$\pm$	3.26	$\pm$	0.10	10^{-2}
5.21	D	3.91	$\pm$	2.39	$\pm$	0.15	10^{-2}
5.81	A	5.07	$\pm$	5.72	$\pm$	0.13	10^{-2}
6.25	B	36.47	$\pm$	20.73	$\pm$	1.83	10^{-2}
	C	21.58	$\pm$	6.96	$\pm$	0.92	10^{-2}
	Average	23.09	$\pm$	6.60	$\pm$	1.01	10^{-2}

Table 5.6: Neutron-Transmission Asymmetries Normalized to Beam and Target Polarizations

Model	$\Delta\sigma_T(E_0)$ (mb)
Full Bonn	899.8
Bonn A	958.5
Bonn B	959.2
Bonn C	964.0
Arndt SM92 Analysis	879.2
Effective Range Parameters	972.7
Average	938.9 $\pm$ 39.1

Table 5.7: Calculated Values of $\Delta\sigma_T$ at a Neutron Energy of 1.94 MeV

E_n (MeV)	$\Delta\sigma_T$ (mb)	$\pm$	Δ_{stat}	$\pm$	Δ_{sys}	Δ
3.65	260.2	$\pm$	28.6	$\pm$	29.1	40.8
4.42	45.9	$\pm$	35.3	$\pm$	4.8	35.6
4.91	42.1	$\pm$	34.5	$\pm$	3.9	34.7
5.21	-39.3	$\pm$	24.1	$\pm$	3.9	24.4
5.81	-26.5	$\pm$	29.9	$\pm$	3.0	30.1
6.25	-67.8	$\pm$	19.4	$\pm$	7.6	20.8

Table 5.8: Measured Values of $\Delta\sigma_T$

5.1.4 Determination of the Zero-Crossing Energy of $\Delta\sigma_T$

In order to determine the zero-crossing energy, a continuous function must be fit to the $\Delta\sigma_T$ data. For this purpose, the prediction of the Bonn potential is used with the transformation

$$E \rightarrow a + bE. \tag{5.30}$$

The coefficients a and b are allowed to vary to find the smallest total chi-square.

$$\chi^2 = \sum_i \left[\frac{\Delta\sigma_T^i(E) - \Delta\sigma_T^{Bonn}(a+bE)}{\Delta(\Delta\sigma_T^i)(E)} \right]^2 \tag{5.31}$$

The uncertainties used are the total uncertainties of Table 5.8. The best fit is obtained with $a = -0.800$ MeV, $b = 1.127$, resulting in a total chi-square of $\chi^2 = 3.98$ and a reduced chi-square of $\chi^2_\nu = 0.995$. The data and fit are shown in Figure 5.2. The zero-crossing energy obtained from the fit is

$$E_{zc} = 5.08 \pm 0.10 \text{ MeV}.$$

The errors on the zero-crossing energy are obtained by shifting a by an amount sufficient to increase χ^2 by 1.0. The zero-crossing energy determined by the shifted fit gives the one-sigma bound on E_{zc}. A simple phase-shift analysis has been performed, allowing only the ϵ_1 mixing parameter to vary[4] in order to reproduce E_{zc}. The result obtained from the analysis is

$$\epsilon_1 = 0.30 \pm 0.17^\circ.$$

These results will be discussed further in Chapter 6.

5.2 $K_y^{y'}$ Measurements for the ^{3}H($\vec{p}$,$\vec{n}$)^{3}He Reaction

Since the determination of $\Delta\sigma_T$ depends upon the polarization-transfer coefficients, $K_y^{y'}$, for the ^{3}H($\vec{p}$,$\vec{n}$)^{3}He neutron source reaction, it is important to know these parameters well. In particular, it is essential to know the polarization transfer at the calibration energy, E_0. Existing data only extends down to a neutron energy of

[4] All phase-shift parameters except ϵ_1 are obtained from the full Bonn potential.

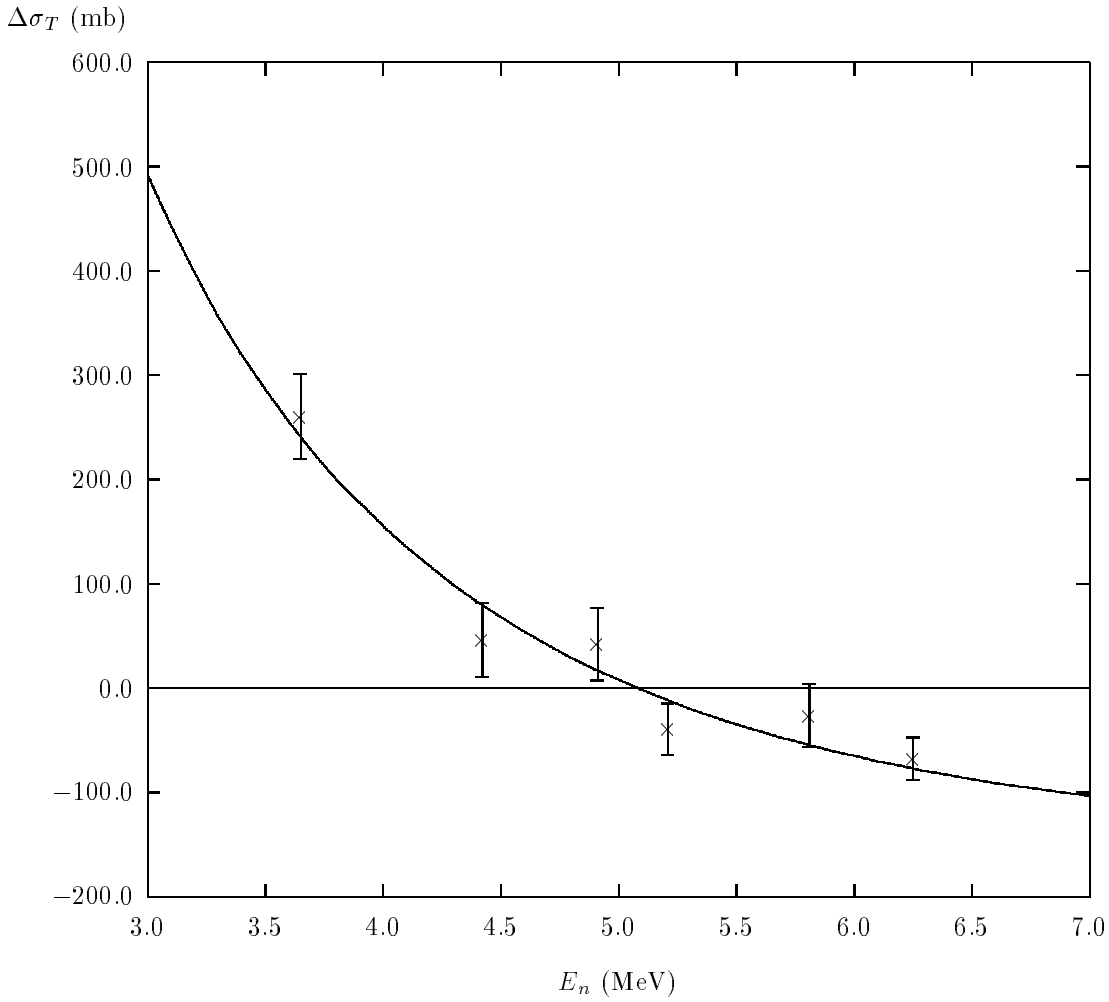

Figure 5.2: $\Delta\sigma_T$ Data with Fit

	Forward Angle				Backward Angle			
E_n (MeV)	N_{L+}	N_{L-}	N_{R+}	N_{R-}	N_{L+}	N_{L-}	N_{R+}	N_{R-}
1.94	—	—	—	—	1316	2192	1757	1117
5.21	1133	676	632	1006	204	422	353	197
5.81	198	361	303	157	81	29	41	107

Table 5.9: Neutron Counts in the Neutron Polarimeter Detectors

2.12 MeV, requiring an extrapolation to $E_0 = 1.94$ MeV. In addition, it is useful to confirm the earlier data in the region of the $\Delta\sigma_T$ zero-crossing. For these reasons, $K_y^{y'}$ has been measured at neutron energies of 1.94, 5.21, and 5.81 MeV. The new data is combined with the existing data to predict the polarization transfer at all energies at which $\Delta\sigma_T$ measurements are made.

5.2.1 Determination of $K_y^{y'}$

The neutron polarimeter asymmetry is calculated for each pair of detectors by forming the asymmetry for the two detectors as defined in Section 4.2.

$$\bar{\varepsilon}_{npol} = \frac{\sqrt{\frac{N_{L+}}{N_{L-}}\frac{N_{R-}}{N_{R+}}} - 1}{\sqrt{\frac{N_{L+}}{N_{L-}}\frac{N_{R-}}{N_{R+}}} + 1} \tag{5.32}$$

$$\Delta\bar{\varepsilon}_{npol} = \frac{\sqrt{N_{L+}N_{R-}(N_{L-}+N_{R+}) + N_{L-}N_{R+}(N_{L+}+N_{R-})}}{\left(\sqrt{N_{L+}N_{R-}} + \sqrt{N_{L-}N_{R+}}\right)^2} \tag{5.33}$$

N_L and N_R refer to the number of counts in the left and right detectors respectively. The subscripts "+" and "−" refer to the spin-state of the beam. This method of averaging reduces the sensitivity of the asymmetry to beam misalignments and detector efficiency differences. In addition, since two detectors are used, it is not necessary to know the incident neutron flux. Table 5.9 lists the total number of counts in each detector and spin-state combination summed over all runs. The average neutron polarizations can be calculated from the average asymmetries using

$$\bar{P}_n = \frac{\bar{\varepsilon}_{npol}}{A_y(^4\mathrm{He})}, \tag{5.34}$$

E_n (MeV)	θ	$\bar{\varepsilon}_{npol}$	$\pm$	$\Delta\bar{\varepsilon}_{npol}$	$\bar{P}_n$	$\pm$	$\Delta_{stat}\bar{P}_n$	$\pm$	$\Delta_{sys}\bar{P}_n$
1.94	107°	−0.2362	$\pm$	0.0122	−0.309	$\pm$	0.016	$\pm$	0.004
5.21	50°	0.2405	$\pm$	0.0166	−0.382	$\pm$	0.026	$\pm$	0.006
	121°	−0.3163	$\pm$	0.0277	−0.344	$\pm$	0.030	$\pm$	0.006
	Average				−0.366	$\pm$	0.020	$\pm$	0.006
5.81	51°	−0.3045	$\pm$	0.0300	0.482	$\pm$	0.048	$\pm$	0.008
	121°	0.4594	$\pm$	0.0560	0.502	$\pm$	0.061	$\pm$	0.008
	Average				0.490	$\pm$	0.038	$\pm$	0.008

Table 5.10: Average Neutron Beam Polarizations

E_n (MeV)	E_p (MeV)	$\bar{\varepsilon}_{ppol}$	$\bar{P}_p$	$\pm$	$\Delta\bar{P}_p$
1.94	6.18	0.401	−0.471	$\pm$	0.005
5.21	6.18	0.395	−0.464	$\pm$	0.005
5.81	6.77	−0.316	0.608	$\pm$	0.011

Table 5.11: Average Proton Beam Polarizations

where the ^{4}He(n,n)^{4}He effective analyzing powers, $A_y(^4\text{He})$, are obtained from Table 3.7. The uncertainties in the analyzing powers are treated as systematic uncertainties. The results for each angle pair at each energy as well as the weighted averages over both angles are listed in Table 5.10.

The average proton polarimeter asymmetries are obtained by taking the difference between the spin *up* and spin *down* asymmetries as in Equation 5.20 and averaging over all runs. The average proton polarization is given by

$$\bar{P}_p = \frac{\bar{\varepsilon}_{pol}}{A_y(^{12}\text{C})}, \tag{5.35}$$

where the ^{12}C(p,p$_0$)^{12}C analyzing powers, $A_y(^{12}\text{C})$, are obtained from Table 5.2. Again, the uncertainties in the analyzing powers are treated as systematic uncertainties. As in the $\Delta\sigma_T$ measurements, the proton beam polarization for the E_n = 1.94 MeV measurement is obtained at a higher energy. Table 5.11 lists the average proton polarizations at each energy.

Once the neutron and proton beam polarizations are known, the polarization-

E_n (MeV)	$K_y^{y'}$	$\pm$	$\Delta_{stat} K_y^{y'}$	$\pm$	$\Delta_{sys} K_y^{y'}$	$\Delta K_y^{y'}$
1.94	0.656	$\pm$	0.034	$\pm$	0.011	0.036
5.21	0.789	$\pm$	0.043	$\pm$	0.015	0.046
5.81	0.806	$\pm$	0.063	$\pm$	0.020	0.066

Table 5.12: Measured Values of the ^{3}H($\vec{\text{p}}$,$\vec{\text{n}}$)^{3}He Polarization-Transfer Coefficient

transfer coefficient is simply the ratio of the two.

$$K_y^{y'} = \frac{\bar{P}_n}{\bar{P}_p} \tag{5.36}$$

Table 5.12 lists the values of $K_y^{y'}$ obtained, as well as statistical and systematic uncertainties. The total uncertainty, $\Delta K_y^{y'}$, is given by

$$\Delta K_y^{y'} = \sqrt{(\Delta_{stat} K_y^{y'})^2 + (\Delta_{sys} K_y^{y'})^2}. \tag{5.37}$$

5.2.2 Interpolation of $K_y^{y'}$ Data

The present $K_y^{y'}$ measurements are combined with data from an earlier experiment at Los Alamos National Laboratory (LANL) [Don71, Hai72] in order estimate the values at the energies of interest. These data are listed in Table 5.13 and plotted in Figure 5.3. The value of $K_y^{y'}$ is estimated at other energies by linear interpolation between the two nearest measurements. The uncertainty is estimated by a linear interpolation of the variances. Estimates of $K_y^{y'}$ are made by this method at the neutron energies used in the $\Delta\sigma_T$ measurements. These values are listed in Table 5.14.

E_n (MeV)	$K_y^{y'}$	$\pm$	$\Delta K_y^{y'}$	Source
1.94	0.656	$\pm$	0.036	TUNL
2.12	0.632	$\pm$	0.048	LANL
3.12	0.661	$\pm$	0.033	LANL
4.15	0.719	$\pm$	0.052	LANL
4.66	0.681	$\pm$	0.031	LANL
5.16	0.724	$\pm$	0.036	LANL
5.21	0.789	$\pm$	0.046	TUNL
5.67	0.788	$\pm$	0.037	LANL
5.81	0.806	$\pm$	0.066	TUNL
6.17	0.828	$\pm$	0.045	LANL
6.67	0.808	$\pm$	0.040	LANL
7.17	0.789	$\pm$	0.047	LANL
7.68	0.769	$\pm$	0.048	LANL
8.18	0.785	$\pm$	0.043	LANL
9.18	0.670	$\pm$	0.050	LANL
10.19	0.681	$\pm$	0.048	LANL
11.18	0.567	$\pm$	0.043	LANL
12.18	0.551	$\pm$	0.056	LANL
13.18	0.444	$\pm$	0.046	LANL
14.19	0.509	$\pm$	0.039	LANL
15.19	0.393	$\pm$	0.036	LANL

Table 5.13: $^3H(\vec{p},\vec{n})^3He$ Polarization-Transfer Coefficient Data Measured at LANL and TUNL

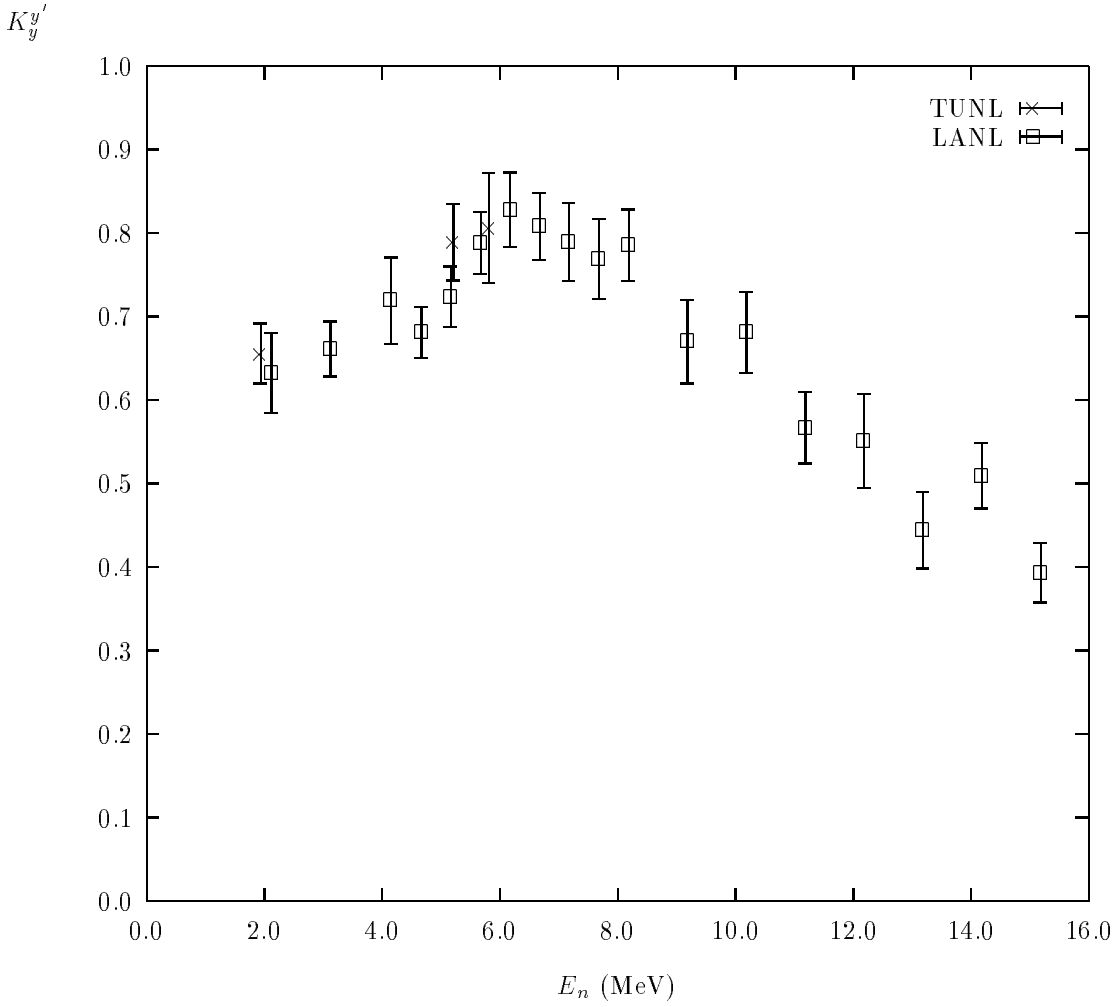

Figure 5.3: ^{3}H($\vec{p}$,$\vec{n}$)^{3}He Polarization-Transfer Coefficient Data Measured at LANL and TUNL

E_n (MeV)	$K_y^{y'}$	$\pm$	$\Delta K_y^{y'}$
1.94	0.656	$\pm$	0.036
3.65	0.691	$\pm$	0.044
4.42	0.699	$\pm$	0.042
4.91	0.703	$\pm$	0.034
5.21	0.789	$\pm$	0.046
5.81	0.806	$\pm$	0.066
6.25	0.825	$\pm$	0.044

Table 5.14: Interpolated Values of the $^3H(\vec{p},\vec{n})^3He$ Polarization-Transfer Coefficient

Chapter 6

Comparison of Data with Potential Models

The measured values of $\Delta\sigma_T$ in Table 5.8 can now be compared with potential-model predictions. Figure 6.1 shows the measured values of $\Delta\sigma_T$ along with the fit obtained in Section 5.1.4, the phase-shift analysis SM92 of Arndt, and the predictions of several potential models. The best agreement is obtained with the Bonn potentials, which have a relatively weak tensor force. The region of the zero-crossing is expanded in Figure 6.2 to compare the fit to the potential models. In this plot, the error bars indicate the uncertainty in the zero-crossing energy. The value of the ϵ_1 phase-shift parameter obtained by performing a simple phase-shift analysis at the zero-crossing energy (Section 5.1.4) is plotted in Figure 6.3. Also included in this plot are the values from potential models and the Arndt SM92 phase-shift analysis. Results obtained from recent experiments sensitive to ϵ_1 are also shown [Ock91b, Ock91a, Sch88]. The Bonn results are from measurements of the neutron-proton polarization transfer coefficient, $K_y^{y'}$.[1] The Erlangen/Tübingen result is from a measurement of the neutron-proton spin-correlation parameter, $A_{yy}(\theta)$, at $\theta_{cm} = 90°$

[1] A value of ϵ_1 was not reported for the Bonn measurement at 17.4 MeV. Instead, a phase-shift analysis similar to the one for the TUNL data was performed by W. Tornow to obtain the plotted value [Tor92].

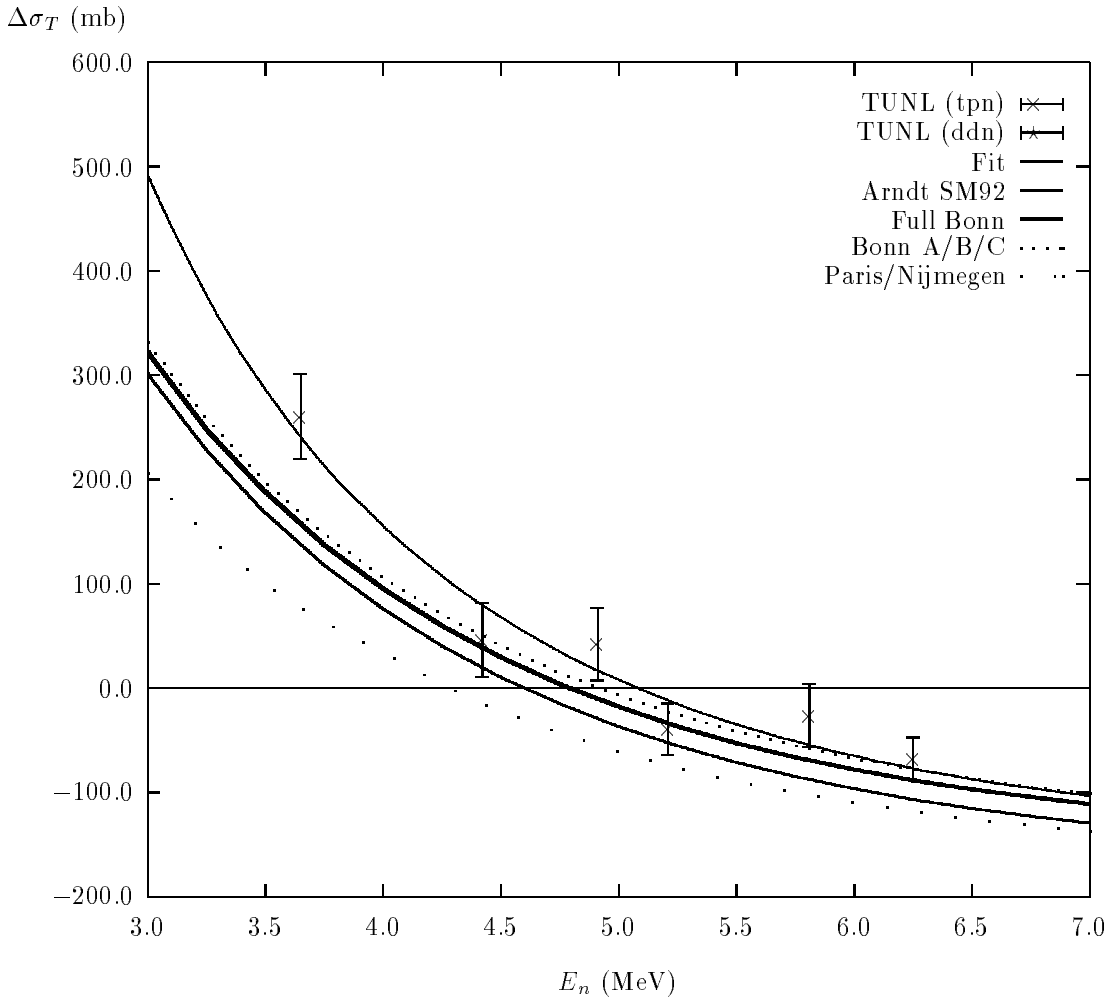

Figure 6.1: Comparison of $\Delta\sigma_T$ Measurements with Potential-Model Predictions

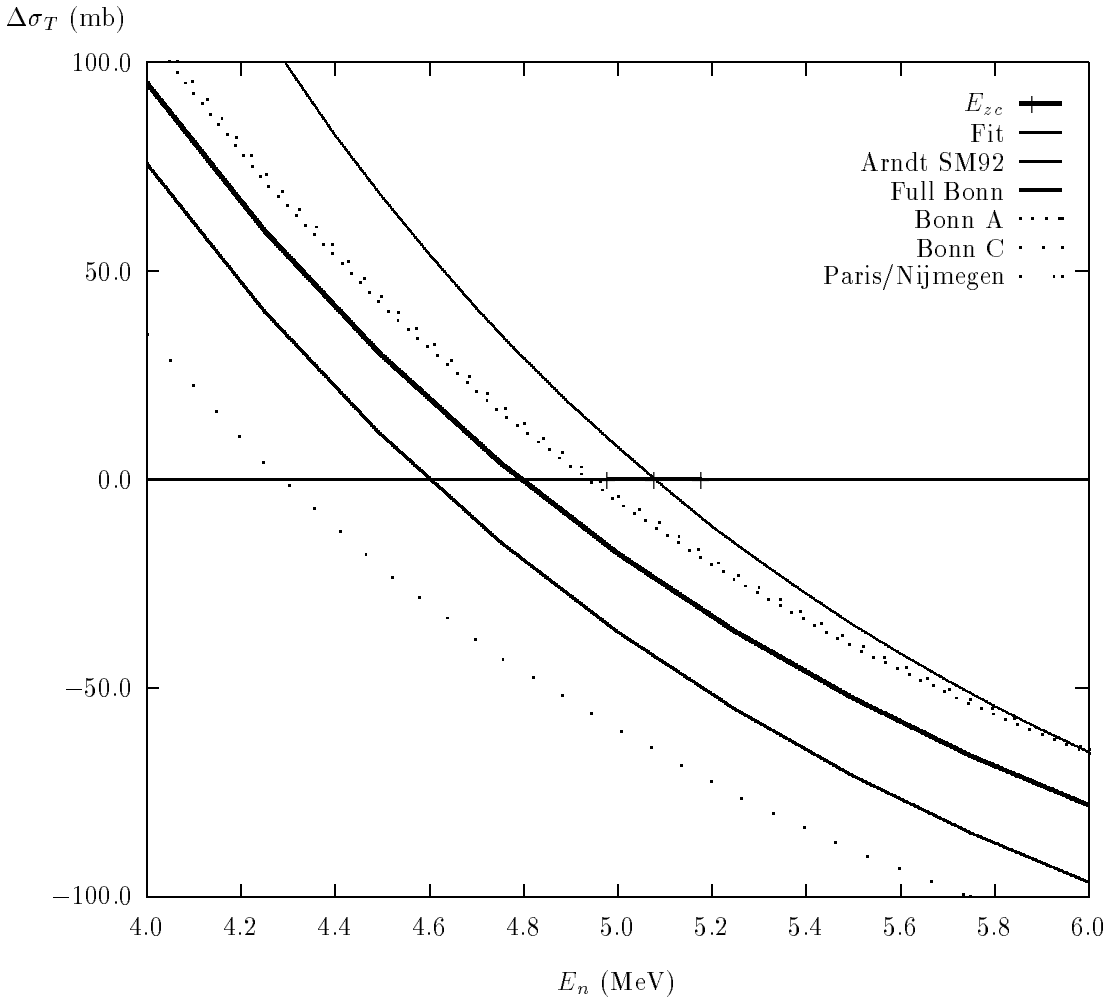

Figure 6.2: Comparison of the Measured Zero-Crossing of $\Delta\sigma_T$ with Potential-Model Predictions

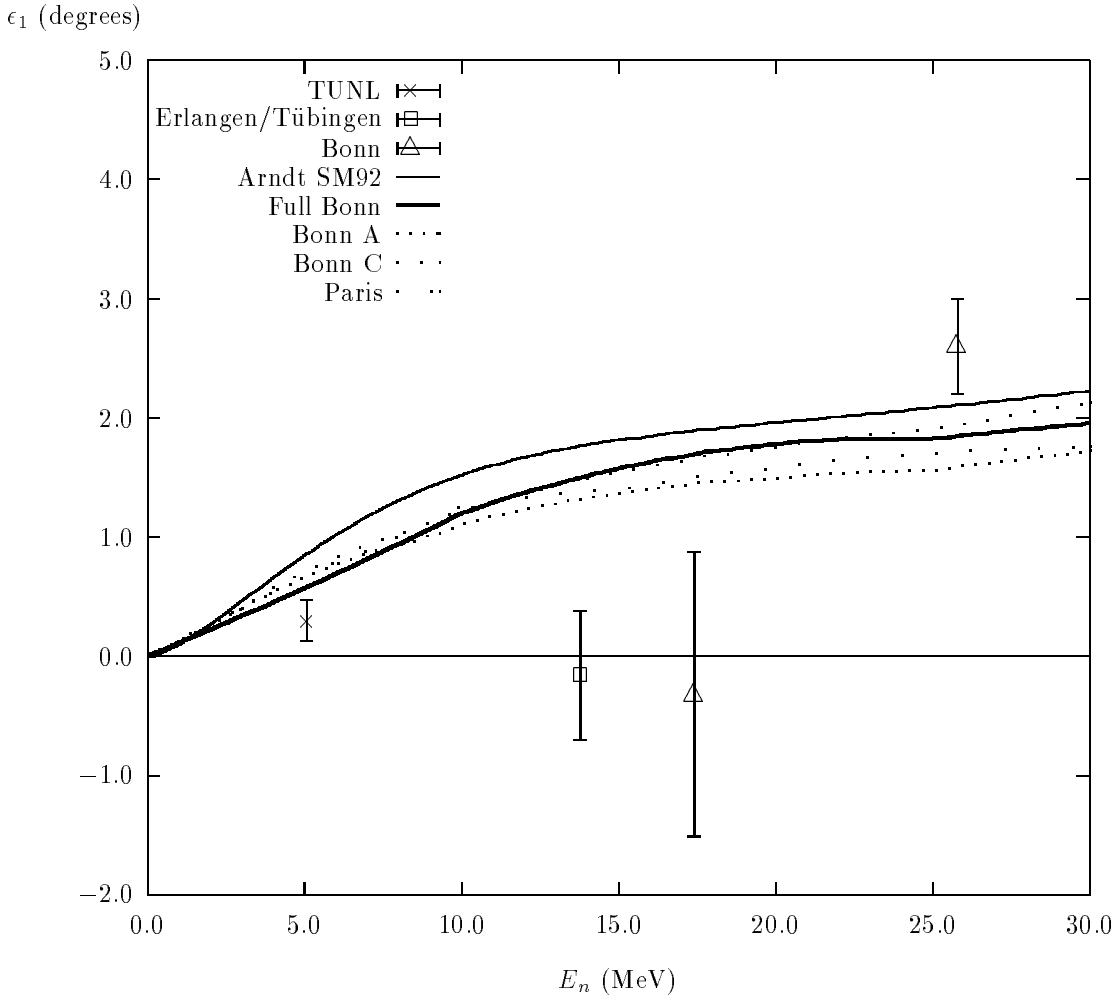

Figure 6.3: Comparison of ϵ_1 Obtained from $\Delta\sigma_T$ Measurements with Potential-Model Parameters

Chapter 7

Conclusions and Summary

Measurements of the spin-dependent difference in total cross section, $\Delta\sigma_T$ for the scattering of polarized neutrons from polarized protons have been made at six energies from 3.65 to 6.25 MeV. $\Delta\sigma_T$ crosses through zero in this energy range, and a zero-crossing energy has been extracted from the data:

$$E_{zc} = 5.08 \pm 0.10 \text{ MeV}.$$

Since a zero-crossing measurement is unaffected by most systematic errors, the uncertainty is due almost entirely to counting statistics. A phase-shift analysis has been performed at the zero-crossing energy in which the mixing parameter ϵ_1 is allowed to vary, while the other parameters are fixed to the full Bonn potential values. The result of this analysis is

$$\epsilon_1 = 0.30 \pm 0.17°.$$

A complete phase-shift analysis allowing all phase-shift parameters to vary and including all relevant data will be performed at a later date in collaboration with R. A. Arndt at Virginia Polytechnic Institute and State University. However, no significant changes are expected from such an analysis. The present result suggests that the tensor force is relatively weak in this energy range. Comparison of the data with potential models shows agreement with potentials such as Bonn A which has a weak tensor force and comes the closest to predicting the correct triton binding energy. The result is also consistent with recent theoretical work suggesting that three-body forces and relativistic effects are not significant in the binding of the triton [Pic92, Sam92],

leaving a weak tensor force as the most likely solution of the triton binding energy problem. It is important to extend the present measurements to higher energies in order to verify these conclusions.

Because of their importance in the analysis of the $\Delta\sigma_T$ data, polarization-transfer coefficients, $K_y^{y'}$, have been measured for the ^{3}H($\vec{p}$,$\vec{n}$)^{3}He reaction at three energies using a neutron polarimeter. The results are in agreement with earlier measurements made at Los Alamos National Laboratory.

Appendix A

Calculation of Neutron Depolarization Due to Magnetic Fields

A beam of neutrons passing through a magnetic field has the spins of the neutrons precessed about the field component transverse to the spin direction. Since the beam has a non-zero spatial extent, the trajectories of the particles are not identical. Thus, particles with different trajectories traverse different magnetic fields and experience differing spin precessions. This process results in an effective depolarization of the beam which must be calculated by Monte Carlo techniques. The FORTRAN code NEUTRONS has been developed to calculate the spin precessions of a beam of neutrons passing through an arbitrary magnetic field. The program is based on the computer code SPINX [Bow91].

The program represents the wavefunctions of the neutrons as two-component Dirac spinors (the lower two components are neglected).

$$\Psi = \begin{pmatrix} \Psi_1 \\ \Psi_2 \end{pmatrix} \tag{A.1}$$

The precession is then represented by a 2×2 rotation matrix, $\mathbf{T}$, which gives the relationship between the initial and final wavefunctions.

$$\Psi_f = \mathbf{T}\Psi_i \tag{A.2}$$

The precession is calculated as a product of small precessions which can be treated as infinitesimal.

$$\mathbf{T} = \mathbf{T}_N\mathbf{T}_{N-1}\mathbf{T}_{N-2}\ldots\mathbf{T}_3\mathbf{T}_2\mathbf{T}_1, \tag{A.3}$$

$$\mathbf{T}_n = \mathbf{I}\cos\left(\frac{\theta}{2}\right) + i\sin\left(\frac{\theta}{2}\right)\left(\boldsymbol{\sigma}\cdot\hat{\boldsymbol{B}}\right), \tag{A.4}$$

where $\mathbf{I}$ is the 2×2 identity matrix, θ is the angle of precession, $\hat{\boldsymbol{B}}$ is a unit vector in the direction of the magnetic field, and $\boldsymbol{\sigma}$ is the Pauli spin vector

$$\boldsymbol{\sigma} = \sigma_x\hat{\boldsymbol{x}} + \sigma_y\hat{\boldsymbol{y}} + \sigma_z\hat{\boldsymbol{z}}. \tag{A.5}$$

The Pauli spin matrices are defined as

$$\sigma_x = \begin{pmatrix} 0 & 1 \\ 1 & 0 \end{pmatrix}, \tag{A.6}$$

$$\sigma_y = \begin{pmatrix} 0 & -i \\ i & 0 \end{pmatrix}, \tag{A.7}$$

$$\sigma_z = \begin{pmatrix} 1 & 0 \\ 0 & -1 \end{pmatrix}. \tag{A.8}$$

The spin precession angle for an infinitesimal rotation, θ, is given by

$$\theta = \frac{\Omega dB}{\sqrt{E}}, \tag{A.9}$$

where d is the distance travelled, B is the magnitude of the magnetic field, E is the energy of the neutron and $\Omega = -1.325 \times 10^{-5}$ $(\mathrm{MeV})^{\frac{1}{2}}/(\mathrm{G{\cdot}cm})$ is a constant. The step size is made small enough such that the difference between calculating the rotation matrix in one step, $\mathbf{T}_n$, and in two half-steps, $\mathbf{T}_n^L$ and $\mathbf{T}_n^U$, is less than a specified amount, ϵ, for each component.

$$\left| T_{ij} - \sum_{k=1}^{2} T_{ik}^U T_{kj}^L \right| \leq \epsilon, \quad (i = 1,2;\ j = 1,2) \tag{A.10}$$

The initial wavefunction is calculated from the angles θ_i and ϕ_i from the input file which give the initial spin direction according to the Madison convention (Section 3.1.3).

$$\Psi_{1i} = \cos\left(\frac{\theta}{2}\right)\cos\left(\frac{\phi}{2}\right) - i\cos\left(\frac{\theta}{2}\right)\sin\left(\frac{\phi}{2}\right) \tag{A.11}$$

$$\Psi_{2i} = \sin\left(\frac{\theta}{2}\right)\cos\left(\frac{\phi}{2}\right) + i\sin\left(\frac{\theta}{2}\right)\sin\left(\frac{\phi}{2}\right) \tag{A.12}$$

Trajectories are chosen by picking a point at random within the initial rectangular beam spot, and picking a direction from a cosine distribution, with the constraint that the trajectory ends inside the final beam spot. The dimensions of the rectangular initial and final beam spots are specified in the input file.

Spin projections are calculated for the final wavefunction along each cartesian axis, and along an axis specified in the input file. The spin projection along an axis specified by a unit vector, $\hat{\boldsymbol{n}}$, is given by

$$\langle P(\hat{\boldsymbol{n}})\rangle = \langle \Psi_f \mid P(\hat{\boldsymbol{n}}) \mid \Psi_f \rangle\,, \tag{A.13}$$

$$P(\hat{\boldsymbol{n}}) = \left|\frac{\mathbf{I} + (\boldsymbol{\sigma}\cdot\hat{\boldsymbol{n}})}{2}\right|. \tag{A.14}$$

The spin projections are averaged over all trajectories and standard deviations are calculated. The angles θ_f and ϕ_f which give the final spin direction are also calculated.

The magnetic field used by NEUTRONS is calculated in a separate program on a three-dimensional grid. The components B_x, B_y, and B_z are calculated at each point. For this experiment, the magnetic field of the superconducting solenoid has been calculated by summing over all windings. The field of one winding can be calculated from the vector potential of a current loop in cylindrical coordinates [Jac75]

$$A_\phi = \frac{4Ia}{c\sqrt{(a+\rho)^2+z^2}}\left[\frac{(2-k^2)K(k)-2E(k)}{k^2}\right], \tag{A.15}$$

$$k^2 = \frac{4a\rho}{(a+\rho)^2+z^2},$$

where a is the radius of the winding, I is the current, c is the speed of light in vacuum, and $K(k)$ and $E(k)$ are elliptic integrals. The solution is given as a series and is in

cgs units.

$$B_\rho = \frac{4\pi I a z}{c[(a+\rho)^2+z^2]^{3/2}} \sum_{n=0}^{\infty} \frac{n(2n+1)}{n+1} \left[\frac{(2n-1)!!}{2^n n!}\right]^2 k^{2n} \tag{A.16}$$

$$B_z = \frac{2\pi I a^2}{c[(a+\rho)^2+z^2]^{3/2}} \sum_{n=0}^{\infty} (2n+1) \left(1 - \frac{n}{n+1}\frac{\rho}{a}\right) \left[\frac{(2n-1)!!}{2^n n!}\right]^2 k^{2n} \tag{A.17}$$

```
      PROGRAM NEUTRONS
C
C         Written 1/8/91 by W. Scott Wilburn, TUNL
C         Based on the FORTRAN program SPINX by J. D. Bowman, LANL
C
C         ***********************************************************
C         This program uses three files which must be assigned to
C         FORTRAN units before execution.  The input file is assigned
C         to FOR001. The format of this file can be obtained from
C         reading the comments about the input parameters given
C         below.  The output file is assigned to FOR002 and is
C         created by this program.  The B field array file is
C         assigned to FOR003.  Note that the size of the array
C         declared as BFIELD below must match that of the array
C         stored in this file.
C         ***********************************************************
C
C         This program performs a Monte Carlo simulation of the
C         precession of the spins of a neutron beam as it passes
C         through a magnetic field.  It differs from the program
C         SPINPROP.FOR in that it obtains the B field at each step
C         from an array previously generated by BFIELD.FOR instead of
C         calculating the values as they are needed.  Random
C         trajectories are chosen to begin within a specified
C         rectangular area in the x-y plane and an initial z position
C         and to end within another rectangular area in the x-y plane
C         at a final z position.  The initial position is chosen with
C         equal probability within the specified plane, and the
C         direction of travel is chosen with a cosine probability
C         distribution such that a trajectory parallel to the z axis
C         is most probable.  The initial-two component spinor wave
C         function is calculated from the initial values of the
C         angles theta and phi given.  Each neutron is transported
```

```
C          along its chosen trajectory in small enough steps that the
C          spin precession can be treated as an infinitesimal
C          rotation.  A rotation matrix is generated for each step and
C          the product of all the rotation  matrices (for one neutron)
C          is computed along the way.  At the end of the trajectory, a
C          rotation matrix representing the entire precession has been
C          generated.  The step size is determined with a convergence
C          criteria which compares the result of taking a whole step
C          with that of taking two half steps.  If the components of
C          the rotation matrix from the two step sizes differ by more
C          than a specified amount, the step size is cut in half and
C          we try again.  At the end of each trajectory, the final
C          spinor wavefunction is calculated by operating on the
C          initial wavefunction with the rotation operator.  Spin
C          projection expectation values are calculated along the x,
C          y, and z axes and along the target spin direction and
C          written to output.  Also, the sums of spin projections and
C          squares of sums for all neutrons are kept up with so that
C          the statistical mean and standard deviation can be
C          calculated.  Finally, the mean spin projections are used to
C          calculate the mean theta and phi spin angles with standard
C          deviations.
C
C          Input Variables (read from FOR001):
C
C             E       Neutron Energy (MeV) (common block DATA)
C             ETA     Magnet Angle (deg converted to rad) (common
C                        block DATA)
C             N       Number of neutrons
C             PHII    Initial azimuthal spin angle (deg conv. to rad)
C             THETAI  Initial polar spin angle (deg conv. to rad)
C             XMAXF   Maximum final x position (cm)
C             XMAXI   Maximum initial x position (cm)
```

```
C            YMAXF   Maximum final y position (cm)
C            YMAXI   Maximum initial y position (cm)
C            ZF      Final z position (cm)
C            ZI      Initial z position (cm)
C
C         Input Variables (read from FOR003):
C
C            BFIELD  Array of B field vectors (G) (common block
C                       FIELD)
C            NBMAX   Dimensions of BFIELD
C            RMAX    Maximum x, y, and z covered by BFIELD (cm)
C            RMIN    Minimum x, y, and z covered by BFIELD (cm)
C                       (common block FIELD)
C
C         Output Variables (written to FOR002):
C
C            PAVE       Mean values of spin projections
C            PDEV       Standard deviations of spin projections
C            PHIF       Mean azimuthal angle of final spin (deg)
C            PHIFDEV    Standard deviation of final phi (deg)
C            RF         Final position (cm)
C            RI         Initial position (cm)
C            THETAF     Mean polar angle of final spin (deg)
C            THETAFDEV  Standard deviation of final theta (deg)
C            P          Spin projections on cartesian axes and
C                          target spin direction
C
C         Internal Variables:
C
C            CVG        Indicates whether convergence has occurred in
C                          calculating rotation matrix
C            D          Step size in fraction of total distance to be
C                          travelled
```

```
C             DELTA_T    Difference in component of rotation matrices
C                           calculated using step D and D/2
C             DR         Magnitude of step (cm)
C             DX         Interval between points in BFIELD (cm)
C                           (common block Field)
C             F          Fraction of total distance travelled
C             GAMMA      Relativistic gamma (common block DATA)
C             J          Counting variable
C             K          Counting variable
C             L          Counting variable
C             M          Counting variable
C             PSIF       Final spinor wavefunction
C             PSII       Initial spinor wavefunction
C             PSQSUM     Sum of squares of spin projections
C             PSUM       Sum of spin projections
C             R          Position vector (cm)
C             R_B        Position vector of B field for full step (cm)
C             RD         Position difference vector, RF-RI (cm)
C             RL_B       Position vector of B field for lower half
C                           step (cm)
C             RU_B       Position vector of B field for upper half
C                           step (cm)
C             S          Spin direction vector
C             SIN_ALPHA  Sine of horizontal trajectory angle
C             SIN_AMAX   Sine of maximum alpha
C             SIN_AMIN   Sine of minimum alpha
C             SIN_BETA   Sine of vertical trajectory angle
C             SIN_BMAX   Sine of maximum beta
C             SIN_BMIN   Sine of minimum beta
C             T          Rotation matrix for a full step
C             TL         Rotation matrix for lower half step
C             TT         Matrix product TU*TL
C             TU         Rotation matrix for upper half step
```

```
C             U          Rotation matrix for entire trajectory
C             W          Unit vector along target spin
C
C          Constants:
C
C             D0      Initial step-size in fraction of total distance
C                        to be moved
C             E0      Neutron rest energy (common block CONSTANTS)
C             EPS     Convergence criteria on rotation matrices for
C                        determining step-size
C             I       Imaginary unit (common block CONSTANTS)
C             PI      Pi (common block CONSTANTS)
C             SEED    Seed for random number generation for choosing
C                        trajectories
C             SI      2x2 identity matrix (common block CONSTANTS)
C             SIGMA   2x2x3 Pauli spin vector (common block CONSTANTS)
C             SX      \
C             SY      } Pauli spin matrices (common block CONSTANTS)
C             SZ      /
C             X       Unit vector along x (common block CONSTANTS)
C             Y       Unit vector along y (common block CONSTANTS)
C             Z       Unit vector along z (common block CONSTANTS)
C
C          ****************************
C          *** Variable Declarations ***
C          ****************************
C
           IMPLICIT NONE
C
           LOGICAL*1   CVG
C
           INTEGER*2   J,K,L,M,N
C
```

```
      INTEGER*4   NBMAX(3),SEED
C
      REAL*4      D,DX(3),D0,DELTA_T,DR,E,E0,EPS,ETA,F,GAMMA
     >            ,PAVE(4),PDEV(4),PHIF,PHIFDEV,R(3),R_B(3),RD(3)
     >            ,RF(3),RI(3),RL_B(3),RMIN(3),RU_B(3),RMAX(3)
     >            ,SIN_ALPHA,SIN_AMAX,SIN_AMIN,SIN_BETA,SIN_BMAX
     >            ,SIN_BMIN,THETAF,THETAFDEV,W(3),X(3),XMAXF
     >            ,XMAXI,Y(3),YMAXF,YMAXI,Z(3),ZF,ZI
C
      REAL*8      BFIELD(11,27,407,3),P(4),PHII,PI,PSQSUM(4)
     >            ,PSUM(4),S(3),THETAI
C
      COMPLEX*8   I,SI(2,2),SIGMA(2,2,3),SX(2,2),SY(2,2),SZ(2,2)
C
      COMPLEX*16  PSIF(2),PSII(2),T(2,2),TL(2,2),TU(2,2),TT(2,2)
     >            ,U(2,2)
C
      EQUIVALENCE (SIGMA(1,1,1),SX),(SIGMA(1,1,2),SY)
     >            ,(SIGMA(1,1,3),SZ)
C
      COMMON /CONSTANTS/   E0,I,PI,SI,SIGMA,X,Y,Z
C
      COMMON /DATA/        E,ETA,GAMMA
C
      COMMON /FIELD/       BFIELD,DX,RMIN
C
      DATA D0     /1.0/
      DATA E0     /939.573/
      DATA EPS    /1.0E-5/
      DATA I      /(0.0,1.0)/
      DATA SEED   /67459873/
      DATA SI     /(1.0,0.0),(0.0,0.0),(0.0,0.0),(1.0,0.0)/
      DATA SX     /(0.0,0.0),(1.0,0.0),(1.0,0.0),(0.0,0.0)/
```

```
      DATA SY     /(0.0,0.0),(0.0,-1.0),(0.0,1.0),(0.0,0.0)/
      DATA SZ     /(1.0,0.0),(0.0,0.0),(0.0,0.0),(-1.0,0.0)/
      DATA X      /1.0,0.0,0.0/
      DATA Y      /0.0,1.0,0.0/
      DATA Z      /0.0,0.0,1.0/
C
C     ********************************
C     *** Preliminary Calculations ***
C     ********************************
C
C     Calculate value of pi
C
      PI=DACOS(-1.0D0)
C
C     Calculate relativistic gamma
C
      GAMMA=1+E/E0
C
C     ******************
C     *** Read Input ***
C     ******************
C
C     Get input parameters:
C
C        ZI       Initial z position of neutrons (cm) (R*4)
C        ZF       Final z position of neutrons (cm) (R*4)
C        XMAXI    Maximum initial x position (cm) (R*4)
C        YMAXI    Maximum initial y position (cm) (R*4)
C        XMAXF    Maximum final x position (cm) (R*4)
C        YMAXF    Maximum final y position (cm) (R*4)
C        N        Number of neutrons to be tracked (I*2)
C        E        Energy of neutrons (MeV) (R*4)
C        THETAI   Initial spin angle theta of neutron (deg) (R*4)
```

```
C             PHII     Initial spin angle phi of neutron (deg) (R*4)
C             ETA      Angle of magnet (deg) (0 is longitudinal) (R*4)
C
C          Open input file
C
           OPEN (UNIT=1,STATUS='OLD',ACCESS='SEQUENTIAL',READONLY)
C
C          Read data
C
           READ (1,*) ZI,ZF
           READ (1,*) XMAXI,YMAXI
           READ (1,*) XMAXF,YMAXF
           READ (1,*) N,E
           READ (1,*) THETAI,PHII
           READ (1,*) ETA
C
C          Close input file
C
           CLOSE (UNIT=1)
C
C          Open output file
C
           OPEN (UNIT=2,STATUS='NEW',ACCESS='SEQUENTIAL')
C
C          Write input data and header for trajectory information to
C          output file
C
           WRITE (2,100) ZI
           WRITE (2,110) ZF
           WRITE (2,120) XMAXI
           WRITE (2,130) YMAXI
           WRITE (2,140) XMAXF
           WRITE (2,150) YMAXF
```

```
            WRITE (2,160) N
            WRITE (2,170) E
            WRITE (2,180) THETAI
            WRITE (2,190) PHII
            WRITE (2,200) ETA
            WRITE (2,210)
C
  100       FORMAT (' Initial z position (cm)            ',F7.2)
  110       FORMAT (' Final z position (cm)              ',F7.2)
  120       FORMAT (' Maximum initial x position (cm)    ',F7.2)
  130       FORMAT (' Maximum initial y position (cm)    ',F7.2)
  140       FORMAT (' Maximum final x position (cm)      ',F7.2)
  150       FORMAT (' Maximum final y position (cm)      ',F7.2)
  160       FORMAT (' Number of neutrons                 ',I7)
  170       FORMAT (' Neutron energy (MeV)                 ',F5.2)
  180       FORMAT (' Initial spin angle theta (degrees)  ',F6.2)
  190       FORMAT (' Initial spin angle phi (degrees)   ',F7.2)
  200       FORMAT (' Magnet angle eta (degrees)         ',F7.2)
  210       FORMAT (/,' NUMBER   Xi      Yi      Xf      Yf      '
     >             ,'Px       Py      Pz      Pt')
C
C           Open file containing B field array
C
            OPEN (UNIT=3,FORM='UNFORMATTED',ACCESS='SEQUENTIAL'
     >           ,STATUS='OLD')
C
C           Read header information
C
            READ (3) NBMAX
            READ (3) RMIN
            READ (3) RMAX
            READ (3)
C
```

```
C          Read B field array
C
           READ (3) BFIELD
C
C          Close file
C
           CLOSE (UNIT=3)
C
C          ********************************
C          *** Preliminary Calculations ***
C          ********************************
C
C          Convert angles from degrees to radians
C
           THETAI=THETAI*PI/180
           PHII=PHII*PI/180
           ETA=ETA*PI/180
C
C          Calculate unit vector along target spin
C
           W(1)=SIN(ETA)
           W(2)=0.0
           W(3)=COS(ETA)
C
C          Calculate interval between points in BFIELD
C
           DO K=1,3
              DX(K)=(RMAX(K)-RMIN(K))/(NBMAX(K)-1)
           END DO
C
C          Calculate initial spin wavefunction, PSII, from initial
C          theta and phi
C
```

```
            PSII(1)=DCOS(THETAI/2)*DCOS(PHII/2)-I*DCOS(THETAI/2)
     >             *DSIN(PHII/2)
            PSII(2)=DSIN(THETAI/2)*DCOS(PHII/2)+I*DSIN(THETAI/2)
     >             *DSIN(PHII/2)
C
C
C
C           Initialize variables.  PSUM are the spin projection
C           expectation values for each axis summed over all
C           trajectories calculated.  PSQSUM are the sums of the
C           squares of these values.  They are used at the end to
C           calculate averages and standard deviations.
C
            DO K=1,3
               PSUM(K)=0.0
               PSQSUM(K)=0.0
            END DO
C
C           ***************************
C           *** Propagate Neutrons ***
C           ***************************
C
C           Calculate N random trajectories, propagate a neutron spin
C           wavefunction along each trajectory, and calculate
C           expectation values of the spin projections on the x, y, and
C           z axes.
C
            DO J=1,N
C
C              ************************
C              *** Choose Trajectory ***
C              ************************
C
```

```
C            Choose a random trajectory for a neutron starting at
C            z=ZI and ending at z=ZF.  Starting x and y values are
C            randomly chosen in the range -XMAXI<=x<=XMAXI and
C            -YMAXI<=y<=YMAXI respectively.  Final x and y values are
C            chosen by picking random trajectories with a cosine
C            probability distribution such that the pass through the
C            region -XMAXF<=x<=XMAXF, and -YMAXF<=y<=YMAXF.  RI and
C            RF are the initial and final vectors so chosen and RD is
C            RF-RI.  Alpha and beta are the angles of the trajectory
C            in the x and y planes respectively.  SIN_AMAX and
C            SIN_AMIN are the sines of maximum and minimum values of
C            alpha which allow the trajectory to pass through the
C            specified region.  SIN_BMAX and SIN_BMIN work the same
C            for beta.  SIN_ALPHA and SIN_BETA are the sines of the
C            randomly chosen values of alpha and beta for this
C            trajectory.
C
             RI(1)=XMAXI*(2*RAN(SEED)-1)
             RI(2)=YMAXI*(2*RAN(SEED)-1)
             RI(3)=ZI
C
             SIN_AMAX=(XMAXF-RI(1))/(ZF-ZI)
             SIN_AMIN=(-XMAXF-RI(1))/(ZF-ZI)
             SIN_BMAX=(YMAXF-RI(2))/(ZF-ZI)
             SIN_BMIN=(-YMAXF-RI(2))/(ZF-ZI)
C
             SIN_ALPHA=(SIN_AMAX-SIN_AMIN)*RAN(SEED)+SIN_AMIN
             SIN_BETA=(SIN_BMAX-SIN_BMIN)*RAN(SEED)+SIN_BMIN
C
             RF(1)=(ZF-ZI)*SIN_ALPHA+RI(1)
             RF(2)=(ZF-ZI)*SIN_BETA+RI(2)
             RF(3)=ZF
C
```

```
            DO K=1,3
               RD(K)=RF(K)-RI(K)
            END DO
C
C           ************************
C           *** Transport Neutron ***
C           ************************
C
C           Transport a neutron spin along the trajectory from RI to
C           RF starting with initial spin wave function PSII. PSIF
C           is the calculated final spin wave function.
C
C           Set initial values of position (R), fraction of
C           trajectory travelled (F), and incremental distance(D).
C
            DO K=1,3
               R(K)=RI(K)
            END DO
C
            D=D0
            F=0.0
C
C           Initialize U, a 2x2 matrix corresponding to the
C           cumulative rotation of the neutron spin
C
            DO K=1,2
               DO L=1,2
                  U(K,L)=SI(K,L)
               END DO
            END DO
C
            DO WHILE (F.LT.1.0)
C
```

```
C               Check to see if we are at the last step and it will
C               take us past the end of the trajectory.  If so,
C               adjust the last step to end at the right point.
C
                IF ((F+D).GT.1.0) THEN
                   D=1-F
                END IF
C
C               Calculate the rotation matrix for a whole step (T)
C               and for the interval taken as two half steps (TL and
C               TU).  If T differs from the product of TL and TU by
C               more than EPS, it is not a good approximation to
C               approximate the step with an infinitesimal rotation,
C               and we cut the step size in half and try again.
C
                DO K=1,3
                   R_B(K)=R(K)+(D/2)*RD(K)
                   RL_B(K)=R(K)+(D/4)*RD(K)
                   RU_B(K)=R(K)+(3*D/4)*RD(K)
                END DO
C
                DR=D*SQRT(RD(1)**2+RD(2)**2+RD(3)**2)
C
                CALL ROT(R_B,DR,T)
                CALL ROT(RL_B,DR/2,TL)
                CALL ROT(RU_B,DR/2,TU)
C
C               Calculate TT and the difference between it and T,
C               DELTA_T
C
                CALL MULT(TL,TU,TT)
C
                CVG=.TRUE.
```

```
C
                DO K=1,2
                   DO L=1,2
                      DELTA_T=ABS(T(K,L)-TT(K,L))
                      IF (DELTA_T.GT.EPS) THEN
                         CVG=.FALSE.
                      END IF
                   END DO
                END DO
C
C               If the convergence criteria is not met, cut the step
C               size in half.  If it is met, increment the fraction
C               of the distance travelled, F, by the step taken, D,
C               multiply the cumulative rotation matrix, U, by the
C               rotation performed in this step, T, and set the step
C               size back to its original value.
C
                IF (CVG.EQ..FALSE.) THEN
                   D=D/2
                ELSE
                   F=F+D
                   DO K=1,3
                      R(K)=R(K)+D*RD(K)
                   END DO
                   CALL MULT(U,T,U)
                   D=D0
                END IF
C
             END DO
C
C            ****************************************
C            *** Calculate Final Spinor Wavefunction ***
C            ****************************************
```

```
C
              DO K=1,2
                 PSIF(K)=(0.0,0.0)
              END DO
C
              DO K=1,2
                 DO L=1,2
                    PSIF(K)=PSIF(K)+U(K,L)*PSII(L)
                 END DO
              END DO
C
C             ****************************
C             *** Calculate Projections ***
C             ****************************
C
C             Calculate spin projection expectation values for at the
C             end of the trajectory and write to output file
C
              CALL PROJ(PSIF,X,P(1))
              CALL PROJ(PSIF,Y,P(2))
              CALL PROJ(PSIF,Z,P(3))
              CALL PROJ(PSIF,W,P(4))
C
              WRITE (2,300) J,RI(1),RI(2),RF(1),RF(2),P
C
  300         FORMAT (2x,I5,4(3x,F5.2),4(2x,F6.4))
C
C             ****************************
C             *** Accumulate Statistics ***
C             ****************************
C
C             Add spin projections to statistical accumulations
C
```

```
               DO K=1,4
                  PSUM(K)=PSUM(K)+P(K)
                  PSQSUM(K)=PSQSUM(K)+P(K)**2
               END DO
C
            END DO
C
C           ************************************
C           *** Calculate Statistical Results ***
C           ************************************
C
C           Calculate averages and and standard deviations for the spin
C           projections.
C
            DO K=1,4
               PAVE(K)=PSUM(K)/FLOAT(N)
               IF (N.NE.1) THEN
                  PDEV(K)=SQRT(ABS((PSQSUM(K)-FLOAT(N)*PAVE(K)**2)
     >                 /FLOAT(N-1)))
               ELSE
                  PDEV(K)=0.0
               END IF
            END DO
C
C           Calculate the average theta and phi for final spin
C           wavefunction, with standard deviations
C
C           Get unit vector for spin direction.
C
            DO K=1,3
               S(K)=2*PAVE(K)-1
            END DO
C
```

```
            THETAF=ACOS(S(3))
            IF (ABS(S(3)).EQ.1.0) THEN
               THETAFDEV=0.0
            ELSE
               THETAFDEV=(2/SQRT(1-S(3)**2))*PDEV(3)
            END IF
C
            IF ((S(1).EQ.0.0).AND.(S(2).EQ.0.0)) THEN
               PHIF=0.0
               PHIFDEV=0.0
            ELSE
               IF (S(2).GE.0.0) THEN
                  PHIF=ACOS(S(1)/SQRT(S(1)**2+S(2)**2))
               ELSE
                  PHIF=2*PI-ACOS(S(1)/SQRT(S(1)**2+S(2)**2))
               END IF
               PHIFDEV=(2/(S(1)**2+S(2)**2))*SQRT(S(2)**2*PDEV(1)**2
     >              +S(1)**2*PDEV(2)**2)
            END IF
C
C           Convert angles from radians to degrees
C
            THETAF=THETAF*180/PI
            THETAFDEV=THETAFDEV*180/PI
            PHIF=PHIF*180/PI
            PHIFDEV=PHIFDEV*180/PI
C
C           ********************
C           *** Write Output ***
C           ********************
C
            WRITE (2,400) PAVE(1),PDEV(1)
            WRITE (2,410) PAVE(2),PDEV(2)
```

```
           WRITE (2,420) PAVE(3),PDEV(3)
           WRITE (2,430) PAVE(4),PDEV(4)
           WRITE (2,440) THETAF,THETAFDEV
           WRITE (2,450) PHIF,PHIFDEV
C
  400      FORMAT (//,' Averages',/,'    PX = ',F6.4,' +/- ',F6.4)
  410      FORMAT ('    PY = ',F6.4,' +/- ',F6.4)
  420      FORMAT ('    PZ = ',F6.4,' +/- ',F6.4)
  430      FORMAT ('    PT = ',F6.4,' +/- ',F6.4,/)
  440      FORMAT (' THETA = ',F6.2,' +/- ',F6.2)
  450      FORMAT ('   PHI = ',F6.2,' +/- ',F6.2,/)
C
        END
C
C
C
        SUBROUTINE MULT(U1,U2,U3)
C
C          Multiplies two spin rotation operators to obtain a third,
C          U3=U2*U1
C
C          Input Variables:
C
C             U1  Rotation operator acting first
C             U2  Rotation operator acting second
C
C          Output Variable:
C
C             U3  Matrix product U2*U1
C
C          Internal Variables:
C
C             K   Counting variable
```

```
C             L   Counting variable
C             M   Counting variable
C             UT  Matrix product U2*U1 (temporary)
C
              IMPLICIT NONE
C
              INTEGER*2   K,L,M
C
              COMPLEX*16  U1(2,2),U2(2,2),U3(2,2),UT(2,2)
C
C             Initialize UT, which will temporarily be the product.  This
C             allows U3 to be the same variable as U1 or U2, if desired.
C
              DO K=1,2
                 DO L=1,2
                    UT(K,L)=(0.0,0.0)
                 END DO
              END DO
C
C             Calculate UT=U2*U1
C
              DO K=1,2
                 DO L=1,2
                    DO M=1,2
                       UT(K,L)=UT(K,L)+U2(K,M)*U1(M,L)
                    END DO
                 END DO
              END DO
C
C             Set U3=UT
C
              DO K=1,2
                 DO L=1,2
```

```
               U3(K,L)=UT(K,L)
            END DO
         END DO
C
         RETURN
      END
C
C
C
      SUBROUTINE ROT(R1,DR1,T1)
C
C        Constructs the approximate rotation operator for an
C        incremental step by assuming it is infinitesimal
C
C        Input Variables:
C
C           DR1  Length of step (cm)
C           R1   Position at which field is to be calculated (cm)
C                  (center of step)
C
C        Output Variable:
C
C           T1  Rotation matrix for step
C
C        Internal Variables:
C
C           B      Magnetic field vector at R1 (G)
C           BMAG   Magnitude of B (G)
C           BUN    Unit normal vector along B
C           FB     Fraction R is away from nearest grid point in
C                     each dimension
C           K      Counting variable
C           L      Counting variable
```

```
C             M      Counting variable
C             P      Counting variable
C             THETA  Angle of rotation (rad)
C
C          Constants:
C
C             BFIELD  Array of B field vectors (G) (common block
C                        FIELD)
C             DX      Interval between points in BFIELD (cm) (common
C                        block FIELD)
C             E       Energy of neutron (MeV) (common block DATA)
C             E0      Neutron rest energy (MeV) (common block
C                        CONSTANTS)
C             ETA     Angle of magnet (rad) (common block DATA)
C             GAMMA   Relativistic gamma (common block DATA)
C             I       Imaginary unit (common block CONSTANTS)
C             NB      Array coordinates of R1 in BFIELD
C             OMEGA   Precession of 1 MeV neutron after travelling 1
C                        cm in 1 G field
C             PI      Pi (common block CONSTANTS)
C             RMIN    Minimum x, y, and z covered by BFIELD (cm)
C                        (common block FIELD)
C             SIGMA   Pauli spin vector (common block CONSTANTS)
C             SI      2x2 identity matrix (common block CONSTANTS)
C             X       Unit vector along x (common block CONSTANTS)
C             Y       Unit vector along y (common block CONSTANTS)
C             Z       Unit vector along z (common block CONSTANTS)
C
              IMPLICIT NONE
C
              INTEGER*2   K,L,M,NB(3),P
C
              REAL*4      DR1,DX(3),E,E0,ETA,FB(3),GAMMA,OMEGA,R1(3)
```

```
     >                ,RMIN(3),X(3),Y(3),Z(3)
C
           REAL*8      B(3),BFIELD(11,27,407,3),BMAG,BUN(3),PI,THETA
C
           COMPLEX*8   I,SI(2,2),SIGMA(2,2,3)
C
           COMPLEX*16  T1(2,2)
C
           COMMON /CONSTANTS/   E0,I,PI,SI,SIGMA,X,Y,Z
           COMMON /DATA/        E,ETA,GAMMA
           COMMON /FIELD/       BFIELD,DX,RMIN
C
           DATA OMEGA  /-1.325E-5/
C
C          Calculate magnetic field vector by interpolating between
C          points in BFIELD array
C
C          Calculate coordinates of R in BFIELD array.  NB(K) are the
C          integer parts while FB(K) is are the fractional parts minus
C          1/2.
C
C          Initialize B.
C
           DO K=1,3
              NB(K)=IINT((R1(K)-RMIN(K))/DX(K))+1
              FB(K)=(R1(K)-RMIN(K))/DX(K)+1.0/2-NB(K)
              B(K)=0.0
           END DO
C
C          Linearly interpolate between nearest 8 points in BFIELD.
C
           DO K=0,1
              DO L=0,1
```

```
                DO M=0,1
                   DO P=1,3
                      B(P)=B(P)+(1.0/2-(-1)**K*FB(1))*(1.0/2-(-1)**L
     >                    *FB(2))*(1.0/2-(-1)**M*FB(3))
     >                    *BFIELD(NB(1)+K,NB(2)+L,NB(3)+M,P)
                   END DO
                END DO
             END DO
          END DO
C
C         Calculate magnitude of B
C
          BMAG=DSQRT(B(1)**2+B(2)**2+B(3)**2)
C
C         Calculate unit vector in direction of B
C
          DO K=1,3
             IF (BMAG.EQ.0.0) THEN
                BUN(K)=0.0
             ELSE
                BUN(K)=B(K)/BMAG
             END IF
          END DO
C
C         Calculate precession of spin during step
C
          THETA=(OMEGA/(GAMMA*SQRT(E)))*DR1*BMAG
C
C         Initialize T1, rotation matrix
C
          DO K=1,2
             DO L=1,2
                T1(K,L)=(0.0,0.0)
```

```
               END DO
            END DO
C
C           Calculate T1=Icos(THETA/2)+isin(THETA/2)(SIGMA*BUN)
C
            DO K=1,2
               DO L=1,2
                  T1(K,L)=T1(K,L)+DCOS(THETA/2)*SI(K,L)
                  DO M=1,3
                     T1(K,L)=T1(K,L)+I*DSIN(THETA/2)*BUN(M)
     >                       *SIGMA(K,L,M)
                  END DO
               END DO
            END DO
C
            RETURN
         END
C
C
C
         SUBROUTINE PROJ (PSI1,N1,P1)
C
C           Calculates the projection of the spin wavefunction PSI1 on
C           the normal vector N1.  P1 is the result
C
C           Input Variables:
C
C              PSI1  Spinor wavefunction
C              N1    Unit vector
C
C           Output Variable:
C
C              P1  Spin projection of PSI1 on N1
```

```
C
C          Internal Variables:
C
C             J    Counting variable
C             K    Counting Variable
C             L    Counting variable
C             PHI  Result of operating on PSI1 with projection
C                     operator
C
C          Constants:
C
C             E0     Neutron rest energy (MeV) (common block
C                       CONSTANTS)
C             I      Imaginary unit (common block CONSTANTS)
C             PI     Pi (common block CONSTANTS)
C             SIGMA  Pauli spin vector (common block CONSTANTS)
C             SI     2x2 identity matrix (common block CONSTANTS)
C             X      Unit vector along x (common block CONSTANTS)
C             Y      Unit vector along y (common block CONSTANTS)
C             Z      Unit vector along z (common block CONSTANTS)
C
          IMPLICIT NONE
C
          INTEGER*2   J,K,L
C
          REAL*4      E0,N1(3),X(3),Y(3),Z(3)
C
          REAL*8      P1,PI
C
          COMPLEX*8   I,SI(2,2),SIGMA(2,2,3)
C
          COMPLEX*16  PHI(2),PSI1(2)
C
```

```
      COMMON /CONSTANTS/  E0,I,PI,SI,SIGMA,X,Y,Z
C
C     Initialize PHI, result of operating on PSI1 with projection
C     operator
C
      PHI(1)=(0.0,0.0)
      PHI(2)=(0.0,0.0)
C
C     Calculate PHI=1/2[I+(SIGMA*N1)]PSI1
C
      DO J=1,2
         DO K=1,2
            PHI(J)=PHI(J)+SI(J,K)*PSI1(K)/2
            DO L=1,3
               PHI(J)=PHI(J)+SIGMA(J,K,L)*N1(L)*PSI1(K)/2
            END DO
         END DO
      END DO
C
C     Initialize P1, the expectation value of the projection of
C     PSI1 along N1
C
      P1=0.0
C
C     Calculate P1=<PSI1|PHI>
C
      DO J=1,2
         P1=P1+REAL(CONJG(PSI1(J))*PHI(J))
      END DO
C
      RETURN
    END
```

Appendix B

The Spin-Dependent Total Cross Section Difference $\Delta\sigma_{tensor}$

Following Equation 2.31, a general expression for the spin-dependent total cross section difference can be written

$$\Delta\sigma(\theta_1, \theta_2) = 2[(\boldsymbol{\sigma}_1 \cdot \boldsymbol{\sigma}_2)\sigma_s + S_{12}\sigma_t], \tag{B.1}$$

where θ_1 and θ_2 are the angles of the proton target spin and neutron beam spin with respect to the beam direction, $\hat{\boldsymbol{x}}$. As before, σ_s and σ_t are the scalar and tensor parts of the spin-spin cross section, σ_{ss}. The equation can be expressed in terms of θ_1 and θ_2 to give[1]

$$\Delta\sigma = 2[(\sin\theta_1 \sin\theta_2 + \cos\theta_1 \cos\theta_2)\sigma_s - (\sin\theta_1 \sin\theta_2 - 2\cos\theta_1 \cos\theta_2)\sigma_t]. \tag{B.2}$$

Thus, it is possible to measure different linear combinations of σ_s and σ_t by changing the spin directions of the target and beam.

The measurement of two different linear combinations is sufficient to completely determine the two spin-spin cross sections. Although the measurement of both $\Delta\sigma_L$ and $\Delta\sigma_T$ fulfills this requirement, they are not the most desirable for two reasons. First, changing between the longitudinal and transverse geometries requires that the magnet be rotated. This cannot be accomplished while the target is polarized and precludes measuring both $\Delta\sigma_T$ and $\Delta\sigma_L$ in the same experiment. Second, since the

[1] An identical result is obtained using the statistical polarization tensor formalism [Kei93].

goal of these measurements is to determine the strength of the tensor interaction, the most useful measurement is one in which the linear combinations which are diagonal in σ_s and σ_t. Instead, $\Delta\sigma_L$ and $\Delta\sigma_T$ are mixtures of these cross sections. There is, however, a pair of $\Delta\sigma$ geometries which avoids both of these problems. These special cases of $\Delta\sigma$ will be referred to as $\Delta\sigma_{scalar}$ and $\Delta\sigma_{tensor}$. $\Delta\sigma_{tensor}$ is the case in which $\boldsymbol{\sigma}_1 \cdot \boldsymbol{\sigma}_2 = 0$. The result is then given by

$$\Delta\sigma_{tensor} = \pm 3 \sin 2\theta_1 \sigma_t, \tag{B.3}$$

where the upper sign applies in the case $\theta_1 - \theta_2 = +\frac{\pi}{2}$, and the lower sign in the case $\theta_1 - \theta_2 = -\frac{\pi}{2}$. A maximum is obtained for $\theta_1 = \pm\frac{\pi}{4}, \pm\frac{3\pi}{4}$, giving

$$\Delta\sigma_{tensor}^{max} = \pm 3\sigma_t. \tag{B.4}$$

$\Delta\sigma_{scalar}$ is the case in which $S_{12} = 0$. As a result,

$$\Delta\sigma_{scalar} = \frac{\pm 3 \sin 2\theta_1}{\sqrt{1 + 3\cos^2\theta_1}}\sigma_s, \tag{B.5}$$

with the constraint $\tan\theta_1 \tan\theta_2 = 2$. The upper sign refers to the case $-\frac{\pi}{2} \leq \theta_2 \leq +\frac{\pi}{2}$.

Fixing the target spin angle at 45° ($\theta_1 = +\frac{\pi}{4}$) then gives the result

$$\Delta\sigma_{tensor} = 3\sigma_t \quad ; \quad \theta_2 = -45°, \tag{B.6}$$

$$\Delta\sigma_{scalar} = \frac{6}{\sqrt{10}}\sigma_s \quad ; \quad \theta_2 \approx 63°. \tag{B.7}$$

Thus, the experiment can be switched between $\Delta\sigma_{tensor}$ and $\Delta\sigma_{scalar}$ by simply re-setting the spin direction of the neutron beam. The target is left unchanged.

It is often useful to have expressions for these cases in terms of the simpler longitudinal and transverse cross section differences. Through Equations 2.33 and 2.34, the general case $\Delta\sigma$ can be expressed in terms of $\Delta\sigma_L$ and $\Delta\sigma_T$.

$$\Delta\sigma = \Delta\sigma_L \cos\theta_1 \cos\theta_2 + \Delta\sigma_T \sin\theta_1 \sin\theta_2 \tag{B.8}$$

The special cases $\Delta\sigma_{tensor}$ and $\Delta\sigma_{scalar}$ are then given by

$$\Delta\sigma_{tensor} = \frac{\pm \sin 2\theta_1}{2}(\Delta\sigma_L - \Delta\sigma_T), \tag{B.9}$$

$$\Delta\sigma_{scalar} = \frac{\pm\frac{1}{2} \sin 2\theta_1}{\sqrt{1 + 3\cos^2\theta_1}}(\Delta\sigma_L + 2\Delta\sigma_T). \tag{B.10}$$

Using Equations 2.35 and 2.36, $\Delta\sigma_{tensor}$ and $\Delta\sigma_{scalar}$ can be written in terms of phase-shift parameters.

$$\Delta\sigma_{tensor} = \frac{\mp\sin 2\theta_1}{2}\frac{\pi}{k^2}\left[\begin{array}{l} 2-2\cos 2\delta_{3P0}+3\cos\delta_{3P1}-3\cos 2\delta_{3D1} \\ \quad +6\sqrt{2}\sin(\delta_{3S1}+\delta_{3D1})\sin 2\epsilon_1 \\ \quad -\cos 2\delta_{3P2}+5\cos 2\delta_{3D2}-4\cos 2\delta_{3F2} \\ \quad +6\sqrt{6}\sin(\delta_{3P2}+\delta_{3F2})\sin 2\epsilon_2+\cdots \end{array}\right] \quad \text{(B.11)}$$

$$\Delta\sigma_{scalar} = \frac{\pm\frac{1}{2}\sin 2\theta_1}{\sqrt{1+3\cos^2\theta_1}}\frac{\pi}{k^2}\left[\begin{array}{l} -2+3\cos 2\delta_{1S0}-\cos 2\delta_{3P0} \\ \quad +9\cos 2\delta_{1P1}-3\cos 2\delta_{3S1} \\ \quad -3\cos\delta_{3P1}-3\cos 2\delta_{3D1} \\ \quad +15\cos 2\delta_{1D2}-5\cos 2\delta_{3P2} \\ \quad -5\cos 2\delta_{3D2}-5\cos 2\delta_{3F2}+\cdots \end{array}\right] \quad \text{(B.12)}$$

References

[Ada78] J. M. Adams and G. White. *A Versatile Pulse Shape Discriminator for Charged Particle Separation and Its Application to Fast Neutron Time-of-Flight Spectroscopy.* Nuclear Instruments and Methods, **156**(1978) 459–476.

[Arn89] R. A. Arndt. *Phase-Shift Analysis SP89*, 1989. Private Communication.

[Arn92] R. A. Arndt. *Phase-Shift Analysis SM92*, 1992. Private Communication.

[Aur84] R. Aures, W. Heeringa, H. O. Klages, R. Maschuw, F. K. Schmidt, and B. Zeitnitz. *A Brute-Force Polarised Proton Target as an Application of a Versatile Brute-Force Polarisation Facility.* Nuclear Instruments and Methods, **224**(1984) 347–354.

[Bla52a] J. M. Blatt and L. C. Biedenharn. *The Angular Distribution of Scattering and Reaction Cross Sections.* Reviews of Modern Physics, **24**(1952) 258–272.

[Bla52b] J. M. Blatt and L. C. Biedenharn. *Neutron-Proton Scattering with Spin-Orbit Coupling. I. General Expressions.* Physical Review, **86**(1952) 399–404.

[Bow82] J. E. Bowsher. *BABEL*, 1982. Computer Code.

[Bow91] J. D. Bowman. *Computer Code SPINX*, 1991. Private Communication.

[Bra88] R. A. Brandenburg, G. S. Chulick, R. Machleidt, A. Picklesimer, and R. M. Thaler. *Essential Mechanisms in the Triton Binding.* Physical Review C, **37**(1988) 1245–1252.

[Bug80] D. V. Bugg. *How to Improve np Phase-Shifts at 25 and 50 MeV.* Journal of Physics, **G6**(1980) 1329–1333.

[Can83] Canberra Industries, Inc., Meriden, Connecticut. *Pulse Shape Discriminator Model 2160A*, 1983.

[Che87] Z. Chen. *Neutron Attenuation Measurements for Shielding Materials.* Measurements made with the TUNL Neutron Time-of-Flight Group, 1987.

[Chi76] G. E. Childs, L. J. Ericks, and R. L. Powell. *Thermal Conductivity of Solids at Room Temperature and Below.* Monograph 131, NBS, 1976.

[Cle89] T. B. Clegg. *Polarized H^- and D^- Source Development at the Triangle Universities Nuclear Laboratory.* In K. J. Heller, editor, *Particles and Fields Series 37*, volume 187, pages 1227–1236. American Institute of Physics, 1989. Series editor R. G. Lerner.

[DeB67] S. DeBenedetti. *Nuclear Interactions.* John Wiley & Sons, New York, 1967.

[deR89] E. M. M. deRas, J. P. Vaane, and W. van Suetendael. *Investigation of the Nature of a Contamination Caused by Tritium Targets Used for Neutron Production.* In *U.S. Sixth Coordination Meeting for the Program to Meet Nuclear Data Needs for Fusion Energy*, pages 119–122, 1989.

[Don71] T. R. Donoghue, R. C. Haight, G. P. Lawrence, J. E. Simmons, D. C. Dodder, and G. M. Hale. *Polarization Transfer in the Reaction $^3H(\vec{p},\vec{n})\ ^3He$ at 0° for E_p in the Range 3 to 16 MeV.* Physical Review Letters, **27**(1971) 947–949.

[Eri84] T. E. O. Ericson. *Nuclear Low Energy Tests of OPEP.* Comments on Nuclear and Particle Physics, **13**(1984) 157–170.

[Gou81] C. R. Gould, L. L. Holzsweig, S. E. King, Y. C. Lau, R. V. Poore, N. R. Roberson, and S. A. Wender. *The XSYS Data Acquisition System at Triangle Universities Nuclear Laboratory.* IEEE Transactions in Nuclear Science, **NS-28**(1981) 3708–3714.

[Gou84] C. R. Gould, D. G. Haase, K. E. Nash, and N. R. Roberson. *The Cryogenic Polarized Target Facility.* In *Annual Report XXIII*, pages 121–123, Durham, North Carolina, 1984. Triangle Universities Nuclear Laboratory.

[Gre86] D. S. Greywall. *^{3}He Specific Heat and Thermometry at Millikelvin Temperatures.* Physical Review B, **33**(1986) 7520–7538.

[Hai72] R. C. Haight, J. E. Simmons, and T. R. Donoghue. *Polarization and Polarization Transfer in the Reaction T(p,n) ^{3}He.* Physical Review C, **5**(1972) 1826–1834.

[Hee85] W. Heeringa, R. Aures, R. Maschuw, and F. K. Schmidt. *Brute-Force Polarization of Protons in TiH_2.* Cryogenics, **25**(1985) 369–374.

[Jac75] J. D. Jackson. *Classical Electrodynamics*, pages 177–180. John Wiley & Sons, New York, second edition, 1975.

[Kei90] C. D. Keith. *Applications of ^{3}He Melting Curve Thermometry in a Nuclear Polarization Experiment.* Master's thesis, North Carolina State University, 1990.

[Kei92] C. D. Keith, C. R. Gould, D. G. Haase, N. R. Roberson, W. Tornow, and W. S. Wilburn. *^{3}He Melting Curve Thermometry in a Nuclear Polarization Experiment.* Hyperfine Interactions, **75**(1992) 525–532.

[Kei93] C. D. Keith, 1993. Private Communication.

[Kel39] J. M. B. Kellogg, I. I. Rabi, N. F. Ramsey, and J. R. Zacharias. *Magnetic Moments of the Proton and the Deuteron.* Physical Review, **56**(1939) 728–743.

[Kos90] J. E. Koster. *A Test of Time Reversal Invariance with Polarized Neutrons and Aligned ^{165}Holmium.* Ph.D. thesis, North Carolina State University, 1990.

[Lac80] M. Lacombe, B. Loiseau, J. M. Richard, V. Vinh Mau, J. Côté, P. Pirès, and R. de Tourreil. *Parametrization of the Paris N-N Potential.* Physical Review C, **21**(1980) 861–873.

[Lew87] H. W. Lewis, 1987. Private Communication.

[Li92] J. Li, A. Pflaum, F. Pobell, P. Sekowski, U. Stuhr, and H. Wipf. *Thermal Conductivity and Heat Capacity of Titanium Hydrides.* Journal of Low Temperature Physics, **88**(1992) 309–315.

[Lin] Link Analytical Limited, Bucks, England. *Pulse Shape Discriminator and Gated Integrator Model 5020.*

[Lis75] P. W. Lisowski, R. L. Walter, C. E. Busch, and T. B. Clegg. *Polarization Transfer in the $^2H(\vec{d},\vec{n})\,^3He$ Reaction at 0°.* Nuclear Physics, **A242**(1975) 298–308.

[Lon51] H. London. In *Proceedings of the International Conference on Low Temperature Physics*, page 157, 1951.

[Lon62] H. London, G. R. Clarke, and E. Mendoza. *Osmotic Pressure of ^3He in Liquid ^4He with Proposals for a Refrigerator to Work below 1 K.* Physical Review, **128**(1962) 1992–2005.

[Lou74] O. V. Lounasmaa. *Experimental Principles and Methods Below 1 K*, chapter 3, pages 17–58. Academic Press, London, 1974.

[Mac86] R. Machleidt. *The Meson Theory of Nuclear Forces and Nuclear Matter.* In M. B. Johnson and A. Picklesimer, editors, *Relativistic Dynamics and Quark-Nuclear Physics*, pages 71–173. John Wiley & Sons, New York, 1986.

[Mac87] R. Machleidt, K. Holinde, and C. Elster. *The Bonn Meson-Exchange Model for the Nucleon-Nucleon Interaction.* Physics Reports, **149**(1987) 1–89.

[Mac89] R. Machleidt. *The Meson Theory of Nuclear Forces and Nuclear Structure.* Advances in Nuclear Physics, **19**(1989) 189–376.

[Mar83] H. Marshak. *Nuclear Orientation Thermometry.* Journal of Research of the National Bureau of Standards, **88**(1983) 175–217.

[Mos65] S. J. Moss and W. Haeberli. *The Polarization of Protons Scattered by Carbon.* Nuclear Physics, **72**(1965) 417–435.

[Nag78] M. M. Nagels, T. A. Rijken, and J. J. de Swart. *Low-Energy Nucleon-Nucleon Potential from Regge-Pole Theory.* Physical Review D, **17**(1978) 768–776.

[Nat84] National Electrostatics Corporation, Middleton, Wisconsin. *Instruction Manual for Operation and Service of Beam Profile Monitor Model BPM-80*, 1984.

[Nat90] National Nuclear Data Center, Brookhaven National Laboratory, Upton, New York. *ENDF/B-VI Data File for Oxygen*, January 1990. Evaluation by G. Hale, Z. Chen, and P. Young.

[Nat91] National Nuclear Data Center, Brookhaven National Laboratory, Upton, New York. *ENDF/B-VI Data File for Carbon*, July 1991. Evaluation by C. Y. Fu, E. J. Axton, and F. G. Perey, Revision 1.

[Ock91a] M. Ockenfels, T. Köble, M. Schwindt, J. Weltz, and W. von Witsch. *Measurement of the Neutron-Proton Polarization Transfer Coefficient $K_y^{y'}$ at 17.4 MeV.* Nuclear Physics, **A534**(1991) 248–254.

[Ock91b] M. Ockenfels, F. Meyer, T. Köble, W. von Witsch, J. Weltz, K. Wingender, and G. Wollmann. *Measurement of the Spin Transfer Parameter $K_y^{y'}$ in np Scattering at 25.8 MeV.* Nuclear Physics, **A526**(1991) 109–130.

[Pic92] A. Picklesimer, R. A. Rice, and R. Brandenburg. *Δ Degrees of Freedom in Trinuclei. V. Exotic Contributions.* Physical Review C, **46**(1992) 1178–1182.

[Rei68] R. V. Reid. *Local Phenomenological Nucleon-Nucleon Potentials.* Annals of Physics, **50**(1968) 411–448.

[Rob81] N. R. Roberson and S. E. Edwards. *Interface for the TUNL VAX Data Acquisition Facility.* IEEE Transactions in Nuclear Science, **NS-28**(1981) 3834–3837.

[Sam92] F. Sammarruca, D. P. Xu, and R. Machleidt. *Relativistic Corrections to the Triton Binding Energy.* Physical Review C, **46**(1992) 1636–1641.

[Sat71] G. R. Satchler et al. *The Madison Convention.* In H. H. Barschall and W. Haeberli, editors, *Proceedings of the 3rd International Symposium on Polarization Phenomena in Nuclear Reactions, 1970*, pages xxv–xxix, Madison, 1971. The University of Wisconsin Press.

[Sch68] L. I. Schiff. *Quantum Mechanics.* McGraw-Hill Book Company, New York, third edition, 1968.

[Sch88] M. Schöberl, H. Kuiper, R. Schmelzer, G. Mertens, and W. Tornow. *Measurement of the Neutron-Proton Spin Correlation Coefficient $A_{yy}(\theta)$ at 90° c.m. by Elastic Scattering of 13.7 MeV Polarized Neutrons from a Polarized Proton Target.* Nuclear Physics, **A489**(1988) 284–302.

[Sim73] J. E. Simmons, W. B. Broste, T. R. Donoghue, R. C. Haight, and J. C. Martin. *Sources of Polarized Neutrons from 2 to 33 MeV Using Polarization Transfer Reactions at 0°.* Nuclear Instruments and Methods, **106**(1973) 477–480.

[SP86] N. J. Stone and H. Postma, editors. *Low-Temperature Nuclear Orientation.* North-Holland Physics Publishing, Amsterdam, 1986.

[Sta72] T. Stammbach and R. L. Walter. *R-Matrix Formulation and Phase Shifts for n-^{4}He and p-^{4}He Scattering for Energies up to 20 MeV.* Nuclear Physics, **A180**(1972) 225–240.

[Swa60] C. D. Swartz and G. E. Owen. *Recoil Detection in Scintillators.* In J. B. Marion and J. L. Fowler, editors, *Fast Neutron Physics Part I*, chapter II.B, pages 211–246. Interscience Publishers, Inc., New York, 1960.

[Ter68] G. E. Terrell, M. F. Jahns, M. R. Kostoff, and E. M. Bernstein. *Polarization in ^{12}C(p,p) ^{12}C.* Physical Review, **173**(1968) 931–936.

[Tor74] W. Tornow. *Fast Neutron Double Scattering on ^{4}He.* Zeitschrift für Physik, **266**(1974) 357–365.

[Tor75] W. Tornow, H. Spiegelhauer, and G. Mack. *Simulation of a Double-Scattering Polarization Experiment with Fast Neutrons by Means of Monte Carlo Calculations.* Nuclear Instruments and Methods, **125**(1975) 373–389.

[Tor88] W. Tornow. *Sensitivity of the Mixing Parameter ϵ_1 to the Spin-Dependent Neutron-Proton Total Cross Sections.* Bulletin of the American Physical Society, **33**(1988) 1582.

[Tor91] W. Tornow. *Recent Developments in Low-Energy Nucleon-Nucleon Interaction Studies.* In S. W. Wissink, C. D. Goodman, and G. E. Walker, editors, *Spin and Isospin in Nuclear Interactions*, pages 461–487, New York, 1991. Plenum Press. Proceedings of an international conference held March 11–15, 1991 in Telluride, Colorado.

[Tor92] W. Tornow, 1992. Private Communication.

[VdG60] R. J. Van de Graaff. *Tandem Electrostatic Accelerators.* Nuclear Instruments and Methods, **8**(1960) 195–202.

[Yuk35] H. Yukawa. *Interaction of Elementary Particles.* Proceedings of the Physico-Mathematical Society of Japan, **17**(1935) 48–57.

Biography

Wesley Scott Wilburn

Personal

Born in Pensacola, Florida, March 9, 1964
Married Dianne Williams, August 11, 1989

Education

B.S. Physics, North Carolina State University, Raleigh, North Carolina, 1987
B.S. Electrical Engineering, North Carolina State University, Raleigh, North Carolina, 1987
A.M. Physics, Duke University, Durham, North Carolina, 1990

Academic Positions

President, NCSU Society of Physics Students, 1986–1987
Townes-Perkins Fellow, Duke University, 1987–1990
Teaching Assistant, Duke University, 1987–1989
Research Assistant, Duke University, 1989–1993

Memberships

American Physical Society
Sigma Pi Sigma

Publications

W. Tornow, O. K. Baker, C. R. Gould, D. G. Haase, N. R. Roberson, and W. S. Wilburn. *Experimental Determination of the NN Tensor Force.* In J. Sowinski and S. E. Vigdor, editors, *Physics with Polarized Beams on Polarized Targets.* World Scientific, Singapore, 1990.

J. E. Koster, E. D. Davis, C. R. Gould, D. G. Haase, N. R. Roberson, L. W. Seagondollar, S. Wilburn, and X. Zhu. *Direct Reaction Test of T Violation in 2 MeV Neutron Scattering from Aligned ^{165}Ho.* Physics Letters B, **267**(1991) 23–26.

C. D. Keith, C. R. Gould, D. G. Haase, N. R. Roberson, W. Tornow, and W. S. Wilburn. *^{3}He Melting Curve Thermometry in a Nuclear Polarization Experiment.* Hyperfine Interactions, **75**(1992) 525–532.

Contributed Abstracts

W. S. Wilburn, N. R. Roberson, K. A. Sweeton, E. W. Hoen, and T. B. Clegg. *Computer Control System for a Polarized Ion Source.* Bulletin of the American Physical Society, **33**(1988) 2201.

W. S. Wilburn, N. R. Roberson, W. Tornow, C. R. Gould, and D. G. Haase. *Experimental Determination of the Zero-Crossing of the Spin-Dependent Neutron-Proton Total Cross-Section Differences $\Delta\sigma_T$ and $\Delta\sigma_L$ and its Bearing on the NN Tensor Force.* In *Proceedings of the 7th International Conference on Polarization Phenomena in Nuclear Physics,* Paris, 1990, page 27A.

W. S. Wilburn, P. R. Huffman, J. E. Koster, N. R. Roberson, W. Tornow, C. R. Gould, D. G. Haase, and C. D. Keith. *Measurement of $\Delta\sigma_T$ in Polarized Neutron/Polarized Proton Scattering.* Bulletin of the American Physical Society, **37**(1992) 902.

W. S. Wilburn, P. R. Huffman, J. E. Koster, N. R. Roberson, W. Tornow, C. R. Gould, D. G. Haase, and C. D. Keith. *The NN Tensor Force from $\vec{n}$-$\vec{p}$ Scattering.* In I. R. Afnan and R. T. Cahill, editors, *Proceedings of the XIII International Conference on Few-Body Problems in Physics,* Adelaide, 1992, page 124.

Co-Authored Abstracts

T. Clegg, K. Felder, W. Hooke, J. Hunn, H. Lewis, A. Lovette, H. Middleton, H. Pfützner, R. Roberson, H. Robinson, K. Sweeton, and S. Wilburn. *Design of an Atomic Beam Polarized Ion Source with an ECR Ionizer.* Bulletin of the American Physical Society, **33**(1988) 905.

K. Felder, H. G. Robinson, H. W. Lewis, W. S. Wilburn, and T. B. Clegg. *Development of New RF Cavities for Use in a Polarized Ion Source.* Bulletin of the American Physical Society, **33**(1990) 2200.

J. E. Koster, C. R. Gould, D. G. Haase, W. Seagondollar, N. R. Roberson, W. S. Wilburn, and X. Zhu. *Holmium Deformation Effect Measured with a Rotating Aligned Target.* Bulletin of the American Physical Society, **35**(1990) 926.

C. D. Keith, D. G. Haase, C. R. Gould, W. S. Wilburn, N. R. Roberson, and W. Tornow. *Application of ^{3}He Melting Curve Thermometry in a Nuclear Orientation Cryostat.* Bulletin of the American Physical Society, **35**(1990) 2361.

T. B. Clegg, D. J. Abbott, T. C. Black, E. R. Crosson, R. K. Das, K. A. Fletcher, C. R. Howell, H. J. Karwowski, J. E. Koster, S. Lemieux, E. J. Ludwig, M. Al-Ohali, N. R. Roberson, K. A. Sweeton, W. Tornow, W. S. Wilburn, and J. Z. Williams. *Report on Operation of a New Intense Polarized Ion Source and ECR Ionizer.* In *Proceedings of the 7th International Conference on Polarization Phenomena in Nuclear Physics,* Paris, 1990, page 3E.

W. Tornow, N. R. Roberson, W. S. Wilburn, C. R. Gould, and D. G. Haase. *Experimental Determination of the Nucleon-Nucleon Tensor Force via $\Delta\sigma_T$ and $\Delta\sigma_L$ Measurements.* In *Proceedings of the 7th International Conference on Polarization Phenomena in Nuclear Physics,* Paris, 1990, page 29A.

C. D. Keith, C. R. Gould, D. G. Haase, P. R. Huffman, N. R. Roberson, W. Tornow, and W. S. Wilburn. *Level Structure of ^{4}He and the Spin Dependence of the n-^{3}He Total Cross Section.* Bulletin of the American Physical Society, **37**(1992) 1257.